

A HIGH-ORDER LOW-ORDER ALGORITHM WITH
EXPONENTIALLY-CONVERGENT MONTE CARLO FOR THERMAL
RADIATIVE TRANSFER PROBLEMS

A Dissertation

by

SIMON RAY BOLDING

Submitted to the Office of Graduate and Professional Studies of
Texas A&M University
in partial fulfillment of the requirements for the degree of

DOCTOR OF PHILOSOPHY

Chair of Committee,	Jim Morel
Committee Members,	Ryan McClarren
	Jean Ragusa
	Jean-Luc Guermond
Head of Department,	Yassin Hassan

December 2016

Major Subject: Nuclear Engineering

Copyright 2016 Simon Ray Bolding

ABSTRACT

We have implemented a new high-order low-order (HOLO) algorithm for solving thermal radiative transfer problems. The low-order (LO) system is based on spatial and angular moments of the transport equation and a linear-discontinuous finite-element spatial representation, producing equations similar to the standard S_2 equations. The LO solver is fully implicit in time and efficiently resolves the non-linear temperature dependence at each time step. The HO solver utilizes exponentially-convergent Monte Carlo (ECMC) to give a globally accurate solution for the angular intensity to a fixed-source, pure absorber transport problem. This global solution is used to compute consistency terms, which require the HO and LO solutions to converge towards the same solution. The use of ECMC allows for the efficient reduction of statistical noise in the MC solution, reducing inaccuracies introduced through the LO consistency terms. We compare results with an implicit Monte Carlo (IMC) code for one-dimensional, gray test problems and demonstrate the efficiency of ECMC over standard Monte Carlo in this HOLO algorithm.

DEDICATION

This is an optional page. Lorem ipsum dolor sit amet, consectetur adipiscing elit. Integer lectus quam, condimentum quis bibendum eu, sollicitudin eget lacus. Praesent non sodales odio. Class aptent taciti sociosqu ad litora torquent per conubia nostra, per inceptos himenaeos. Nulla ac luctus sapien. Morbi cursus sapien eget lorem fermentum hendrerit. Nam ac erat dui, in cursus velit. Vivamus hendrerit porttitor nisi, ut porttitor lorem volutpat eget. In ligula ligula, euismod ut condimentum sit amet, pulvinar sit amet diam. Pellentesque interdum, ipsum ullamcorper consequat dignissim, sem arcu egestas mauris, vitae interdum sem tortor ut ante. Nunc blandit laoreet nisi, non rutrum lorem hendrerit quis. Cras nunc diam, convallis et feugiat at, auctor id libero. Nunc facilisis massa eu eros imperdiet vestibulum. Vestibulum ante ipsum primis in faucibus orci luctus et ultrices posuere cubilia Curae; Donec non velit vitae tortor blandit semper.

Etiam vitae dolor nulla. Ut eros odio, rhoncus eget placerat vitae, elementum ac ante. Proin vitae odio eu nisl pharetra mattis. Pellentesque habitant morbi tristique senectus et netus et malesuada fames ac turpis egestas. Phasellus fermentum lacus consectetur neque consequat ullamcorper. Cras blandit urna non dui consequat molestie. Curabitur viverra nibh at nisi semper faucibus. Nam egestas mauris a enim dignissim nec consectetur tortor rutrum. Mauris at nisi in est luctus congue ut mattis est. Ut pretium, mi quis elementum cursus, ante eros suscipit ligula, ut porttitor elit leo sed turpis. Nam sed dui ligula.

ACKNOWLEDGEMENTS

Lorem ipsum dolor sit amet, consectetur adipiscing elit. Integer lectus quam, condimentum quis bibendum eu, sollicitudin eget lacus. Praesent non sodales odio. Class aptent taciti sociosqu ad litora torquent per conubia nostra, per inceptos himenaeos. Nulla ac luctus sapien. Morbi cursus sapien eget lorem fermentum hendrerit. Nam ac erat dui, in cursus velit. Vivamus hendrerit porttitor nisi, ut porttitor lorem volutpat eget. In ligula ligula, euismod ut condimentum sit amet, pulvinar sit amet diam. Pellentesque interdum, ipsum ullamcorper consequat dignissim, sem arcu egestas mauris, vitae interdum sem tortor ut ante. Nunc blandit laoreet nisi, non rutrum lorem hendrerit quis. Cras nunc diam, convallis et feugiat at, auctor id libero. Nunc facilisis massa eu eros imperdiet vestibulum. Vestibulum ante ipsum primis in faucibus orci luctus et ultrices posuere cubilia Curae; Donec non velit vitae tortor blandit semper.

Etiam vitae dolor nulla. Ut eros odio, rhoncus eget placerat vitae, elementum ac ante. Proin vitae odio eu nisl pharetra mattis. Pellentesque habitant morbi tristique senectus et netus et malesuada fames ac turpis egestas. Phasellus fermentum lacus consectetur neque consequat ullamcorper. Cras blandit urna non dui consequat molestie. Curabitur viverra nibh at nisi semper faucibus. Nam egestas mauris a enim dignissim nec consectetur tortor rutrum. Mauris at nisi in est luctus congue ut mattis est. Ut pretium, mi quis elementum cursus, ante eros suscipit ligula, ut porttitor elit leo sed turpis. Nam sed dui ligula.

TABLE OF CONTENTS

	Page
ABSTRACT	ii
DEDICATION	iii
ACKNOWLEDGEMENTS	iv
TABLE OF CONTENTS	v
LIST OF FIGURES	viii
LIST OF TABLES	ix
1. INTRODUCTION	1
1.1 Thermal Radiative Transfer Background	1
1.1.1 Derivation of 1D Grey Model	2
1.2 Previous Work	2
1.2.1 The Implicit Monte Carlo Method	3
1.2.2 Previous work on moment-based acceleration methods	6
1.3 Overview of the HOLO Algorithm	7
1.3.1 Similarities to Residual Monte Carlo	9
1.4 Dissertation Layout	10
2. OVERVIEW OF THE HOLO ALGORITHM	11
3. THE MOMENT-BASED LOW-ORDER EQUATIONS	15
3.1 Forming the Space-Angle Moment Equations	15
3.1.1 LO Spatial mesh and Finite-Element Spatial Moments	15
3.1.2 Definition of Angular Moments	17
3.1.3 Space-Angle Moments of the Radiation Transport Equation	18
3.1.4 The Angular Consistency Terms	19
3.1.5 The Exact Radiation Moment Equations	20
3.1.6 Material Energy Equations	21
3.2 Closing the LO System with Information from the HO Solution	22
3.2.1 Angular Closure	23
3.2.2 Spatial Closure	23

3.2.3	Newton's Method for LO Equations	25
4.	THE HIGH-ORDER EXPONENTIALLY-CONVERGENT MONTE CARLO SOLVER	26
4.1	The ECMC High Order Solver	26
4.2	MC solution with LDD trial space	30
4.3	Implementation of ECMC finite-element space, tallies, and residual sampling	33
4.4	Adaptive Mesh Refinement	35
4.4.1	Continuous Weight Deposition Tallies	35
4.4.2	Modified Systematic Sampling Algorithm	36
5.	THE MOMENT-BASED LOW-ORDER EQUATIONS	38
5.1	Forming the Space-Angle Moment Equations	38
5.1.1	LO Spatial mesh and Finite-Element Spatial Moments	38
5.1.2	Definition of Angular Moments	40
5.1.3	Space-Angle Moments of the Radiation Transport Equation	41
5.1.4	The Angular Consistency Terms	42
5.1.5	The Exact Radiation Moment Equations	43
5.1.6	Material Energy Equations	44
5.2	Closing the LO System with Information from the HO Solution	45
5.2.1	Angular Closure	46
5.2.2	Spatial Closure	46
5.2.3	Newton's Method for LO Equations	48
6.	ACCELERATED ITERATIVE SOLUTION TO THE LO EQUATIONS	49
6.1	Source Iteration Solution to the Linearized LO Equations	50
6.2	Linear Diffusion Synthetic Acceleration	51
6.2.1	The WLA-DSA Accelerated Source Iteration Algorithm	54
6.3	GMRES Solution to the LO Equations	55
6.4	Computational Results	56
6.4.1	Results for LD Spatial Discretization	57
7.	THE HIGH-ORDER EXPONENTIALLY-CONVERGENT MONTE CARLO SOLVER	59
7.1	The ECMC High Order Solver	59
7.2	MC solution with LDD trial space	63
7.3	Implementation of ECMC finite-element space, tallies, and residual sampling	66
7.4	Adaptive Mesh Refinement	68

7.4.1	Continuous Weight Deposition Tallies	68
7.4.2	Modified Systematic Sampling Algorithm	69
7.5	COMPUTATIONAL RESULTS	70
7.5.1	Marshak Wave	71
7.5.2	Two Material Problem	73
7.5.3	Performance comparison of IMC and HOLO-ECMC	75
7.5.4	Comparison of different HO Solvers	77
7.5.5	Pre-heated Marshak wave problem and adaptive mesh refinement	79
7.6	Accuracy in the Equilibrium Diffusion Limit	80
7.7	CONCLUSIONS	81
8.	ACCELERATED ITERATIVE SOLUTION TO THE LO EQUATIONS .	87
8.1	Source Iteration Solution to the Linearized LO Equations	88
8.2	Linear Diffusion Synthetic Acceleration	89
8.2.1	The WLA-DSA Accelerated Source Iteration Algorithm	92
8.3	GMRES Solution to the LO Equations	93
8.4	Computational Results	94
8.4.1	Results for LD Spatial Discretization	95
8.5	Analytic Neutronics answer for Source fixup	95
8.6	Estimating the Spatial Closure from the HO Solution	98
8.6.1	Motivation	98
8.6.2	Choice of Spatial Closure	99
8.6.3	The Doubly-Discontinuous Trial Space	101
8.7	Face Tallies and correction near $\mu = 0$	103
8.8	Preservation of the Discrete Maximum Principle	104
	REFERENCES	110

LIST OF FIGURES

FIGURE		Page
3.1	Illustration of linear finite element basis functions $b_{L,i}(x)$ and $b_{R,i}(x)$ for spatial element i	16
5.1	Illustration of linear finite element basis functions $b_{L,i}(x)$ and $b_{R,i}(x)$ for spatial element i	39
7.1	Comparison of radiation temperatures for Marshak wave problem at $t = 5$ sh.	84
7.2	Comparison of radiation temperatures for two material problem.	85
7.3	Comparison of radiation temperatures for the pre-heated Marshak wave problem for 100 x cells at $t = 0.5$ sh.	86
7.4	Comparison of T_r for step and LDFE discretizations of the LO equations in the equilibrium diffusion limit.	86
8.1	Linear doubly-discontinuous representation for mean intensity in LO equations	102
8.2	T_r and T for MP violation problem with IMC and $\Delta t = 0.001$ sh. . .	107
8.3	T_m for MP violation problem with IMC for various time step sizes. . .	108
8.4	T_m for MP violation problem with HOLO method for various time step sizes.	108

LIST OF TABLES

TABLE		Page
6.1	Scattering source iterations for the two material problem. Simulation end time is 1 sh.	58
6.2	Scattering source iterations for the equilibrium diffusion limit problem. Simulation end time is 3 sh.	58
7.1	Comparison of sample statistics for the Marshak Wave problem. Simulation end time is $t = 5$ sh.	73
7.2	Material properties for two material problem	74
7.3	Comparison of sample statistics for the two material problem for 200 x cells. Simulation end time is $t = 2$ sh.	75
7.4	Comparison of average CPU times per history and LO iteration counts for the Marshak Wave problem.	77
7.5	Average CPU times per history and LO iteration counts required for the two material problem.	77
7.6	Comparison of sample statistics for the Marshak Wave problem. Number of ECMC batches is indicated in parenthesis. .	78
7.7	Comparison of sample standard deviations for the two material problem. Number of ECMC batches is indicated in parenthesis.	78
7.8	Comparison of sample statistics for the pre-heated marshak wave problem for 100 x cells. Number of ECMC batches is indicated in parenthesis.	80
8.1	Scattering source iterations for the two material problem. Simulation end time is 1 sh.	96
8.2	Scattering source iterations for the equilibrium diffusion limit problem. Simulation end time is 3 sh.	96

8.3	Problem specifications for maximum principle violation. Absorption cross section has form $\sigma_a = \sigma_{a,0}/T^3$	107
8.4	Comparison of LO Newton iterations for HOLO solution to MP problem and different time step sizes. For $\Delta t = 0.1$ sh, no damping was used; for all other cases a damping factor of 0.5 was used.	109

1. INTRODUCTION

1.1 Thermal Radiative Transfer Background

Thermal radiative transfer (TRT) physics describe the time-dependent energy distributions of a photon radiation field and a high-temperature material. The material and radiation exchange energy through absorption and emission of photons by the material. Accurate modeling of TRT physics becomes relevant in the high-energy, high-density physics regime. Radiative transfer is the dominant form of heat transfer in very high-temperature systems, where the material temperature T is $O(10^6)$ K or higher. Typical computational applications of TRT include simulation of inertial confinement fusion and astrophysics phenomena.

The transport of photons through a material is characterized by particle position, direction, and frequency. The material energy distribution is described by the material internal energy as a function of position. The high-dimensional space results in a nonlinear transport problem that is difficult to solve. The internal energy e is related to the material temperature through an equation of state. In this work a perfect gas equation of state is used [?], which produces the relation $\rho c_v T = e$, where ρ is the material mass density and c_v is the specific heat. Thus, we will now describe the equations in terms of temperature.

The equations are strongly coupled through the gray Planckian emission source $\sigma_a a c T^4$, which is a nonlinear function of temperature, and the radiation absorption term $\sigma_a \phi$. In general, the material properties are a function of T . The temperature-dependent material properties and absorption and reemission physics lead to systems that require accurate modeling of photon transport through a mix of streaming and optically-thick, diffusive regions. Although in most physical applications material

motion is present, it is not the focus of this research and will not be considered. The purpose of the proposed research is to demonstrate the ability of a new algorithm to provide highly-accurate and efficient solutions to Eq. (1.1) and Eq. (1.2).

1.1.1 Derivation of 1D Grey Model

The transport of photons through a material is governed by the Boltzmann linear transport equation [4, 2]. We will make an assumption of isotropic scattering to simplify the equations. The radiative

This research will focus on a simplified 1D slab-geometry and frequency-integrated (grey) TRT model. The governing equations for this simplified model are the radiation and material energy balance equations

$$\frac{1}{c} \frac{\partial I(x, \mu, t)}{\partial t} + \mu \frac{\partial I(x, \mu, t)}{\partial x} + \sigma_t I(x, \mu, t) = \frac{\sigma_s}{2} \phi(x, t) + \frac{1}{2} \sigma_a a c T^4(x, t) \quad (1.1)$$

$$\rho c_v \frac{\partial T(x, t)}{\partial t} = \sigma_a \phi(x, t) - \sigma_a a c T^4(x, t). \quad (1.2)$$

In the above equations the fundamental unknowns are the material temperature $T(x, t)$ and the angular intensity $I(x, \mu, t)$ of radiation, where x is the position, t is the time, μ is the x -direction cosine of the photon direction of travel, and a , c , ρ , and c_v are the radiation constant, speed of light, material mass density, and material specific heat; σ_a , σ_s , and σ_t are the absorption, scattering, and total cross sections (cm^{-1}), respectively. The scalar radiation intensity $\phi(x, t) = \int_{-1}^1 I(x, \mu, t) d\mu$ is related to the radiation energy density E (with typical units $\text{Jks cm}^{-3} \text{ sh}^{-1}$) by the relation $E = \phi/c$.

1.2 Previous Work

This sections describes related work on Monte Carlo solution to the TRT equations. The Monte Carlo (MC) method samples the underlying physics distributions

to estimate the average behavior of a field of photon. This can provide a highly-accurate results, in particular for treatment of the angular and temporal variable in the transport equation. The temperature equation is almost always solved deterministically in such particle transport methods. Monte carlo solution to the transport equation can introduce large statistical noise into the material temperature distribution, which is undesirable when coupling to other physics. To improve the efficiency of MC solutions, hybrid MC methods utilize a deterministic solution to accelerate the MC solution.

1.2.1 The Implicit Monte Carlo Method

Monte Carlo (MC) solution to the TRT equations is typically achieved by the implicit Monte Carlo (IMC) method [1]. This method partially linearizes Eq. (1.1) & Eq. (1.2) over a discrete time step, with material properties evaluated at the previous temperature. Linearization of the system produces a transport equation that contains an approximate emission source and an effective scattering cross section representing absorption and reemission of photons over a time step. This transport equation is advanced over a time step via MC. The MC simulation tallies energy absorption over a discretized spatial mesh. The energy absorption in each mesh cell is used to directly estimate a new end of time step temperature in that cell. In optically thick regions, or for large time steps, the effective scattering dominates interactions. In these diffusive regions IMC becomes computationally expensive. Acceleration methods typically attempt to improve efficiency by allowing particles to take discrete steps through optically thick regions based on a discretized diffusion approximation [?, ?]. In IMC the approximate linearization of the emission source is not iterated on within a time step due to the large computational cost of the MC transport each time step; this imposes a limit on the time step size to produce physically accurate results [?].

The Monte Carlo (MC) method [4] is a standard computational method in the field of radiation transport. The implicit Monte Carlo (IMC) method [1] is the most common approach for applying the MC method to TRT problems. The IMC method partially linearizes Eq. (1.1) and Eq. (1.2) over a discrete time step and lags material properties to produce a linear transport equation, which can be solved with MC simulation. The linear transport equation contains an approximate emission source and effective scattering cross section that represent absorption and reemission of photons over a time step. The transport equation is solved with MC simulation to advance the distribution of radiation to the end of the time step and determine the energy absorbed by the material over the time step. The energy absorption by the material is tallied over a discrete spatial mesh, computed with cell-averaged quantities. The energy absorption in each mesh cell is used to directly estimate a new end of time step material temperature based on the linearized material energy balance equation. Integration of the time-variable is treated continuously over the time step via MC sampling, but the linearized Planckian source in the transport equation is based on a time-discrete approximation.

The IMC method has some limitations. In optically thick regions, or for large time steps, the effective scattering dominates interactions. In these diffusive regions IMC becomes computationally expensive. Acceleration methods typically attempt to improve efficiency by allowing particles to take discrete steps through optically-thick regions based on a spatially-discretized diffusion approximation [?, ?]. Another issue occurs due to the approximate linearization of the system which can not be iteratively improved due to the high computational cost of the MC transport. For some problems, the linearization can yield non-physical results that violate the discrete maximum principle if the time step size is too large or the cell size is too small [?]. The violation of the maximum principle results in the material temperature being

artificially higher than the boundary conditions and sources should physically allow. The violation is caused by the temperature in the emission source not being fully implicit in time due to the necessary linearization. The work in [?] uses less-expensive MC iterations to produce an implicit system which prevents this from happening, but has very slow iterative convergence in diffusive problems. In IMC, temperature-dependent material properties, in particular cross sections, are evaluated at the previous-time step temperature. These lagged cross sections can produce inaccurate solutions but do not cause stability issues.

In IMC the material and radiation energy fields are discretized spatially to solve for cell-averaged values. Inaccurate spatial representation of the emission source over a cell can result in energy propagating through the domain artificially fast, yielding non-physical results referred to as “teleportation error” [?]. The IMC method uses a fixup known as source tilting to mitigate this problem. Source tilting reconstructs a more accurate linear-discontinuous representation of the emission source within a cell based on the cell-averaged material temperatures in adjacent cells. Recent work in IMC has incorporated a linear-discontinuous finite-element representation directly into the discretization of the material temperature equation [?].

For TRT simulations, inaccurate spatial representation of the emission source over a cell can result in energy propagating through the domain artificially fast, yielding non-physical results referred to as “teleportation error” [?]. The IMC method uses a fixup known as source tilting to mitigate this problem. Source tilting reconstructs a more accurate linear-discontinuous representation of the emission source within a cell based on the cell-averaged material temperatures in adjacent cells. This linear reconstruction is also necessary to preserve the asymptotic equilibrium diffusion limit (EDL), at least for a more general time step size and class of problems than for a piece-wise constant representation [?]. Preserving the equilibrium diffusion limit

is an important aspect of a numerical method for TRT problems. In this limit, cells are optically thick and diffusive, and the material and radiation energy fields approach equilibrium. Spatial discretizations which do not preserve the EDL can produce inaccurate solutions, even though the mesh size should accurately capture the behavior of the solution [?].

1.2.2 Previous work on moment-based acceleration methods

An alternative application of MC to the TRT equations is moment-based hybrid MC methods. Recent work has focused on so-called high-order low-order (HOLO) methods [?, ?, ?, ?]. These methods involve fixed-point iterations between high-order (HO) MC solution of a transport equation and a deterministic LO system. The low-order (LO) operator is based on angular moments of the transport equation, formulated over a fixed spatial mesh. Physics operators that are time consuming for MC to resolve, e.g., absorption-reemission physics, are moved to the LO system. The reduced angular dimensionality of the system and Newton methods allow for nonlinearities in the LO equations to be fully resolved efficiently [?, ?]. The high-order (HO) transport problem is defined by Eq. (1.1), with sources estimated from the previous LO solution. The high-order (HO) transport equation is solved via MC to produce a high-fidelity solution for the angular intensity. The MC estimate of the angular intensity is used to estimate consistency terms, present in the LO equations, that require the LO system to preserve the angular accuracy of the MC solution. These consistency terms are present in all spatial-regions of the problem, requiring statistical variance to be reduced sufficiently throughout the entire domain of the problem.

Another area of related research is the application of residual Monte Carlo. The goal of these methods is to solve an auxiliary transport equation for the error in some

estimate of the intensity. The error is then added to the estimate of the solution, which can produce an overall solution for the intensity that has less statistical noise than solution of the original transport equation would produce. In [?], the MC simulation solves for the change in intensity from the previous time step. This has the potential to limit statistical noise significantly in regions where the solution is near equilibrium. The work in [?] used residual MC as a HO solver for 1D grey problems. The residual MC demonstrated impressive reduction in statistical variance. However, a piecewise constant representation was used for the space-angle representation of the intensity, which does not preserve the EDL and can be inaccurate in angularly complex regions of the problem. Similar to RMC, a difference formulation has been applied to another algorithm known as the symbolic IMC method (SIMC), for the case of 1D frequency-dependent problems [?]. SIMC forms a standard FE solution to the material energy balance equation, and uses symbolic weights in the MC transport to solve for expansion coefficients. The difference formulation modifies the transport equation to solve for unknowns representing the deviation of the intensity from equilibrium with the material energy. The difference formulation was also applied to a linear-discontinuous FE spatial representation of the emission source, demonstrating accuracy in the EDL [?]. Both [?] and [?] produced minimal statistical noise in slowly varying problems where the behavior of the system is near equilibrium.

1.3 Overview of the HOLO Algorithm

The research proposed herein provides a new HOLO algorithm for radiative transfer. In this work, we propose an S_2 -like LO operator [?] in conjunction with an exponentially-convergent MC (ECMC) method [3] for the HO solver. Our LO system and approach to enforcing consistency contrast greatly from the typical formulation in [?, ?, ?]. We have derived the LO operator directly from the transport

equation, using a linear-discontinuous finite-element (LD FE) spatial discretization. Exponentially-convergent Monte Carlo (ECMC)[3, ?] provides an iterative algorithm that can efficiently reduce statistical noise to acceptable levels with significantly less particle histories than standard MC. In particular, ECMC is exceptionally efficient in time-dependent TRT problems because information about the intensity from the previous time step can be used as an accurate initial guess for the new end of time step intensity. However, implementation of ECMC is non-trivial, requiring a finite-element representation of the solution in all phase-space variables that are being sampled with MC. The method contains many of the desired qualities, such as preserving the equilibrium diffusion limit, preserving the maximum principle, and in particular, providing high-fidelity MC solution to the TRT equations in an efficient manner.

Sufficient MC histories must be performed to eliminate statistical noise in the consistency terms that can contaminate the LO solution. Exponentially-convergent Monte Carlo (ECMC)[3, ?] provides an algorithm that can efficiently reduce statistical noise to the same order as the HOLO iteration error with significantly less particle histories than standard MC. In particular, ECMC is exceptionally efficient in time-dependent TRT problems because information about the intensity from the previous time step can be used as an accurate initial guess for the new end of time step intensity. Additionally, no particle histories are required in regions where the radiation and material energy field are in equilibrium, similar to [?]. However, implementation of ECMC is non-trivial, requiring a finite-element representation of the solution in all phase-space variables that are being sampled with MC. The fundamental transport of particles is the same as standard Monte Carlo transport codes, but the source will now contain positive and negative weight particles.

1.3.1 Similarities to Residual Monte Carlo

Our ECMC solver contains similarities to the residual Monte Carlo (RMC) HO solver in [?], with some key differences. The RMC algorithm uses a particular, fixed estimate of the solution to significantly reduce the statistical noise in the simulation compared to a standard MC simulation. The guess for the solution is chosen to produce only sources on the faces of cells, reducing the dimension of the phase-space to be sampled [?]. The RMC algorithm uses a piecewise constant trial space representation for the intensity in x and μ . The primary difference between the methods is that ECMC iteratively estimates the solution, in batches, producing a known MC estimate of the error in that estimate. The ECMC algorithm projects the intensity onto a linear-discontinuous finite-element (LDFE) trial space, although the RMC algorithm could similarly be formulated with an LDFE representation. Adaptive mesh-refinement can be used in ECMC to produce highly accurate solutions with minimal statistical noise, as long as sufficient particle histories are performed. The formulation of the residual in [?] use an estimate of the solution such that only face sources need to be sampled. This residual formulation can produce minimal statistical noise in slowly varying problems where the behavior of the system is near equilibrium. Our ECMC algorithm has similar statistical efficiency by choosing the previous time step intensity as the initial guess to the algorithm; however, a linear volumetric source must be sampled in addition to face sources. The ECMC algorithm will generally be more efficient in cases where the solution varies greatly over a time step or when very low statistical noise is desired. Generally, the minimum number of histories per batch to obtain convergence with the LDFE trial space is larger than a piece-wise constant representation because additional histories are needed to sufficiently estimate the first moment in x and μ of the intensity. It is noted that

our formulation of the LO equations and consistency terms contrast greatly from the typical formulation in [?, ?, ?].

In this work, we demonstrate the utility of an S_2 -like LO operator [?] in conjunction with an ECMC method [3] for the HO solver. The ECMC algorithm uses information about the intensity from the previous time step to reduce statistical noise to the same order as the HOLO iteration error with significantly less particle histories than standard MC simulations, with less computational cost than IMC per history. We have derived the LO operator directly from the transport equation, using a linear-discontinuous (LD) finite-element (FE) spatial discretization for the HO and LO solutions. Herein we describe the algorithm and present results for 1D, gray test problems.

1.4 Dissertation Layout

This document describes dissertation research over a new Monte Carlo algorithm for solution of thermal radiative transfer problems. Herein, a brief description of thermal radiative transfer and the model problem are given, followed by a discussion of the standard Monte Carlo solution method and other related research. An overview of the methodology and results performed thus far are given in Sec. ???. Then, the remaining topics for completing this dissertation research are discussed in Sec. ??. Finally, Sec. ?? provides a specific outline of the remaining research to be investigated and computational results to be generated.

2. OVERVIEW OF THE HOLO ALGORITHM

For simplicity, our HOLO method will use a backwards Euler discretization in time, as well as constant specific heats and cell-wise constant cross sections. The time-discretized equations are

$$\mu \frac{\partial I^{n+1}}{\partial x} + \left(\sigma_t^{n+1} + \frac{1}{c\Delta t} \right) I^{n+1} = \frac{\sigma_s}{2} \phi^{n+1} + \frac{1}{2} (\sigma_a a c T^4)^{n+1} + \frac{I^n}{c\Delta t} \quad (2.1)$$

$$\rho c_v \frac{T^{n+1} - T^n}{\Delta t} = \sigma_a^{n+1} \phi^{n+1} - \sigma_a a c (T^4)^{n+1}, \quad (2.2)$$

where Δt is the uniform time step size, the superscript n is used to indicate the n -th time step. Cross sections are evaluated at the end of time step temperature, i.e., $\sigma_a^{n+1} \equiv \sigma_a(T^{n+1})$. It is noted that in IMC the time derivative in Eq. (??) is typically treated continuously using time-dependent MC over each time step. Our HO transport equation is discrete in time for simpler application of ECMC and to avoid difficulties in coupling to the fully-discrete LO solver. However, this does introduce some artificial propagation of energy due to the implicit time differencing in optically thin regions.

In the HOLO context, the LO solver models isotropic scattering and resolves the material temperature spatial distribution $T(x)$ at each time step. The LO equations are formed via half-range angular and spatial moments of Eq. (2.1) and Eq. (2.2). The spatial moments are formed over a finite-element mesh and linear-discontinuous representation of the temperature is used to close the system. The angular treatment in the LO equations has the same form as those used in the hybrid-S₂ method in [?], with consistency parameters that represent angularly-weighted averages of the intensity. These consistency parameters are analogous to a variable Eddington factor [?].

If the angular consistency parameters were exact, then the LO equations are exact, neglecting spatial discretization errors. These consistency parameters are lagged in each LO solve, estimated from the previous HO solution for $I^{n+1}(x, \mu)$, as explained below. For the initial LO solve for each time step, the parameters are calculated with $I^n(x, \mu)$. The discrete LO equations always conserve total energy, independent of the accuracy of the consistency terms. The LO system uses a LDFE spatial discretization for the temperature and half-range scalar intensities. The LDFE spatial discretization should correctly preserve the equilibrium diffusion limit, a critical aspect for TRT equations [?, ?]. Additionally, the implicit time discretization with sufficient convergence of the nonlinear emission source will ensure that the method will not exhibit maximum principle violations [?].

If the angular consistency parameters were estimated exactly, then the LO equations preserve the exact angular-averaged solution, neglecting spatial discretization errors. These consistency parameters are lagged in each LO solve, estimated from the previous HO solution for the intensity, or from a previous time step. The discrete LO equations always conserve total energy, independent of the accuracy of the consistency terms. It is noted that our LO operator is different from the nonlinear diffusion acceleration (NDA) methods used by other HOLO methods [?, ?, ?]. In NDA methods, an artificial term is added to the LO equations to enforce consistency and estimated using a previous HO solution. In our method we have simply algebraically manipulated space-angle moment equations to produce our consistency terms, which will hopefully produce more stability in optically-thick regions where NDA methods demonstrate stability issues.

The solution to the LO system is used to construct a LDFE spatial representation of the isotropic scattering and emission sources on the right hand side of Eq. (2.1). The LDFE representation of the emission source mitigates teleportation error. This

defines a fixed-source, pure absorber transport problem for the HO operator. This HO transport problem represents a characteristic method that uses MC to invert the continuous streaming plus removal operator with an LDFF representation of sources; the representation of sources is similar to the linear moments method discussed in [?]. We will solve this transport problem using ECMC. The output from ECMC is $\tilde{I}^{n+1}(x, \mu)$, a space-angle LDFF projection of the exact solution $I^{n+1}(x, \mu)$ to the described transport problem. Once computed, $\tilde{I}^{n+1}(x, \mu)$ is used to directly evaluate the necessary consistency parameters for the next LO solve. Since there is a global, functional representation of the angular intensity, LO parameters are estimated using quadrature and do not require additional tallies. The HO solution is not used to directly estimate a new temperature at the end of the time step; it is only used to estimate the angular consistency parameters for the LO equations, which eliminates typical operator splitting stability issues that require linearization of the emission source.

The process of performing subsequential HO and LO solves, within a single time step, can be repeated to obtain an increasingly accurate solution for $\phi^{n+1}(x)$ and $T^{n+1}(x)$. Thus, the HOLO algorithm, for the n -th time step, is

1. Perform a LO solve to produce an initial guess for $T^{n+1,0}(x)$ and $\phi^{n+1,0}(x)$, based on consistency terms estimated with \tilde{I}^n .
2. Solve the HO system for $\tilde{I}^{n+1,k+1/2}(x, \mu)$ with ECMC, based on the current LO estimate of the emission and scattering sources.
3. Compute LO consistency parameters with $\tilde{I}^{n+1,k+1/2}$.
4. Solve the LO system with HO consistency parameters to produce a new estimate of $\phi^{n+1,k+1}$ and $T^{n+1,k+1}$.

5. Optionally repeat 2 – 4 until desired convergence is achieved.

6. Store $\tilde{I}^n \leftarrow \tilde{I}^{n+1}$, and move to the next time step.

where the superscript k denotes the outer HOLO iteration. The consistency terms force the HO and LO solutions for $\phi^{n+1}(x)$ to be consistent to the order of the current HOLO iteration error, as long as the LDFE spatial representation can accurately represent $\phi(x)$ and $T(x)$.

3. THE MOMENT-BASED LOW-ORDER EQUATIONS

The formulation of the LO equations is similar to a discontinuous FE method. Weighted integrals of the the equations are taken with functions that have local support as weight functions. The equations are written with element-wise moments of I and T as unknowns. Leaving the solution in this form allows for use of information from a previous HO solution to eliminate auxillary unknowns from the equations. This is different than a standard Galerkin FE method [?] where a functional form of the solution is directly assumed. The final equations will have a similar form to S_2 equations, but we have not used a collocation method in angle, which should limit ray effects [?] in higher spatial dimensions. The equations eliminate extra spatial unknowns in a manner similar to to a linear-discontinuous FE method [?]. We also explore the possibility of using the MC solution to modify the discretization of the LO solution in Sec. 8.6. MOVE

The remainder of this chapter is structured as follows: the general moments will be derived and then the angular and spatial closure are discussed REWRITE. For simplicity, the backward Euler time discretization is used throughout this section. Sec. ?? will use the HO solution and MC transport to consistently close the equations in time, improving time accuracy.

3.1 Forming the Space-Angle Moment Equations

3.1.1 *LO Spatial mesh and Finite-Element Spatial Moments*

The LO equations are formulated over a FE mesh. The domain for the i -th spatial element (or cell) has support $x \in [x_{i-1/2}, x_{i+1/2}]$ with width $h_i = x_{i+1/2} - x_{i-1/2}$ and cell center $x_i = x_{i-1/2} + h_i/2$. There is a total of N_c elements, spanning the spatial domain $0 \leq x \leq X$. For simplicity, this spatial mesh is fixed throughout the

simulation. Mesh adaptation is only applied in the HO solver.

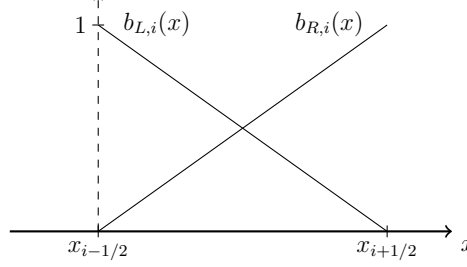


Figure 3.1: Illustration of linear finite element basis functions $b_{L,i}(x)$ and $b_{R,i}(x)$ for spatial element i .

The spatial moments are defined by integrals weighted with the standard linear finite element (FE) interpolatory basis functions. An illustration of the two linear FE basis functions for the i -th element is given in Fig. 5.1. The left basis function is defined as

$$b_{L,i}(x) = \begin{cases} \frac{x_{i+1/2}-x}{h_i} & x_{i-1/2} \leq x \leq x_{i+1/2} \\ 0 & \text{elsewhere} \end{cases}, \quad (3.1)$$

corresponding to the node $x_{i-1/2}$. The right basis function is

$$b_{R,i}(x) = \begin{cases} \frac{x-x_{i-1/2}}{h_i} & x_{i-1/2} \leq x \leq x_{i+1/2} \\ 0 & \text{elsewhere} \end{cases}, \quad (3.2)$$

corresponding to the node $x_{i+1/2}$. With these definitions, a local linear approximation to a function f can be formulated as $f(x) \simeq f_{L,i}b_{L,i}(x) + f_{R,i}b_{R,i}(x)$, $x \in [x_{i-1/2}, x_{i+1/2}]$.¹

¹In literature the FE functions are formally defined with support over two adjacent elements. However, in our notation our functions only have non-zero support in element i . This accommodates our later definition of moments and discontinuous unknowns.

The spatial moments are defined by integrals over the each element, using the two basis functions. We use $\langle \cdot \rangle$ to indicate integration over a spatial element. The spatial moments are

$$\langle \cdot \rangle_{L,i} = \frac{2}{h_i} \int_{x_{i-1/2}}^{x_{i+1/2}} b_{L,i}(x)(\cdot)dx \quad (3.3)$$

and

$$\langle \cdot \rangle_{R,i} = \frac{2}{h_i} \int_{x_{i-1/2}}^{x_{i+1/2}} b_{R,i}(x)(\cdot)dx. \quad (3.4)$$

where the factor of $2/h_i$ is a normalization constant. It is noted in this notation $\langle \phi \rangle_{L,i}$ and $\langle \phi \rangle_{R,i}$ represent spatial moments of the intensity over cell i , opposed to $\phi_{L,i}$ and $\phi_{R,i}$, which represent the interior value of the linear representation of $\phi(x)$ at $x_{i-1/2}$ and $x_{i+1/2}$ within the cell.

To simplify notation and discussion, we also define the slope and average moments over a spatial cell. The average scalar intensity is

$$\phi_i = \frac{1}{h_i} \int_{x_{i-1/2}}^{x_{i+1/2}} \phi(x)dx \quad (3.5)$$

and

$$\phi_{x,i} = \frac{6}{h_i} \int_{x_{i-1/2}}^{x_{i+1/2}} \left(\frac{x - x_i}{h_i} \right) \phi(x)dx. \quad (3.6)$$

The linear representation over a cell in terms of these moments is $\phi(x) = \phi_i + 2\phi_{x,i}(x - x_i)/h_i^2$, for $x \in (x_{i-1/2}, x_{i+1/2})$.

3.1.2 Definition of Angular Moments

To reduce the angular dimensionality, positive and negative half-range integrals of the angular intensity are taken. The angular integrals are denoted with a superscript as

$$(\cdot)^\pm = \pm \int_0^{\pm 1} (\cdot) d\mu \quad (3.7)$$

The half-range integrals of I are defined as $\phi^+(x, t) = \int_0^1 I(x, \mu, t) d\mu$ and $\phi^-(x, t) = 2\pi \int_{-1}^0 I(x, \mu, t) d\mu$, respectively. Thus, in terms of half-range quantities, the mean intensity is $\phi = \phi^- + \phi^+$. It is noted that in this notation the flux is defined as $J = J^- + J^+$, which is not the standard definition for the half-range fluxes, e.g., in [2].

3.1.3 Space-Angle Moments of the Radiation Transport Equation

The LO radiation equations are formed by applying the space and angle moment operators to the transport equation and performing algebraic manipulation. We provide a detailed derivation of the L and $+$ radiation moment equation and state the final results for the other moment operators. First, the L moment operator is applied to the time-discretized transport equation, i.e., Eq. (2.1). Integration by parts on the streaming term yields

$$\begin{aligned}
& -\frac{2}{h_i} \mu_{i-1/2} I_{i-1/2}^{n+1} + \frac{2}{h_i^2} \int_{x_{i-1/2}}^{x_{i+1/2}} \mu I^{n+1} dx + \left(\sigma_{t,i}^{n+1} + \frac{1}{c\Delta t} \right) \langle \phi \rangle_{L,i}^{n+1,+} \\
& - \frac{\sigma_{s,i}}{2} \langle \phi \rangle_{L,i}^{n+1} = \frac{1}{2} \langle \sigma_a^{n+1} ac T^{n+1,4} \rangle_{L,i} + \frac{1}{c\Delta t} \langle \phi \rangle_{L,i}^{n,+}. \quad (3.8)
\end{aligned}$$

Here, the cross sections have been assumed constant over a cell. The mean intensity in the scattering term is expanded in terms of half-range unknowns. The integral can be rewritten in terms of L and R moments by noting that $b_{L,i}(x) + b_{R,i}(x) = 2/h_i$. These substitutions are made and the resulting equation is multiplied by h_i to produce

$$\begin{aligned}
& -2\mu_{i-1/2} I_{i-1/2}^{n+1} + \langle \mu I^{n+1} \rangle_{L,i} + \langle \mu I^{n+1} \rangle_{R,i} + \left(\sigma_{t,i}^{n+1} + \frac{1}{c\Delta t} \right) h_i \langle \phi \rangle_{L,i}^{n+1,+} \\
& - \frac{\sigma_{s,i} h_i}{2} (\langle \phi \rangle_{L,i}^{n+1,+} + \langle \phi \rangle_{L,i}^{n+1,-}) = \frac{h_i}{2} \langle \sigma_a^{n+1} ac T^{n+1,4} \rangle_{L,i} + \frac{h_i}{c\Delta t} \langle \phi \rangle_{L,i}^{n,+}. \quad (3.9)
\end{aligned}$$

The resulting equation is integrated over the positive half range:

$$\begin{aligned}
& -2 \left(\mu_{i-1/2} I_{i-1/2}^{n+1} \right)^+ + \langle \mu I^{n+1} \rangle_{L,i}^+ + \langle \mu I^{n+1} \rangle_{R,i}^+ + \left(\sigma_{t,i}^{n+1} + \frac{1}{c\Delta t} \right) h_i \langle \phi \rangle_{L,i}^{n+1,+} \\
& - \frac{\sigma_{s,i} h_i}{2} \left(\langle \phi \rangle_{L,i}^{n+1,+} + \langle \phi \rangle_{L,i}^{n+1,-} \right) = \frac{h_i}{2} \langle \sigma_a^{n+1} a c T^{n+1,4} \rangle_{L,i} + \frac{h_i}{c\Delta t} \langle \phi \rangle_{L,i}^{n,+}. \quad (3.10)
\end{aligned}$$

3.1.4 The Angular Consistency Terms

Now, algebraic manipulations are performed on the streaming terms to produce face and volume-averaged values of μ , weighted by the intensity. Each term in the streaming term is multiplied by a factor of unity, with the desired unknown appropriate to each term in the numerator and denominator. Temporarily dropping the time index for clarity, the manipulations applied to the streaming term are as follows:

$$\left\langle \mu \frac{\partial I}{\partial x} \right\rangle_L^+ = -\frac{2}{h_i} (\mu I_{i-1/2})^+ + \frac{1}{h_i} [\langle \mu I \rangle_{L,i}^+ + \langle \mu I \rangle_{R,i}^+] \quad (3.11)$$

$$= -\frac{2}{h_i} (\mu I_{i-1/2})^+ \frac{(I_{i-1/2})^+}{(I_{i-1/2})^+} + \frac{1}{h_i} \left[\langle \mu I \rangle_{L,i}^+ \frac{\langle I \rangle_{L,i}^+}{\langle I \rangle_{L,i}^+} + \langle \mu I \rangle_{R,i}^+ \frac{\langle I \rangle_{R,i}^+}{\langle I \rangle_{R,i}^+} \right] \quad (3.12)$$

$$= -\frac{2}{h_i} \left\{ \frac{(\mu I)_{i-1/2}^+}{\phi_{i-1/2}^+} \right\} \phi_{i-1/2}^+ + \frac{1}{h_i} \left[\left\{ \frac{\langle \mu I \rangle_{L,i}^+}{\langle \phi \rangle_{L,i}^+} \right\} \langle \phi \rangle_{L,i}^+ + \left\{ \frac{\langle \mu I \rangle_{R,i}^+}{\langle \phi \rangle_{R,i}^+} \right\} \langle \phi \rangle_{R,i}^+ \right] \quad (3.13)$$

The ratios in braces are what we will formally define as *angular consistency terms*. These nonlinear functionals are approximated by the HO solver. The angular consistency term for the L and $+$ moments is defined as

$$\{\mu\}_{L,i}^{n+1,+} \equiv \frac{\langle \mu I^{n+1} \rangle_{L,i}^+}{\langle I^{n+1} \rangle_{L,i}^+} = \frac{\frac{2}{h_i} \int_0^1 \int_{x_{i-1/2}}^{x_{i+1/2}} \mu b_{L,i}(x) I^{n+1}(x, \mu) dx d\mu}{\frac{2}{h_i} \int_0^1 \int_{x_{i-1/2}}^{x_{i+1/2}} b_{L,i}(x) I^{n+1}(x, \mu) dx d\mu}. \quad (3.14)$$

The consistency terms on the face represent averaging at a point, with a similar definition as

$$\mu_{i+1/2}^+ \equiv \frac{(\mu I_{i+1/2})^+}{\phi_{i+1/2}^+} = \frac{\int_0^1 \mu I(x_{i+1/2}, \mu) d\mu}{\int_0^1 I(x_{i+1/2}, \mu) d\mu}. \quad (3.15)$$

There are analogous definitions for the R and $-$ moments. The moment of the streaming term for the L and $+$ operators becomes

$$\left\langle \mu \frac{\partial I}{\partial x} \right\rangle_L^+ = -\frac{2}{h_i} \mu_{i-1/2}^+ I_{i-1/2}^+ + \frac{1}{h_i} \left[\{\mu\}_{L,i}^+ \langle \phi \rangle_{L,i}^+ + \{\mu\}_{R,i}^+ \langle \phi \rangle_{R,i}^+ \right] \quad (3.16)$$

It is noted that this expression does not contain a cross section in the denominator, such as in the variable Eddington factor approach [?], thus this method will be stable in a void.

3.1.5 The Exact Radiation Moment Equations

A final expression for the moment equation resulting from application of the L moment and positive half-range integral is obtained by substituting the result of Eq. (5.16) into Eq. (5.10):

$$\begin{aligned} & -2\mu_{i-1/2}^{n+1,+} \phi_{i-1/2}^{n+1,+} + \{\mu\}_{L,i}^{n+1,+} \langle \phi \rangle_{L,i}^{n+1,+} + \{\mu\}_{R,i}^{n+1,+} \langle \phi \rangle_{R,i}^{n+1,+} + \left(\sigma_{t,i}^{n+1} + \frac{1}{c\Delta t} \right) h_i \langle \phi \rangle_{L,i}^{n+1,+} \\ & - \frac{\sigma_{s,i} h_i}{2} (\langle \phi \rangle_{L,i}^{n+1,+} + \langle \phi \rangle_{L,i}^{n+1,-}) = \frac{h_i}{2} \langle \sigma_a^{n+1} a c T^{n+1,4} \rangle_{L,i} + \frac{h_i}{c\Delta t} \langle \phi \rangle_{L,i}^{n,+}, \quad (3.17) \end{aligned}$$

Similar derivations can be used to derive the other radiation moment equations. Pairwise application of the L and R basis moments with the $+$ and $-$ half-range integrals to Eq. (??) ultimately yields four moment equations per cell. The equation

for the R and $+$ moment is

$$2\mu_{i+1/2}^{n+1,+} \phi_{i+1/2}^{n+1,+} - \{\mu\}_{L,i}^{n+1,+} \langle \phi \rangle_{L,i}^{n+1,+} - \{\mu\}_{R,i}^{n+1,+} \langle \phi \rangle_{R,i}^{n+1,+} + \left(\sigma_{t,i}^{n+1} + \frac{1}{c\Delta t} \right) h_i \langle \phi \rangle_{R,i}^{n+1,+} - \frac{\sigma_{s,i} h_i}{2} (\langle \phi \rangle_{R,i}^{n+1,+} + \langle \phi \rangle_{R,i}^{n+1,-}) = \frac{h_i}{2} \langle \sigma_a^{n+1} acT^{n+1,4} \rangle_{R,i} + \frac{h_i}{c\Delta t} \langle \phi \rangle_{R,i}^{n,+}, \quad (3.18)$$

The equations for the negative half-range moment are identical to the above with the negative half-range superscripts replacing the positive. Explicitly,

$$-2\mu_{i-1/2}^{n+1,-} \phi_{i-1/2}^{n+1,-} + \{\mu\}_{L,i}^{n+1,-} \langle \phi \rangle_{L,i}^{n+1,-} + \{\mu\}_{R,i}^{n+1,-} \langle \phi \rangle_{R,i}^{n+1,-} + \left(\sigma_{t,i}^{n+1} + \frac{1}{c\Delta t} \right) h_i \langle \phi \rangle_{L,i}^{n+1,-} - \frac{\sigma_{s,i} h_i}{2} (\langle \phi \rangle_{L,i}^{n+1,+} + \langle \phi \rangle_{L,i}^{n+1,-}) = \frac{h_i}{2} \langle \sigma_a^{n+1} acT^{n+1,4} \rangle_{L,i} + \frac{h_i}{c\Delta t} \langle \phi \rangle_{L,i}^{n,-} \quad (3.19)$$

and

$$2\mu_{i+1/2}^{n+1,-} \phi_{i+1/2}^{n+1,-} - \{\mu\}_{L,i}^{n+1,-} \langle \phi \rangle_{L,i}^{n+1,-} - \{\mu\}_{R,i}^{n+1,-} \langle \phi \rangle_{R,i}^{n+1,-} + \left(\sigma_{t,i}^{n+1} + \frac{1}{c\Delta t} \right) h_i \langle \phi \rangle_{R,i}^{n+1,-} - \frac{\sigma_{s,i} h_i}{2} (\langle \phi \rangle_{R,i}^{n+1,+} + \langle \phi \rangle_{R,i}^{n+1,-}) = \frac{h_i}{2} \langle \sigma_a^{n+1} acT^{n+1,4} \rangle_{R,i} + \frac{h_i}{c\Delta t} \langle \phi \rangle_{R,i}^{n,-}, \quad (3.20)$$

Ultimately, the two half-ranges will be treated differently when the equations are closed spatially.

3.1.6 Material Energy Equations

To derive the LO material energy equations, an approximation must be introduced to relate $T(x)$ and $T^4(x)$ within a cell. We represent $T(x)$ spatially with a LDFE trial space. This trial space will ensure preservation of the equilibrium diffusion limit. To simplify the relation between $T(x)$ and $T^4(x)$ $T(x) \simeq T_{L,i} b_{L,i}(x) + T_{R,i} b_{R,i}(x)$, $x \in (x_{i-1/2}, x_{i+1/2})$. Similarly, the emission term is represented in the material and radiation equations with the LDFE interpolant $T^4(x) \simeq T_{L,i}^4 b_{L,i}(x) +$

$T_{R,i}^4 b_{R,i}(x)$. The L and R spatial moments are taken of the material energy equations; the LD FE representations for $T(x)$ and $\sigma_a a c T^4(x)$ are used to simplify the spatial integrals. The final LO material energy equation resulting from application of the L moment is

$$\begin{aligned} \frac{\rho_i c_{v,i}}{\Delta t} \left[\left(\frac{2}{3} T_{L,i} + \frac{1}{3} T_{R,i} \right)^{n+1} - \left(\frac{2}{3} T_{L,i} + \frac{1}{3} T_{R,i} \right)^n \right] + \sigma_{a,i}^{n+1} (\langle \phi \rangle_{L,i}^+ + \langle \phi \rangle_{L,i}^-)^{n+1} \\ = \sigma_{a,i}^{n+1} a c \left(\frac{2}{3} T_{L,i}^4 + \frac{1}{3} T_{R,i}^4 \right)^{n+1}. \end{aligned} \quad (3.21)$$

The equation for the R moment is

$$\begin{aligned} \frac{\rho_i c_{v,i}}{\Delta t} \left[\left(\frac{1}{3} T_{L,i} + \frac{2}{3} T_{R,i} \right)^{n+1} - \left(\frac{1}{3} T_{L,i} + \frac{2}{3} T_{R,i} \right)^n \right] + \sigma_{a,i}^{n+1} (\langle \phi \rangle_{R,i}^+ + \langle \phi \rangle_{R,i}^-)^{n+1} \\ = \sigma_{a,i}^{n+1} a c \left(\frac{1}{3} T_{L,i}^4 + \frac{2}{3} T_{R,i}^4 \right)^{n+1}. \end{aligned} \quad (3.22)$$

Cross sections have been assumed constant over each element, evaluated at the average temperature within the element, i.e., $\sigma_{a,i}^{n+1} = \sigma_{a,i}([T_{L,i}^{n+1} + T_{R,i}^{n+1}]/2)$. Because the material energy balance only contains angularly integrated quantities, there is no need to take angular moments of the above equations.

REWRITE: WHAT TO DO WITH THIS PARAGRAPH? Because there are no derivatives of T in Eq. (??), there is no need to define T on the faces. Because only moments of ϕ appear in the material energy equations, they are fully defined at this point. The LD closure for the L and $+$ equations produces

3.2 Closing the LO System with Information from the HO Solution

The six degrees of freedom (DOF) over each cell i are the four moments $\langle \phi \rangle_{L,i}^+$, $\langle \phi \rangle_{R,i}^+$, $\langle \phi \rangle_{L,i}^-$, and $\langle \phi \rangle_{R,i}^-$ and the two spatial edge values $T_{L,i}$ and $T_{R,i}$. The four

radiation and two material energy equations define a system of equations for the six DOF, coupled spatially through the streaming term. We emphasize that at this point we have not made any spatial or angular approximations to the transport moment equations; these moment equations are exact with respect to the chosen time discretization. The material energy equation has the approximation of an LD FE space for $T(x)$. Some approximation of this form is necessary to relate T and T^4 .

3.2.1 Angular Closure

The angular consistency parameters (e.g., Eq. (5.14) and (5.15)) are not known a priori. A lagged estimate of I^{n+1} from the previous HO solve is used to estimate the angular consistency parameters. In the HOLO algorithm, the equations for LO unknowns at iteration $k + 1$ use consistency parameters computed using the latest HO solution $\tilde{I}^{n+1,k+1/2}$ as an approximation for $I^{n+1}(x, \mu)$. We evaluate these terms using quadrature based on the functional form of the solution provided by the HO solution.

3.2.2 Spatial Closure

The relation between the volume and face averaged quantities must be known to eliminate the final auxiliary unknowns. To close the LO system spatially, we will explore multiple options. The simplest closure is to use a linear-discontinuous (LD) spatial closure with the usual upwinding approximation [?]. For example, for positive flow (e.g., Eq. (??)) the face terms $\mu_{i-1/2}$ and $\phi_{i-1/2}$ are upwinded from the previous cell $i - 1$ or from a boundary condition; the terms at $x_{i+1/2}$ are linearly extrapolated, computed using the L and R basis moments. By assuming $\phi^\pm(x)$ is linear over a cell, a relation between the outflow and moments can be derived, e.g., $\phi_{i+1/2}^+ = 2\langle\phi\rangle_R^+ - \langle\phi\rangle_L^+$. For the negative half range, $\phi_{i-1/2}^- = 2\langle\phi\rangle_L^- - \langle\phi_R\rangle^+$. The LD

closure, with upwinding, for the L equation and positive half-range is

$$-2\mu_{i-1/2}^{n+1,+} (2\langle\phi\rangle_{R,i-1}^+ -) + \{\mu\}_{L,i}^{n+1,+} \langle\phi\rangle_{L,i}^{n+1,+} + \{\mu\}_{R,i}^{n+1,+} \langle\phi\rangle_{R,i}^{n+1,+} + \left(\sigma_{t,i}^{n+1} + \frac{1}{c\Delta t}\right) h_i \langle\phi\rangle_{L,i}^{n+1,+} - \frac{\sigma_{s,i} h_i}{2} (\langle\phi\rangle) \quad (3.23)$$

Similar equations can be derived for the other directions, fully defining the radiation equations. These equations are equivalent to an S_2

Note that we have chosen to leave $\mu_{i-1/2}^{n+1,+}$ as a value to be estimated from the HO solver, which is more conducive to the other spatial closures described in Sec. ???. Alternatively, the spatial closure could be introduced before performing the algebraic manipulation to form consistency terms (e.g., into Eq. (5.11)). This would produce only volume-weighted consistency terms for the LD spatial closure.

3.2.2.1 Fixups to LD Solution

The linear-discontinuous (LD) closure with upwinding is not strictly positive. In particular, for optically thick cells with a steep intensity gradient, the solution becomes negative. These negative values of intensity can propagate to adjacent cells. In thick regions of TRT problems, reasonably fine spatial cells can still be on the order of millions of mean free paths; negative values with an LD representation are unavoidable in practice for such cells and mesh refinement is of minimal use. Typically, for a standard LDFE method, the equations are lumped to produce a strictly positive solution (for 1D) [?]. However, standard FE lumping procedures would introduce difficulties in computing the consistency terms from the HO solution. Thus, an alternative spatial closure is used that is equivalent to the standard FE lumping procedure. The L and R moments are defined the same as before, preserving the average within a cell, but the relation between the moments and the outflow is modified. For example, for positive μ , the outflow is now defined as $\phi_{i+1/2}^+ = \langle\phi\rangle_R^+$.

Because the basis function $b_{R,i}(x)$ is strictly positive, the outflow is positive. This closure is only used in cells where negative intensities occur.

3.2.3 *Newton's Method for LO Equations*

Adding the equations for each cell together forms a global system of coupled equations. The equations are nonlinear due to the Planckian emission source. We have used Newton's method to solve the nonlinear system, based on a typical linearization of the Planckian source with cross sections evaluated at temperatures from the previous iteration, as described in [?]. A derivation of the LO Newton equations is given in ??.

The equations for each half-range are coupled together via scattering. In one spatial dimension, the scattering terms can be included in the discrete system matrix and directly inverted. We consider an alternative iterative solution method that could be more easily extended to higher spatial dimensions in Sec. ??. Isotropic scattering, including effective scattering terms from the linearization, are included in the system matrix. The system matrix is an asymmetric, banded matrix with a band width of seven and is inverted directly. Newton iterations are repeated until $\phi^{n+1}(x)$ and $T^{n+1}(x)$ are converged to a desired relative tolerance. Convergence is calculated using the spatial L_2 norm of the change in $\phi^{n+1}(x)$ and $T^{n+1}(x)$, relative to the norm of each solution. The lumping-equivalent discretization discussed above is used for cells where the solution for ϕ^{n+1} becomes negative. When negative values for $\phi^{n+1,\pm}(x)$ are detected, the lumping-equivalent discretization is used within those cells and that Newton step is repeated.

4. THE HIGH-ORDER EXPONENTIALLY-CONVERGENT MONTE CARLO SOLVER

4.1 The ECMC High Order Solver

The transport equation to be solved by the HO solver is

$$\mu \frac{\partial I^{n+1,k+1/2}}{\partial x} + \left(\sigma_t^k + \frac{1}{c\Delta t} \right) I^{n+1,k+1/2} = \frac{\sigma_s}{2} \phi^{n+1,k} + \frac{1}{2} (\sigma_a^k a c T^4)^{n+1,k} + \frac{\tilde{I}^n}{c\Delta t} \quad (4.1)$$

where the superscript k represents the outer HOLO iteration index. Material property indices will be suppressed from now on. Here, $k + 1/2$ denotes the ECMC solution within outer HOLO iteration k , whereas k and $k + 1$ represent successive LO solves. The sources at k in Eq. (7.1) are estimated by the previous LO solution. Cross sections are evaluated at $T^{n+1,k}$. As all sources on the right side of the equation are known, this defines a fixed-source, pure absorber transport problem. We will solve this equation using ECMC. A more detailed description of the ECMC method can be found in [3], but a brief overview is given here. A general proof of exponential convergence for related adaptive MC transport methods with a different formulation is depicted in [?].

In operator notation, Eq. (7.1) can be written as

$$\mathbf{L}^k I^{n+1,k+1/2} = q^k \quad (4.2)$$

where $I^{n+1,k+1/2}$ is the transport solution of the angular intensity based on the k -th LO estimate of q^k . The linear operator \mathbf{L}^k is the continuous streaming plus removal operator defined by the left hand side of Eq. (??). The m -th approximate LDFE solution to Eq. (7.2) (m is the index of inner HO batches) is represented as $\tilde{I}^{n+1,(m)}$.

The m -th residual is defined as $r^{(m)} = q - \mathbf{L}^k \tilde{I}^{n+1,(m)}$. For reference, the residual at iteration m in the HO solve is

$$r^{(m),k+1/2} = \frac{\sigma_s}{2} \phi^{n+1,k} + \frac{1}{2} (\sigma_a a c T^4)^{n+1,k} + \frac{\tilde{I}^n}{c \Delta t} - \left(\mu \frac{\partial \tilde{I}^{n+1,k+1/2}}{\partial x} + \left(\sigma_t + \frac{1}{c \Delta t} \right) \tilde{I}^{n+1,k+1/2} \right)^{(m)} \quad (4.3)$$

where the k terms are LD in space on the coarsest mesh and are not recalculated at any point during the HO solve. The functional form of \tilde{I}^n is defined from the final HO solution of the previous time step.

Addition of $\mathbf{L}I^{n+1} - q = 0$ to the residual equation and manipulation of the result yields the error equation

$$\mathbf{L}(I^{n+1} - \tilde{I}^{n+1,(m)}) = \mathbf{L}\epsilon^{(m)} = r^{(m)} \quad (4.4)$$

where I^{n+1} is the exact solution and $\epsilon^{(m)}$ is the true error in $\tilde{I}^{n+1,(m)}$. We have suppressed the HOLO iteration indices because the LO estimated q^k and \mathbf{L}^k remain constant over the entire HO solve. The \mathbf{L} operator in the above equation is inverted yielding the Monte Carlo LDFE projection of the error in $\tilde{I}^{n+1,(m)}$, i.e.,

$$\tilde{\epsilon}^{(m)} = \mathbf{L}^{-1} r^{(m)} \quad (4.5)$$

where \mathbf{L}^{-1} is the Monte Carlo inversion of the streaming and removal operator. This inversion is strictly a standard Monte Carlo simulation. It is noted that the exact error in $\tilde{I}^{n+1,(m)}$ (with respect to Eq. (7.1)) is being estimated with MC; tallies produce a projection of the error onto a LDFE space-angle trial space. The space-angle moments of the error computed as $\tilde{\epsilon}^{(m)}$ can be added to the moments of $\tilde{I}^{n+1,(m)}$ to produce a more accurate solution.

Here, we emphasize the solution $\tilde{I}^{n+1,(m)}$ represents the LD FE projection of the exact Monte Carlo solution to the transport problem defined by Eq. (7.1). The discretization error is in q , i.e., the LD spatial representation of the emission and scattering source and the LD FE space-angle projection $\tilde{I}^n(x, \mu)$. The projection of the intensity is in general far more accurate than a standard finite element solution, e.g., a S_N collocation method in angle. In typical IMC calculations, the average energy deposition within a cell is computed using a standard path-length volumetric flux tally; the zeroth moment of the LD FE projection of ϵ is computed using an equivalent tally, preserving the zeroth moment of the true error.

Volumetric flux tallies over each space-angle element are required to estimate $\tilde{\epsilon}^{(m)}$. The LD approximation in space is used to relate the outflow within a cell to the volumetric moments, eliminating the need for face-averaged tallies. The procedure for representing the solution, sampling with negative and positive weight particles, and tally definitions are given in Appendix 7.3.

The ECMC algorithm is

1. Initialize the guess for $\tilde{I}^{n+1,(0)}$ to \tilde{I}^n or the projection of \tilde{I}^{n+1} from the latest HO solve
2. Compute $r^{(m)}$.
3. Perform a MC simulation to obtain $\tilde{\epsilon}^{(m)} = \mathbf{L}^{-1}r^{(m)}$
4. Compute a new estimate of the intensity $\tilde{I}^{n+1,(m+1)} = \tilde{I}^{n+1,(m)} + \tilde{\epsilon}^{(m)}$
5. Repeat steps 2 – 4 until desired convergence criteria is achieved.

The initial guess for the angular intensity $I^{n+1,(0)}$ is computed based on the previous solution for \tilde{I}^n . This is a critical step in the algorithm; it significantly reduces the

required number of particles per time step because the intensity does not change drastically between time steps in optically-thick regions. It is noted that the ECMC batch (steps 1-4 of the algorithm) results in essentially the same estimate of the solution as the residual formulation used in [?]. The primary difference is that our method uses an LDFF trial space and iterates on the solution estimate by recomputing the residual.

Exponential convergence is obtained if the error ϵ is reduced each batch. With each batch, a better estimate of the solution is being used to compute the new residual, decreasing the magnitude of the MC residual source at each iteration m , relative to the solution I^{n+1} . Each MC estimate of the moments of ϵ still has a statistical uncertainty that is governed by the standard $1/\sqrt{N}$ convergence rate [4], for a particular source $r^{(m)}$, where N is the number of histories performed. If the statistical estimate of the projection $\tilde{\epsilon}$ is not sufficiently accurate, then the iterations would diverge. It is noted that there is statistical correlation across batches because $I^{n+1,(m+1)}$ and $\epsilon^{(m)}$ are correlated through $I^{n+1,(m)}$ and the MC source $r^{(m)}$.

Because the exact angular intensity does not in general lie within the LDFF trial space, the iterative estimate of the error will eventually stagnate once the error cannot be sufficiently represented by a given FE mesh. An adaptive h -refinement algorithm has been implemented that can be used to allow the system to continue converging towards the exact solution [3, ?]. For TRT problems where absorption-reemission physics dominate, the diffusive and slowly varying regions of the problem require a less refined angular mesh to capture the solution than typical neutronics problems. However, greater spatial resolution is needed due to steep spatial gradients. Once error stagnation has occurred (and mesh refinement has reached a maximum level), additional histories can be performed with a fixed residual source to estimate the remaining error in the current solution. Although the remaining error will converge

statistically at a standard $1/\sqrt{N}$ convergence rate, the remaining error will be much smaller than for a standard MC simulation, producing a much more efficient solution method overall.

For the HO solver, in cells near the radiation wavefront, the LDFE trial space results in negative values in $\tilde{I}^{n+1}(x, \mu)$, similar to the LO solver. Because the residual formulation in ECMC allows for negative weight particles to occur, currently we do not treat these cells specially. We detect if the consistency terms lie in the appropriate half space at the end of the HO solve, an indication that the intensity was negative within that cell. If the terms are non-physical, then they are replaced with the corresponding S₂-equivalent value. In general, in such cells where the trial space cannot accurately represent the solution, error stagnation will rapidly occur.

4.2 MC solution with LDD trial space

The inclusion of the outflow discontinuity has a minimal effect on the treatment of the residual source. The residual source and process of estimating moments of the error on the interior of a space-angle cell is unchanged. The process of estimating the solution on the outgoing face requires tallying the solution when particles leave a cell. The tallying process is discussed later in Section 8.7.

Applying L to the LDD trial space, as shown in Fig. ??, results in two δ functions at each interior face. For positive flow, at a face $x_{i+1/2}$, the face portion of the residual is defined as

$$r_{\text{face}}(x_{i+1/2}) = -\mu \frac{\partial \tilde{I}^{(m)}}{\partial x} \Big|_{x_{i+1/2}} \quad (4.6)$$

$$= r_{\text{face}}(x_{i+1/2}^-) \delta^-(x - x_{i+1/2}) + r_{\text{face}}(x_{i+1/2}^+) \delta^+(x - x_{i+1/2}) \quad (4.7)$$

where

$$r_{\text{face}}(x_{i+1/2}^-) = -\mu \left(\tilde{I}^{(m)}(x_{i+1/2}, \mu) - \tilde{I}^{(m)}(x_{i+1/2}^-, \mu) \right) \quad (4.8)$$

$$r_{\text{face}}(x_{i+1/2}^+) = -\mu \left(\tilde{I}^{(m)}(x_{i+1/2}^+, \mu) - \tilde{I}^{(m)}(x_{i+1/2}, \mu) \right). \quad (4.9)$$

Here, $I^{(m)}(x_{i+1/2}^+)$ and $I^{(m)}(x_{i+1/2}^-)$ are the LD solution extrapolated to $x_{i+1/2}$ from the x cell i and cell $i + 1$, respectively. Particles sampled from the two δ -functions have the same starting location. The only difference is, for positive μ , particles sampled from $r_{\text{face}}(x_{i+1/2}^-)$ will contribute to the face tally at $x_{i+1/2}$; the opposite is true for negative μ .

To reduce variance, we do not sample the two δ functions independently. Instead, we combine the two δ -functions into a single face source, do not score particles at the face from which they are sampled. To account for the untallied error, we add the analytic contribution to the error from the face source to the corresponding face at the end of a batch. It is noted the combination of the two δ -functions produces the same residual source as the original LD residual.

Define the additional error contribution from the face sources at $x_{i+1/2}$ as $\delta\epsilon^{(m)}$. This additional error is tallied everywhere by MC, except for at $x_{i+1/2}$. The transport equation satisfied by $\delta\epsilon^{(m)}$, for positive μ , with effective total cross section $\hat{\sigma}_t$, is

$$\mu \frac{\partial \delta\epsilon^{(m)}}{\partial x} + \hat{\sigma}_t \delta\epsilon^{(m)} = r_{\text{face}}(x_{i+1/2}^-) \delta^-(x - x_{i+1/2}) + r_{\text{face}}(x_{i+1/2}^+) \delta^+(x - x_{i+1/2}) \quad (4.10)$$

This equation is integrated from $x_{i+1/2} - \alpha$ to $x_{i+1/2}$ to produce

$$\mu \delta\epsilon^{(m)}(x_{i+1/2}, \mu) - \mu \delta\epsilon^{(m)}(x_{i+1/2} - \alpha, \mu) + \int_{x_{i+1/2} - \alpha}^0 \hat{\sigma}_t \delta\epsilon^{(m)} dx$$

$$= r_{\text{face}}(x_{i+1/2}^-) + \int_{x_{i+1/2}-\alpha}^0 r_{\text{face}}(x_{i+1/2}^+) \delta^+(x - x_{i+1/2}) dx. \quad (4.11)$$

The integral on the right side of the equation is zero because $\delta^+(x - x_{i+1/2})$ is zero for $(-\infty, x_{i+1/2}]$. The limit of the above equation is taken as $\alpha \rightarrow 0$, i.e.,

$$\lim_{\alpha \rightarrow 0} \left(\mu \delta \epsilon^{(m)}(x_{i+1/2}, \mu) - \mu \delta \epsilon^{(m)}(x_{i+1/2} - \alpha, \mu) + \int_{x_{i+1/2}-\alpha}^0 \hat{\sigma}_t \delta \epsilon^{(m)} dx \right) = \lim_{\alpha \rightarrow 0} r_{\text{face}}(x_{i+1/2}^-) \quad (4.12)$$

The integral goes to zero because $\delta \epsilon^{(m)}$ is smooth on the interior of the cell, and $\mu \delta \epsilon^{(m)}(x_{i+1/2} - \alpha, \mu)$ goes to zero because there is no source upstream of $x_{i+1/2}^-$. Thus, the final solution is

$$\delta \epsilon^{(m)}(x_{i+1/2}, \mu) = \frac{r_{\text{face}}(x_{i+1/2}^-)}{\mu} = \tilde{I}^{(m)}(x_{i+1/2}^-, \mu) - \tilde{I}^{(m)}(x_{i+1/2}, \mu). \quad (4.13)$$

The update for $I(x_{i+1/2}, \mu)$ is

$$\tilde{I}^{(m+1)}(x_{i+1/2}, \mu) = \tilde{I}^{(m)}(x_{i+1/2}, \mu) + \epsilon^{(m)}(x_{i+1/2}, \mu) + \delta \epsilon^{(m)}(x_{i+1/2}, \mu) \quad (4.14)$$

$$= \tilde{I}^{(m)}(x_{i+1/2}^-, \mu) + \epsilon^{(m)}(x_{i+1/2}, \mu). \quad (4.15)$$

This result has the peculiar effect that the estimation of the solution on a face depends only on the interior solution $\tilde{I}^{(m)}(x_{i+1/2}^-, \mu)$ and not the previous face value $\tilde{I}^{(m)}(x_{i+1/2}, \mu)$. This could be used to only estimate face values in particular cells, at any chosen batch.

4.3 Implementation of ECMC finite-element space, tallies, and residual sampling

The ECMC solver uses a finite element representation in space and angle. On the interior of the cell with the i -th spatial index and j -th angular index, the linear representation is defined as

$$\tilde{I}(x, \mu) = I_{a,ij} + \frac{2}{h_x} I_{x,ij} (x - x_i) + \frac{2}{h_\mu} I_{\mu,ij} (\mu - \mu_j), \quad x_{i-1/2} < x < x_{i+1/2}, \quad \mu_{j-1/2} \leq \mu \leq \mu_{j+1/2}$$

The spatial cell width is h_x , the angular width is h_μ , the center of the cell is (x_i, μ_j) , and

$$I_{a,ij} = \frac{1}{h_x h_\mu} \iint_{\mathcal{D}} I(x, \mu) dx d\mu \quad (4.16)$$

$$I_{x,ij} = \frac{6}{h_x h_\mu} \iint_{\mathcal{D}} \left(\frac{x - x_i}{h_x} \right) I(x, \mu) dx d\mu \quad (4.17)$$

$$I_{\mu,ij} = \frac{6}{h_x h_\mu} \iint_{\mathcal{D}} \left(\frac{\mu - \mu_j}{h_\mu} \right) I(x, \mu) dx d\mu, \quad (4.18)$$

where $\mathcal{D} : x_{i-1/2} \leq x \leq x_{i+1/2} \times \mu_{j-1/2} \leq \mu \leq \mu_{j+1/2}$. Standard upwinding in space is used to define $I(\mu)$ on incoming faces.

This representation can directly be plugged into Eq. (7.3) and evaluated to produce the residual source in the ECMC HO transport problem. The MC source $r^{(m)}(x, \mu)$ in Eq. (7.5) consists of both face and volumetric sources and can produce positive and negative weight particles. The distribution for sampling particle coordinates, in space and angle, is based on the L_1 norm over space and angle of the residual [3]. A particular cell volume or face is sampled, and then rejection sampling [4] is used to sample from the appropriate distribution on the face or interior of the space-angle cell. If the residual is negative at the sampled coordinates, the

weight of the particle history is negative.

During a MC batch, moments of the error are tallied. The necessary moments of the error are defined analogously to Eq.'s (7.16)–(7.18). The tallies are evaluated by weighting the particle density with the appropriate basis function and integrating along the history path through the cell. For the cell average, the n -th particle makes the contribution

$$\epsilon_{a,ij}^n = \frac{1}{h_x h_\mu} \int_{s_o^n}^{s_f^n} w^n(x, \mu) ds, \quad (4.19)$$

where s_o^n and s_f^n are the beginning and end of the n -th particle track in the cell and $w(x, \mu)$ is the weight of the error particle in the MC simulation. Weight is attenuated exponentially, i.e., $w(x, \mu) \propto \exp(-\sigma_t |x/\mu|)$. Substitution of the exponential attenuation of the weight produces the result

$$\epsilon_{a,ij}^n = \frac{w(x_0, \mu)}{\sigma_t h_x h_\mu} (1 - e^{-\sigma_t s^n}). \quad (4.20)$$

Here, $w(x_0, \mu)$ is the particle weight at the start of the path and s^n is the length of the track. The contribution of a particle track to ϵ_x is given by

$$\epsilon_{x,ij}^n = \frac{w(x_0, \mu)}{h_x^2 h_\mu \sigma_t} \left[x_0 - x_f e^{-\sigma_t s^n} + \left(\frac{\mu}{\sigma_t} - x_i \right) (1 - e^{-\sigma_t s^n}) \right], \quad (4.21)$$

where x_0 and x_f are the beginning and ending x coordinates of the n -th path. The contribution to the first moment in μ is

$$\epsilon_{\mu,ij}^n = \frac{w(x_0, \mu)}{h_\mu^2 h_x \sigma_t} (\mu - \mu_j) (1 - e^{-\sigma_t s^n}), \quad (4.22)$$

where the particle x -direction cosine μ does not change because it is a pure-absorber simulation. Finally, the moments of the error are simply the average contribution of

all particles.

4.4 Adaptive Mesh Refinement

This section describes the adaptive refinement strategy for the ECMC algorithm. Detailed equations for performing projections between meshes and computing the residual source on the refined meshes can be found in [3]. At the end of the ECMC batch, refinement is performed in space-angle cells based on a jump indicator. The jump indicator is the magnitude of the different between $I(x, \mu)$ in adjacent cells, averaged over each edge. The value of the largest jump, out of the four edges within a cell, is used as the indicator for that cell. Based on this indicator, the 20% of cells with the largest jump are refined. Future work will explore simply using ϵ to indicate refinement, rather than the jump error. The refinement of a cell is chosen to be symmetric, with each space-angle cell divided into four equal-sized cells. The solution for $\tilde{I}^{n+1}(x, \mu)$ of the batch is projected onto the finer mesh for the next batch. Because the dimensionality of the sample space has increased, we increase the number of histories per batch s.t. the ratio of the number of histories to total cells is approximately constant for all meshes. At the end of the last HO solve in a time step, \tilde{I}^{n+1} is projected back onto the original, coarsest mesh and stored as \tilde{I}^n for the next time step.

4.4.1 Continuous Weight Deposition Tallies

As in [?], because we are solving a pure absorber problem with Monte Carlo, we will allow particles to stream without absorption to reduce statistical variance in the tallies. The weight of particles is reduced deterministically along the path as they stream, with no need to sample a path length. Because particles are exponentially attenuated, the normalized weight is adjusted as $w(x, \mu) = w(x_0, \mu) \exp(-\sigma_t |(x - x_0)/\mu|)$, where x_0 is the starting location of the path. The tallies account for the

continuously changing weight, as given in Appendix 7.3. Histories are allowed to stream in this manner for 6 mean free paths (mfp) before switching to analog path length sampling; this limits the tracking of very small weight histories. The choice of 6 mfp allows particles to continuously deposit weight until they reach 0.25% of their original weight. Path lengths are tracked in terms of mfp, so there is no need to resample at material interfaces.

4.4.2 *Modified Systematic Sampling Algorithm*

As another way to improve efficiency, a modified systematic sampling method [4] was used for determining source particle locations. The goal is to effectively distribute particle histories to regions of importance, but to sample a sufficient number of histories in less probable regions to prevent large statistical noise. However, there is no need to sample histories in regions in thermal equilibrium. The residual gives a good indication of where histories are most likely to contribute to the error, particularly in optically thick cells where particles do not transport long distances. In the sampling algorithm the number of particle histories sampled in each space-angle cell is predetermined and proportional to the magnitude of the residual, including face and volumetric sources, within that cell. Then, for the predetermined number of histories within a cell, the source location is randomly sampled according to the residual source distribution of that cell. In cells where the relative magnitude of the residual is on the order of roundoff no particle histories are sampled. In these regions the problem is remaining in equilibrium and the solution is known exactly. For cells that are significant, but have a predetermined number of histories below some preset minimum N_{min} , the number of histories sampled in that cell is set to N_{min} . This is to limit bad statistics in low probability cells (this would be important for adaptively refined meshes). In the simulations performed for this work $N_{min} = 1$. This choice

was made to keep the total number of histories per time step constant throughout the simulation for comparison to IMC.

5. THE MOMENT-BASED LOW-ORDER EQUATIONS

The formulation of the LO equations is similar to a discontinuous FE method. Weighted integrals of the the equations are taken with functions that have local support as weight functions. The equations are written with element-wise moments of I and T as unknowns. Leaving the solution in this form allows for use of information from a previous HO solution to eliminate auxillary unknowns from the equations. This is different than a standard Galerkin FE method [?] where a functional form of the solution is directly assumed. The final equations will have a similar form to S_2 equations, but we have not used a collocation method in angle, which should limit ray effects [?] in higher spatial dimensions. The equations eliminate extra spatial unknowns in a manner similar to to a linear-discontinuous FE method [?]. We also explore the possibility of using the MC solution to modify the discretization of the LO solution in Sec. 8.6. MOVE

The remainder of this chapter is structured as follows: the general moments will be derived and then the angular and spatial closure are discussed REWRITE. For simplicity, the backward Euler time discretization is used throughout this section. Sec. ?? will use the HO solution and MC transport to consistently close the equations in time, improving time accuracy.

5.1 Forming the Space-Angle Moment Equations

5.1.1 *LO Spatial mesh and Finite-Element Spatial Moments*

The LO equations are formulated over a FE mesh. The domain for the i -th spatial element (or cell) has support $x \in [x_{i-1/2}, x_{i+1/2}]$ with width $h_i = x_{i+1/2} - x_{i-1/2}$ and cell center $x_i = x_{i-1/2} + h_i/2$. There is a total of N_c elements, spanning the spatial domain $0 \leq x \leq X$. For simplicity, this spatial mesh is fixed throughout the

simulation. Mesh adaptation is only applied in the HO solver.

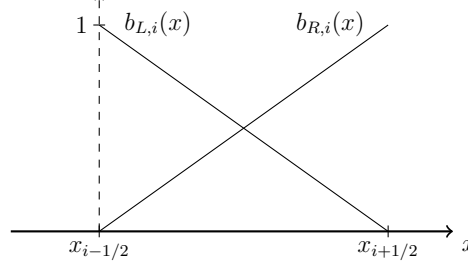


Figure 5.1: Illustration of linear finite element basis functions $b_{L,i}(x)$ and $b_{R,i}(x)$ for spatial element i .

The spatial moments are defined by integrals weighted with the standard linear finite element (FE) interpolatory basis functions. An illustration of the two linear FE basis functions for the i -th element is given in Fig. 5.1. The left basis function is defined as

$$b_{L,i}(x) = \begin{cases} \frac{x_{i+1/2}-x}{h_i} & x_{i-1/2} \leq x \leq x_{i+1/2} \\ 0 & \text{elsewhere} \end{cases}, \quad (5.1)$$

corresponding to the node $x_{i-1/2}$. The right basis function is

$$b_{R,i}(x) = \begin{cases} \frac{x-x_{i-1/2}}{h_i} & x_{i-1/2} \leq x \leq x_{i+1/2} \\ 0 & \text{elsewhere} \end{cases}, \quad (5.2)$$

corresponding to the node $x_{i+1/2}$. With these definitions, a local linear approximation to a function f can be formulated as $f(x) \simeq f_{L,i}b_{L,i}(x) + f_{R,i}b_{R,i}(x)$, $x \in [x_{i-1/2}, x_{i+1/2}]$.¹

¹In literature the FE functions are formally defined with support over two adjacent elements. However, in our notation our functions only have non-zero support in element i . This accommodates our later definition of moments and discontinuous unknowns.

The spatial moments are defined by integrals over the each element, using the two basis functions. We use $\langle \cdot \rangle$ to indicate integration over a spatial element. The spatial moments are

$$\langle \cdot \rangle_{L,i} = \frac{2}{h_i} \int_{x_{i-1/2}}^{x_{i+1/2}} b_{L,i}(x)(\cdot)dx \quad (5.3)$$

and

$$\langle \cdot \rangle_{R,i} = \frac{2}{h_i} \int_{x_{i-1/2}}^{x_{i+1/2}} b_{R,i}(x)(\cdot)dx. \quad (5.4)$$

where the factor of $2/h_i$ is a normalization constant. It is noted in this notation $\langle \phi \rangle_{L,i}$ and $\langle \phi \rangle_{R,i}$ represent spatial moments of the intensity over cell i , opposed to $\phi_{L,i}$ and $\phi_{R,i}$, which represent the interior value of the linear representation of $\phi(x)$ at $x_{i-1/2}$ and $x_{i+1/2}$ within the cell.

To simplify notation and discussion, we also define the slope and average moments over a spatial cell. The average scalar intensity is

$$\phi_i = \frac{1}{h_i} \int_{x_{i-1/2}}^{x_{i+1/2}} \phi(x)dx \quad (5.5)$$

and

$$\phi_{x,i} = \frac{6}{h_i} \int_{x_{i-1/2}}^{x_{i+1/2}} \left(\frac{x - x_i}{h_i} \right) \phi(x)dx. \quad (5.6)$$

The linear representation over a cell in terms of these moments is $\phi(x) = \phi_i + 2\phi_{x,i}(x - x_i)/h_i^2$, for $x \in (x_{i-1/2}, x_{i+1/2})$.

5.1.2 Definition of Angular Moments

To reduce the angular dimensionality, positive and negative half-range integrals of the angular intensity are taken. The angular integrals are denoted with a superscript as

$$(\cdot)^\pm = \pm \int_0^{\pm 1} (\cdot) d\mu \quad (5.7)$$

The half-range integrals of I are defined as $\phi^+(x, t) = \int_0^1 I(x, \mu, t) d\mu$ and $\phi^-(x, t) = 2\pi \int_{-1}^0 I(x, \mu, t) d\mu$, respectively. Thus, in terms of half-range quantities, the mean intensity is $\phi = \phi^- + \phi^+$. It is noted that in this notation the flux is defined as $J = J^- + J^+$, which is not the standard definition for the half-range fluxes, e.g., in [2].

5.1.3 Space-Angle Moments of the Radiation Transport Equation

The LO radiation equations are formed by applying the space and angle moment operators to the transport equation and performing algebraic manipulation. We provide a detailed derivation of the L and $+$ radiation moment equation and state the final results for the other moment operators. First, the L moment operator is applied to the time-discretized transport equation, i.e., Eq. (2.1). Integration by parts on the streaming term yields

$$\begin{aligned} -\frac{2}{h_i} \mu_{i-1/2} I_{i-1/2}^{n+1} + \frac{2}{h_i^2} \int_{x_{i-1/2}}^{x_{i+1/2}} \mu I^{n+1} dx + \left(\sigma_{t,i}^{n+1} + \frac{1}{c\Delta t} \right) \langle \phi \rangle_{L,i}^{n+1,+} \\ - \frac{\sigma_{s,i}}{2} \langle \phi \rangle_{L,i}^{n+1} = \frac{1}{2} \langle \sigma_a^{n+1} a c T^{n+1,4} \rangle_{L,i} + \frac{1}{c\Delta t} \langle \phi \rangle_{L,i}^{n,+}. \end{aligned} \quad (5.8)$$

Here, the cross sections have been assumed constant over a cell. The mean intensity in the scattering term is expanded in terms of half-range unknowns. The integral can be rewritten in terms of L and R moments by noting that $b_{L,i}(x) + b_{R,i}(x) = 2/h_i$. These substitutions are made and the resulting equation is multiplied by h_i to produce

$$\begin{aligned} -2\mu_{i-1/2} I_{i-1/2}^{n+1} + \langle \mu I^{n+1} \rangle_{L,i} + \langle \mu I^{n+1} \rangle_{R,i} + \left(\sigma_{t,i}^{n+1} + \frac{1}{c\Delta t} \right) h_i \langle \phi \rangle_{L,i}^{n+1,+} \\ - \frac{\sigma_{s,i} h_i}{2} (\langle \phi \rangle_{L,i}^{n+1,+} + \langle \phi \rangle_{L,i}^{n+1,-}) = \frac{h_i}{2} \langle \sigma_a^{n+1} a c T^{n+1,4} \rangle_{L,i} + \frac{h_i}{c\Delta t} \langle \phi \rangle_{L,i}^{n,+}. \end{aligned} \quad (5.9)$$

The resulting equation is integrated over the positive half range:

$$\begin{aligned}
& -2 \left(\mu_{i-1/2} I_{i-1/2}^{n+1} \right)^+ + \langle \mu I^{n+1} \rangle_{L,i}^+ + \langle \mu I^{n+1} \rangle_{R,i}^+ + \left(\sigma_{t,i}^{n+1} + \frac{1}{c\Delta t} \right) h_i \langle \phi \rangle_{L,i}^{n+1,+} \\
& - \frac{\sigma_{s,i} h_i}{2} \left(\langle \phi \rangle_{L,i}^{n+1,+} + \langle \phi \rangle_{L,i}^{n+1,-} \right) = \frac{h_i}{2} \langle \sigma_a^{n+1} a c T^{n+1,4} \rangle_{L,i} + \frac{h_i}{c\Delta t} \langle \phi \rangle_{L,i}^{n,+}. \quad (5.10)
\end{aligned}$$

5.1.4 The Angular Consistency Terms

Now, algebraic manipulations are performed on the streaming terms to produce face and volume-averaged values of μ , weighted by the intensity. Each term in the streaming term is multiplied by a factor of unity, with the desired unknown appropriate to each term in the numerator and denominator. Temporarily dropping the time index for clarity, the manipulations applied to the streaming term are as follows:

$$\left\langle \mu \frac{\partial I}{\partial x} \right\rangle_L^+ = -\frac{2}{h_i} (\mu I_{i-1/2})^+ + \frac{1}{h_i} [\langle \mu I \rangle_{L,i}^+ + \langle \mu I \rangle_{R,i}^+] \quad (5.11)$$

$$= -\frac{2}{h_i} (\mu I_{i-1/2})^+ \frac{(I_{i-1/2})^+}{(I_{i-1/2})^+} + \frac{1}{h_i} \left[\langle \mu I \rangle_{L,i}^+ \frac{\langle I \rangle_{L,i}^+}{\langle I \rangle_{L,i}^+} + \langle \mu I \rangle_{R,i}^+ \frac{\langle I \rangle_{R,i}^+}{\langle I \rangle_{R,i}^+} \right] \quad (5.12)$$

$$= -\frac{2}{h_i} \left\{ \frac{(\mu I)_{i-1/2}^+}{\phi_{i-1/2}^+} \right\} \phi_{i-1/2}^+ + \frac{1}{h_i} \left[\left\{ \frac{\langle \mu I \rangle_{L,i}^+}{\langle \phi \rangle_{L,i}^+} \right\} \langle \phi \rangle_{L,i}^+ + \left\{ \frac{\langle \mu I \rangle_{R,i}^+}{\langle \phi \rangle_{R,i}^+} \right\} \langle \phi \rangle_{R,i}^+ \right] \quad (5.13)$$

The ratios in braces are what we will formally define as *angular consistency terms*. These nonlinear functionals are approximated by the HO solver. The angular consistency term for the L and $+$ moments is defined as

$$\{\mu\}_{L,i}^{n+1,+} \equiv \frac{\langle \mu I^{n+1} \rangle_{L,i}^+}{\langle I^{n+1} \rangle_{L,i}^+} = \frac{\frac{2}{h_i} \int_0^1 \int_{x_{i-1/2}}^{x_{i+1/2}} \mu b_{L,i}(x) I^{n+1}(x, \mu) dx d\mu}{\frac{2}{h_i} \int_0^1 \int_{x_{i-1/2}}^{x_{i+1/2}} b_{L,i}(x) I^{n+1}(x, \mu) dx d\mu}. \quad (5.14)$$

The consistency terms on the face represent averaging at a point, with a similar definition as

$$\mu_{i+1/2}^+ \equiv \frac{(\mu I_{i+1/2})^+}{\phi_{i+1/2}^+} = \frac{\int_0^1 \mu I(x_{i+1/2}, \mu) d\mu}{\int_0^1 I(x_{i+1/2}, \mu) d\mu}. \quad (5.15)$$

There are analogous definitions for the R and $-$ moments. The moment of the streaming term for the L and $+$ operators becomes

$$\left\langle \mu \frac{\partial I}{\partial x} \right\rangle_L^+ = -\frac{2}{h_i} \mu_{i-1/2}^+ I_{i-1/2}^+ + \frac{1}{h_i} \left[\{\mu\}_{L,i}^+ \langle \phi \rangle_{L,i}^+ + \{\mu\}_{R,i}^+ \langle \phi \rangle_{R,i}^+ \right] \quad (5.16)$$

It is noted that this expression does not contain a cross section in the denominator, such as in the variable Eddington factor approach [?], thus this method will be stable in a void.

5.1.5 The Exact Radiation Moment Equations

A final expression for the moment equation resulting from application of the L moment and positive half-range integral is obtained by substituting the result of Eq. (5.16) into Eq. (5.10):

$$\begin{aligned} & -2\mu_{i-1/2}^{n+1,+} \phi_{i-1/2}^{n+1,+} + \{\mu\}_{L,i}^{n+1,+} \langle \phi \rangle_{L,i}^{n+1,+} + \{\mu\}_{R,i}^{n+1,+} \langle \phi \rangle_{R,i}^{n+1,+} + \left(\sigma_{t,i}^{n+1} + \frac{1}{c\Delta t} \right) h_i \langle \phi \rangle_{L,i}^{n+1,+} \\ & - \frac{\sigma_{s,i} h_i}{2} (\langle \phi \rangle_{L,i}^{n+1,+} + \langle \phi \rangle_{L,i}^{n+1,-}) = \frac{h_i}{2} \langle \sigma_a^{n+1} a c T^{n+1,4} \rangle_{L,i} + \frac{h_i}{c\Delta t} \langle \phi \rangle_{L,i}^{n,+}, \quad (5.17) \end{aligned}$$

Similar derivations can be used to derive the other radiation moment equations. Pairwise application of the L and R basis moments with the $+$ and $-$ half-range integrals to Eq. (??) ultimately yields four moment equations per cell. The equation

for the R and $+$ moment is

$$2\mu_{i+1/2}^{n+1,+} \phi_{i+1/2}^{n+1,+} - \{\mu\}_{L,i}^{n+1,+} \langle \phi \rangle_{L,i}^{n+1,+} - \{\mu\}_{R,i}^{n+1,+} \langle \phi \rangle_{R,i}^{n+1,+} + \left(\sigma_{t,i}^{n+1} + \frac{1}{c\Delta t} \right) h_i \langle \phi \rangle_{R,i}^{n+1,+} - \frac{\sigma_{s,i} h_i}{2} (\langle \phi \rangle_{R,i}^{n+1,+} + \langle \phi \rangle_{R,i}^{n+1,-}) = \frac{h_i}{2} \langle \sigma_a^{n+1} acT^{n+1,4} \rangle_{R,i} + \frac{h_i}{c\Delta t} \langle \phi \rangle_{R,i}^{n,+}, \quad (5.18)$$

The equations for the negative half-range moment are identical to the above with the negative half-range superscripts replacing the positive. Explicitly,

$$-2\mu_{i-1/2}^{n+1,-} \phi_{i-1/2}^{n+1,-} + \{\mu\}_{L,i}^{n+1,-} \langle \phi \rangle_{L,i}^{n+1,-} + \{\mu\}_{R,i}^{n+1,-} \langle \phi \rangle_{R,i}^{n+1,-} + \left(\sigma_{t,i}^{n+1} + \frac{1}{c\Delta t} \right) h_i \langle \phi \rangle_{L,i}^{n+1,-} - \frac{\sigma_{s,i} h_i}{2} (\langle \phi \rangle_{L,i}^{n+1,+} + \langle \phi \rangle_{L,i}^{n+1,-}) = \frac{h_i}{2} \langle \sigma_a^{n+1} acT^{n+1,4} \rangle_{L,i} + \frac{h_i}{c\Delta t} \langle \phi \rangle_{L,i}^{n,-} \quad (5.19)$$

and

$$2\mu_{i+1/2}^{n+1,-} \phi_{i+1/2}^{n+1,-} - \{\mu\}_{L,i}^{n+1,-} \langle \phi \rangle_{L,i}^{n+1,-} - \{\mu\}_{R,i}^{n+1,-} \langle \phi \rangle_{R,i}^{n+1,-} + \left(\sigma_{t,i}^{n+1} + \frac{1}{c\Delta t} \right) h_i \langle \phi \rangle_{R,i}^{n+1,-} - \frac{\sigma_{s,i} h_i}{2} (\langle \phi \rangle_{R,i}^{n+1,+} + \langle \phi \rangle_{R,i}^{n+1,-}) = \frac{h_i}{2} \langle \sigma_a^{n+1} acT^{n+1,4} \rangle_{R,i} + \frac{h_i}{c\Delta t} \langle \phi \rangle_{R,i}^{n,-}, \quad (5.20)$$

Ultimately, the two half-ranges will be treated differently when the equations are closed spatially.

5.1.6 Material Energy Equations

To derive the LO material energy equations, an approximation must be introduced to relate $T(x)$ and $T^4(x)$ within a cell. We represent $T(x)$ spatially with a LDFF trial space. This trial space will ensure preservation of the equilibrium diffusion limit. To simplify the relation between $T(x)$ and $T^4(x)$ $T(x) \simeq T_{L,i} b_{L,i}(x) + T_{R,i} b_{R,i}(x)$, $x \in (x_{i-1/2}, x_{i+1/2})$. Similarly, the emission term is represented in the material and radiation equations with the LDFF interpolant $T^4(x) \simeq T_{L,i}^4 b_{L,i}(x) +$

$T_{R,i}^4 b_{R,i}(x)$. The L and R spatial moments are taken of the material energy equations; the LD FE representations for $T(x)$ and $\sigma_a a c T^4(x)$ are used to simplify the spatial integrals. The final LO material energy equation resulting from application of the L moment is

$$\begin{aligned} \frac{\rho_i c_{v,i}}{\Delta t} \left[\left(\frac{2}{3} T_{L,i} + \frac{1}{3} T_{R,i} \right)^{n+1} - \left(\frac{2}{3} T_{L,i} + \frac{1}{3} T_{R,i} \right)^n \right] + \sigma_{a,i}^{n+1} (\langle \phi \rangle_{L,i}^+ + \langle \phi \rangle_{L,i}^-)^{n+1} \\ = \sigma_{a,i}^{n+1} a c \left(\frac{2}{3} T_{L,i}^4 + \frac{1}{3} T_{R,i}^4 \right)^{n+1}. \end{aligned} \quad (5.21)$$

The equation for the R moment is

$$\begin{aligned} \frac{\rho_i c_{v,i}}{\Delta t} \left[\left(\frac{1}{3} T_{L,i} + \frac{2}{3} T_{R,i} \right)^{n+1} - \left(\frac{1}{3} T_{L,i} + \frac{2}{3} T_{R,i} \right)^n \right] + \sigma_{a,i}^{n+1} (\langle \phi \rangle_{R,i}^+ + \langle \phi \rangle_{R,i}^-)^{n+1} \\ = \sigma_{a,i}^{n+1} a c \left(\frac{1}{3} T_{L,i}^4 + \frac{2}{3} T_{R,i}^4 \right)^{n+1}. \end{aligned} \quad (5.22)$$

Cross sections have been assumed constant over each element, evaluated at the average temperature within the element, i.e., $\sigma_{a,i}^{n+1} = \sigma_{a,i}([T_{L,i}^{n+1} + T_{R,i}^{n+1}]/2)$. Because the material energy balance only contains angularly integrated quantities, there is no need to take angular moments of the above equations.

REWRITE: WHAT TO DO WITH THIS PARAGRAPH? Because there are no derivatives of T in Eq. (??), there is no need to define T on the faces. Because only moments of ϕ appear in the material energy equations, they are fully defined at this point. The LD closure for the L and $+$ equations produces

5.2 Closing the LO System with Information from the HO Solution

The six degrees of freedom (DOF) over each cell i are the four moments $\langle \phi \rangle_{L,i}^+$, $\langle \phi \rangle_{R,i}^+$, $\langle \phi \rangle_{L,i}^-$, and $\langle \phi \rangle_{R,i}^-$ and the two spatial edge values $T_{L,i}$ and $T_{R,i}$. The four

radiation and two material energy equations define a system of equations for the six DOF, coupled spatially through the streaming term. We emphasize that at this point we have not made any spatial or angular approximations to the transport moment equations; these moment equations are exact with respect to the chosen time discretization. The material energy equation has the approximation of an LDFE space for $T(x)$. Some approximation of this form is necessary to relate T and T^4 .

5.2.1 Angular Closure

The angular consistency parameters (e.g., Eq. (5.14) and (5.15)) are not known a priori. A lagged estimate of I^{n+1} from the previous HO solve is used to estimate the angular consistency parameters. In the HOLO algorithm, the equations for LO unknowns at iteration $k + 1$ use consistency parameters computed using the latest HO solution $\tilde{I}^{n+1,k+1/2}$ as an approximation for $I^{n+1}(x, \mu)$. We evaluate these terms using quadrature based on the functional form of the solution provided by the HO solution.

5.2.2 Spatial Closure

The relation between the volume and face averaged quantities must be known to eliminate the final auxillary unknowns. To close the LO system spatially, we will explore multiple options. The simplest closure is to use a linear-discontinuous (LD) spatial closure with the usual upwinding approximation [?]. For example, for positive flow (e.g., Eq. (??)) the face terms $\mu_{i-1/2}$ and $\phi_{i-1/2}$ are upwinded from the previous cell $i - 1$ or from a boundary condition; the terms at $x_{i+1/2}$ are linearly extrapolated, computed using the L and R basis moments. By assuming $\phi^\pm(x)$ is linear over a cell, a relation between the outflow and moments can be derived, e.g., $\phi_{i+1/2}^+ = 2\langle\phi\rangle_R^+ - \langle\phi\rangle_L^+$. For the negative half range, $\phi_{i-1/2}^- = 2\langle\phi\rangle_L^- - \langle\phi_R\rangle^+$. The LD

closure, with upwinding, for the L equation and positive half-range is

$$-2\mu_{i-1/2}^{n+1,+} (2\langle\phi\rangle_{R,i-1}^+ -) + \{\mu\}_{L,i}^{n+1,+} \langle\phi\rangle_{L,i}^{n+1,+} + \{\mu\}_{R,i}^{n+1,+} \langle\phi\rangle_{R,i}^{n+1,+} + \left(\sigma_{t,i}^{n+1} + \frac{1}{c\Delta t}\right) h_i \langle\phi\rangle_{L,i}^{n+1,+} - \frac{\sigma_{s,i} h_i}{2} (\langle\phi\rangle) \quad (5.23)$$

Similar equations can be derived for the other directions, fully defining the radiation equations. These equations are equivalent to an S_2

Note that we have chosen to leave $\mu_{i-1/2}^{n+1,+}$ as a value to be estimated from the HO solver, which is more conducive to the other spatial closures described in Sec. ???. Alternatively, the spatial closure could be introduced before performing the algebraic manipulation to form consistency terms (e.g., into Eq. (5.11)). This would produce only volume-weighted consistency terms for the LD spatial closure.

5.2.2.1 Fixups to LD Solution

The linear-discontinuous (LD) closure with upwinding is not strictly positive. In particular, for optically thick cells with a steep intensity gradient, the solution becomes negative. These negative values of intensity can propagate to adjacent cells. In thick regions of TRT problems, reasonably fine spatial cells can still be on the order of millions of mean free paths; negative values with an LD representation are unavoidable in practice for such cells and mesh refinement is of minimal use. Typically, for a standard LDFE method, the equations are lumped to produce a strictly positive solution (for 1D) [?]. However, standard FE lumping procedures would introduce difficulties in computing the consistency terms from the HO solution. Thus, an alternative spatial closure is used that is equivalent to the standard FE lumping procedure. The L and R moments are defined the same as before, preserving the average within a cell, but the relation between the moments and the outflow is modified. For example, for positive μ , the outflow is now defined as $\phi_{i+1/2}^+ = \langle\phi\rangle_R^+$.

Because the basis function $b_{R,i}(x)$ is strictly positive, the outflow is positive. This closure is only used in cells where negative intensities occur.

5.2.3 *Newton's Method for LO Equations*

Adding the equations for each cell together forms a global system of coupled equations. The equations are nonlinear due to the Planckian emission source. We have used Newton's method to solve the nonlinear system, based on a typical linearization of the Planckian source with cross sections evaluated at temperatures from the previous iteration, as described in [?]. A derivation of the LO Newton equations is given in ??.

The equations for each half-range are coupled together via scattering. In one spatial dimension, the scattering terms can be included in the discrete system matrix and directly inverted. We consider an alternative iterative solution method that could be more easily extended to higher spatial dimensions in Sec. ??. Isotropic scattering, including effective scattering terms from the linearization, are included in the system matrix. The system matrix is an asymmetric, banded matrix with a band width of seven and is inverted directly. Newton iterations are repeated until $\phi^{n+1}(x)$ and $T^{n+1}(x)$ are converged to a desired relative tolerance. Convergence is calculated using the spatial L_2 norm of the change in $\phi^{n+1}(x)$ and $T^{n+1}(x)$, relative to the norm of each solution. The lumping-equivalent discretization discussed above is used for cells where the solution for ϕ^{n+1} becomes negative. When negative values for $\phi^{n+1,\pm}(x)$ are detected, the lumping-equivalent discretization is used within those cells and that Newton step is repeated.

6. ACCELERATED ITERATIVE SOLUTION TO THE LO EQUATIONS

As described in Sec. ??, the fully-discrete, S_2 -like LO equations are not easy to directly inverted efficiently in higher spatial dimensions. To demonstrate a possible path forward in higher dimensions, we have investigated the use of a standard source iteration scheme to invert the scattering terms in the LO equations. As material properties become more diffusive (e.g., c_v is small and σ_a is large), the effective scattering cross sections becomes large. This results in a spectral radius of the source iterations that approaches unity [?]. These regimes are typical in TRT simulations, so an acceleration method for an iterative solution is critical. We have accelerated the source iterations with a nearly-consistent diffusion synthetic acceleration (DSA) method known as WLA [?, 6].

REWRITE: STUFF ABOUT LUMPING ETC. We have also recast the DSA method as a preconditioner to an iterative Krylov solution [?] of the LO equations. Generally, Krylov methods mitigate acceleration losses due to inconsistencies in the acceleration method. In higher dimensions, the use of a Krylov method is necessary for effective acceleration for nearly-consistent acceleration methods in problems with mixed optical thicknesses [?], e.g., typical radiative transfer problems. Also, applying the preconditioned-Krylov approach allows for the use of spatially lumped DSA equations as a preconditioner, with the LO equations using alternative fix-up methods. We expect better acceleration performance (DID WE GET IT?) when the LDD discretization is introduced into the LO equations.

In the remainder of this chapter is structured as follows: The source iteration solution to the LO equations is detailed. Then, the equations for the WLA DSA method are derived and the acceleration algorithm is given. The DSA method is

then recast as a preconditioner to a GMRES solution to the scattering iteration equations. Finally, results are given for a modified test problem which requires the use of acceleration.

6.1 Source Iteration Solution to the Linearized LO Equations

The linearized LO equations can be solved with a source iteration method [2, ?, ?]. In the source iteration process the scattering source is lagged, which uncouples unknowns between the two half-ranges. This produces a lower-triangular system where the spatial unknowns can be solved for sequentially along the two directions of flow via a standard sweeping procedure [2, ?]. Beginning at the left boundary, the positive unknowns can be determined for each cell from $i = 1, \dots, N_c$; because the inflow to the i -th cell is defined from the previous cell or boundary condition, a local system of equations can be solved for the $\langle \phi \rangle_{L,i}^+$ and $\langle \phi \rangle_{R,i}^+$ unknowns. The negative direction unknowns are determined similarly, starting from the right boundary towards the left. The newly computed half-range intensities can then be used to estimate the scattering source for the next iteration. This process is repeated until convergence.

The source iteration process can be written in operator notation as

$$\mathbf{M}\underline{\psi}^{l+1} = \frac{1}{2}\mathbf{S}\underline{\psi}^l + \underline{Q}, \quad (6.1)$$

where \mathbf{M} is the LO streaming and removal operator (i.e., the left-hand side of Eqs. (5.17)–(5.20) without the scattering terms included), $\underline{\psi}$ is a vector of the half-range FE moment unknowns, and the vector \underline{Q} contains the fixed source terms resulting from the linearized emission source and previous time step moments, for each equation. The source terms for the i -th element and the L equation, for both

half-ranges, are

$$(\underline{Q})_{i,L}^{\pm} = \frac{\langle \phi \rangle_L^{\pm}}{c\Delta t} + \frac{1}{2}f_i\sigma_{a,i}ac\langle (T^n)^4 \rangle_{L,i} \quad (6.2)$$

The scattering operator terms for the i -th element and the L equations are

$$(\underline{\mathbf{S}}\underline{\psi}^l)_{i,L}^{\pm} = (\sigma_{a,i}(1 - f_i) + \sigma_{s,i}) (\langle \phi^l \rangle_{i,L}^+ + \langle \phi^l \rangle_{i,L}^-). \quad (6.3)$$

Equivalent expressions are defined for the R moment equations and boundary conditions, forming a fully defined set of equations. The process of sweeping is denoted as \mathbf{M}^{-1} .

The scattering inversion must be performed within each Newton iteration. Thus, for the m -th Newton step, the source iteration process is defined as

1. Evaluate effective scattering and absorption cross sections with $\{T_i^m : i = 1, 2, \dots, N_c\}$.
2. Compute new scattering source $\frac{1}{2}\underline{\mathbf{S}}\underline{\psi}^l$.
3. Perform sweeps to calculate $\underline{\psi}^{l+1} = \mathbf{M}^{-1}\underline{\mathbf{S}}\underline{\psi}^l + \mathbf{M}^{-1}\underline{Q}$
4. If $\|\underline{\psi}^{l+1} - \underline{\psi}^l\|_2 < \text{tolerance } \|\underline{\psi}^{l+1}\|$, move to next Newton step.
5. Else: repeat steps 2–4.

6.2 Linear Diffusion Synthetic Acceleration

A form of DSA referred to as the WLA method is used to accelerate the source iterations [?, 6]. Between each sweep, an error equation for the scattering iterations is solved with an approximate angular discretization of the transport equation. The estimated error is used to correct the zeroth moment of the intensity unknowns. In operator notation, the DSA equations for a single iteration are

$$\mathbf{L}\psi^{l+1/2} = \frac{1}{2}\mathbf{S}\psi^l + Q \quad (6.4)$$

$$\mathbf{D}\delta\phi^{l+1/2} = \mathbf{S}(\psi^{l+1/2} - \psi^l) \quad (6.5)$$

$$\psi^{l+1} = \psi^{l+1/2} + \delta\phi^{l+1/2}, \quad (6.6)$$

where $\delta\phi$ represents the error in the mean intensity unknowns. The operator \mathbf{D} represents a diffusion-like approximation to the transport equation. The DSA equations contain a standard finite-difference diffusion discretization that can be more efficiently inverted than the S_2 -like equations that are being accelerated (particularly in higher spatial dimensions), but will accurately resolve the slowly-converging, diffusive error modes.

It is important for the spatial discretization of Eq. (8.5) to be closely related to the discretization of the LO equations for the acceleration to be effective and stable [?]. The WLA method first solves a spatially-continuous discretization of the diffusion equation for the error at faces $\{x_{i+1/2}\}$. The error on the faces is then mapped onto the volumetric moment unknowns via a LD discretization of the P_1 equations [?]. The LD mapping resolves issues that would occur in optically-thick cells, while the continuous diffusion equation is accurate in the EDL where acceleration is important [?].

The continuous diffusion equation and mapping equations for the WLA method are derived in Appendix ???. To allow for the use of lumped or standard LD in the DSA equations, we introduce the factor θ , with $\theta = 1/3$ for standard LD, and $\theta = 1$ for lumped LD. The diffusion equation for the face at $x_{i+1/2}$ is

$$\begin{aligned} & \left(\frac{\sigma_{a,i+1}h_{i+1}}{4} (1 - \theta) - \frac{D_{i+1}}{h_{i+1}} \right) \delta\phi_{i+3/2} + \left(\frac{D_{i+1}}{h_{i+1}} + \frac{D_i}{h_i} + \left(\frac{1 + \theta}{2} \right) \left[\frac{\sigma_{a,i+1}h_{i+1}}{2} + \frac{\sigma_{a,i}h_i}{2} \right] \right) \delta\phi_{i+1/2} \\ & + \left(\frac{\sigma_{a,i}h_i}{4} (1 - \theta) - \frac{D_i}{h_i} \right) \delta\phi_{i-1/2} = \frac{h_{i+1}}{2} \langle q \rangle_{L,i+1} + \frac{h_i}{2} \langle q \rangle_{R,i} . \quad (6.7) \end{aligned}$$

The source in Eq. (8.7) is the residual for a given scattering iteration [?, 2]

$$\langle q \rangle_{L/R,i} = \sigma_{s,i} (\langle \phi^{l+1/2} \rangle_{L/R,i} - \langle \phi^l \rangle_{L/R,i}). \quad (6.8)$$

It is noted that there is no need to define the source differently for the lumped or standard LD DSA equations because it is in terms of moments.

The upwinding in the LO system exactly satisfies the inflow boundary conditions, therefore a vacuum boundary condition is applied to the diffusion error equations. Application of Eq. (??) gives the left boundary condition:

$$\left(\frac{1}{2} + \sigma_{a,1} h_1 \frac{1+\theta}{4} - \frac{D_1}{h_1} \right) \delta \phi_{1/2} + \left(\sigma_{a,1} h_1 \frac{1-\theta}{4} - \frac{D_1}{h_1} \right) \delta \phi_{3/2} = \frac{h_1}{2} \langle q \rangle_{L,1} \quad (6.9)$$

The boundary condition for the right-most face is

$$\left(\frac{1}{2} + \sigma_{a,I} h_I \frac{1+\theta}{4} - \frac{D_I}{h_I} \right) \delta \phi_{I+1/2} + \left(\sigma_{a,I} h_I \frac{1-\theta}{4} - \frac{D_I}{h_I} \right) \delta \phi_{I-1/2} = \frac{h_I}{2} \langle q \rangle_{R,I} \quad (6.10)$$

where I is the index of the last cell.

The system of equations formed from Eqs. (8.9), (8.10), and (8.7) can be solved directly with a banded matrix solver. Then, Eq. (??)–(??) are solved in each cell to map the face errors onto an LD representation over the interior. It is noted that unlike fully consistent DSA equations, the WLA-DSA algorithm does not preserve particle balance to round off. This is because the mapping procedure uses an approximate inflow to each cell, which is inconsistent with the partial outflows from adjacent cells.

Because we are interested in the time-dependent solution, we need to accelerate the solution for the half-range intensities, rather than just the zeroth moment. We do not accelerate the first moment of the angular intensity, as the solution for ΔJ is inaccurate due to the approximations introduced. The error in the half-range

moments, using the lumping notation, are

$$\langle \delta \phi \rangle_L^\pm = \frac{1+\theta}{4} \delta \phi_L^\pm + \frac{1-\theta}{4} \delta \phi_R^\pm \quad (6.11)$$

$$\langle \delta \phi \rangle_R^\pm = \frac{1-\theta}{4} \delta \phi_L^\pm + \frac{1+\theta}{4} \delta \phi_R^\pm, \quad (6.12)$$

6.2.1 The WLA-DSA Accelerated Source Iteration Algorithm

We define the process of solving the diffusion like equations and mapping the error unknowns back onto the moment equations as the operator \mathbf{D}^{-1} . The source iteration with linear DSA procedure, for the m -th Newton iteration, is then defined as

1. Evaluate effective scattering and absorption cross sections with $\{T_i^m : i = 1, 2, \dots, N_c\}$.
2. Compute new scattering source $\mathbf{S}\psi^l$.
3. Perform sweeps to calculate $\psi^{l+1/2} = \mathbf{M}^{-1}\mathbf{S}\psi^l + \mathbf{M}^{-1}Q$
4. Perform DSA iteration to solve $\phi^{l+1} = \mathbf{D}^{-1}\sigma_s(\phi^{l+1/2} - \phi^l)$
 - Solve continuous DSA equations, i.e., Eq. (8.7) and Eq. (??), for $\{\delta \phi_{i+1/2}^{l+1/2} : i = 0, 1, \dots, N_c\}$.
 - Map the continuous error onto the moment unknowns, via Eq. (??)–(??).
5. Add correction to the moment unknowns, e.g., $\phi_L^{\pm, l+1} = \phi_L^{\pm, l+1/2} + \delta \phi^{l+1/2}/2$.
6. If $\|\psi^{l+1} - \psi^l\| < \text{tolerance}$, exit
7. Else: repeat steps 4–9.

6.3 GMRES Solution to the LO Equations

The source iteration procedure can be recast as an iterative solution to a matrix equation. Using operator notation, we manipulate the moment equations to form a matrix equation:

$$(\mathbf{I} - \mathbf{M}^{-1}\mathbf{S}) \psi = \mathbf{M}^{-1}Q, \quad (6.13)$$

where I is an identity matrix. The GMRES method is used to iteratively solve the above linear system. The GMRES is an iterative Krylov solution method for asymmetric, sparse matrix equations [?]. Krylov solutions to a linear system repeatedly apply the matrix operator to vectors, projecting the system onto a Krylov subspace [?]. Rather than forming the full matrix system, we apply the operation of \mathbf{S} and \mathbf{M}^{-1} as detailed in Sec. (8.1) to apply $(\mathbf{I} - \mathbf{M}^{-1}\mathbf{S})$ to the Krylov vectors.

The GMRES method will generally converge faster than the source iteration procedure [?]. However, as the system becomes scattering dominated, convergence will degrade. To improve the convergence rate, we precondition the GMRES system with the WLA-DSA method. The goal of preconditioning is to efficiently apply an operator to the equation that will approximate the inverse of the matrix operator. Left preconditioning [?] was applied to the above system. In matrix form, we write the preconditioned GMRES equations as

$$(\mathbf{I} + \mathbf{D}^{-1}\mathbf{S}) (\mathbf{I} - \mathbf{L}^{-1}\mathbf{S}) \psi = (\mathbf{I} + \mathbf{D}^{-1}\mathbf{S}) \mathbf{L}^{-1}Q. \quad (6.14)$$

The operation of $(\mathbf{I} + \mathbf{D}^{-1}\mathbf{S})^{-1}$ is equivalent to the DSA procedure, adding the correction to a Krylov vector.

The opensource library `mgmres` was modified to implement the matrix-free version of the GMRES procedure. The infrastructure from the source iteration with DSA

procedure is reused to provide the operation of $(\mathbf{I} + \mathbf{D}^{-1}\mathbf{S})(\mathbf{I} - \mathbf{M}^{-1}\mathbf{S})$ applied to the Krylov vectors returned from the GMRES solver. The preconditioned-GMRES algorithm is

1. Evaluate effective scattering and absorption cross sections with $\{T_i^m : i = 1, 2, \dots, N_c\}$.
2. Form initial source vector b by solving $b = \mathbf{M}^{-1}Q$
3. Apply left-preconditioner operator to b , so $b \leftarrow (\mathbf{I} + \mathbf{D}^{-1}\mathbf{S})\mathbf{M}^{-1}Q$
4. Compute new scattering source $\mathbf{S}\psi^l$.
5. Perform sweeps to calculate $\psi^{l+1/2} = \mathbf{M}^{-1}\mathbf{S}\psi^l + \mathbf{M}^{-1}Q$
6. Compute DSA residual source $\sigma_s(\phi^{l+1/2} - \phi^l)$
7. Solve continuous DSA equations (i.e., Eq. (8.7)) for $\{\delta\phi_{i+1/2}^{l+1/2} : i = 0, 1, \dots, N_c\}$
8. Map the continuous error onto the moment unknowns.
9. If $\|\psi^{l+1} - \psi^l\| < \text{tolerance}$, exit
10. Else: repeat steps 4-9.

The convergence tolerance is based on the residual. Without preconditioning, the diffusion solve is simply removed.

6.4 Computational Results

It is noted we are not interested in measuring the reduction of computational time in this section because in 1D the LO equations can be directly solved efficiently. We are just interested in ensuring that the acceleration methods can reduce the number of scattering iterations sufficiently, including cases where inconsistencies in the LO equations are present.

We test our acceleration methods with three test problems. The first is the two material problem in Sec ???. The second problem is a modification of the two material problem described in Sec. ???. The problem specifications are the same as before, except for modifications to the material properties for $x > 0.5$ cm. In the right region, the parameters are $\sigma_a = 20,000 \text{ cm}^{-1}$, $\sigma_s = 500 \text{ cm}^{-1}$, $c_v = ??? \text{ Jk g}^{-1} \text{ keV}^{-1}$. The third test problem is the diffusion limit problem described in Sec. ???.

6.4.1 Results for LD Spatial Discretization

We first test this problem with the source iteration using DSA to accelerate and compare to an unaccelerated SI solution. 3 batches of 10,000 particles are ran for each HO solve, one HO solver per time step. We tally the total number of source iterations per time step, over the two solves. We initialize the solution for the scattering iterations to zero at the beginning of each LO solve. We reduce the solve time for each to 1.0 sh. The time step begins at 0.001 sh and linearly increases by 15 % each time step to a maximum time step size of 0.01 sh. The larger time step size increases the amount of diffusive behavior. The scattering iterations have a relative convergence between scattering iterations of 1.E-10.

For the DSA we have used a lumped spatial representation in all cases. This should cause some inconsistency issues, slightly degrading the acceleration. There is a slight degradation in the performance, but the GMRES does not work significantly better.

Table 6.1: Scattering source iterations for the two material problem. Simulation end time is 1 sh.

Method	Sweeps/Newton Step	Newton Steps/LO Solve
SI	247.0	19.4
SI-DSA	10.1	19.3
GMRES	13.1	19.4
GMRES-DSA	7.7	19.3

Table 6.2: Scattering source iterations for the equilibrium diffusion limit problem. Simulation end time is 3 sh.

LD LO Equations		
Method	Sweeps/Newton Step	Newton Steps/LO Solve
SI	357.4	4.2
SI-DSA	21.9	4.2
GMRES	36.5	4.2
GMRES-DSA	13.3	4.2
Lumped LO Equations		
SI	359.8	4.1
SI-DSA	14.6	4.1
GMRES	37.3	4.1
GMRES-DSA	9.8	4.1

7. THE HIGH-ORDER EXPONENTIALLY-CONVERGENT MONTE CARLO SOLVER

7.1 The ECMC High Order Solver

The transport equation to be solved by the HO solver is

$$\mu \frac{\partial I^{n+1,k+1/2}}{\partial x} + \left(\sigma_t^k + \frac{1}{c\Delta t} \right) I^{n+1,k+1/2} = \frac{\sigma_s}{2} \phi^{n+1,k} + \frac{1}{2} (\sigma_a^k a c T^4)^{n+1,k} + \frac{\tilde{I}^n}{c\Delta t} \quad (7.1)$$

where the superscript k represents the outer HOLO iteration index. Material property indices will be suppressed from now on. Here, $k + 1/2$ denotes the ECMC solution within outer HOLO iteration k , whereas k and $k + 1$ represent successive LO solves. The sources at k in Eq. (7.1) are estimated by the previous LO solution. Cross sections are evaluated at $T^{n+1,k}$. As all sources on the right side of the equation are known, this defines a fixed-source, pure absorber transport problem. We will solve this equation using ECMC. A more detailed description of the ECMC method can be found in [3], but a brief overview is given here. A general proof of exponential convergence for related adaptive MC transport methods with a different formulation is depicted in [?].

In operator notation, Eq. (7.1) can be written as

$$\mathbf{L}^k I^{n+1,k+1/2} = q^k \quad (7.2)$$

where $I^{n+1,k+1/2}$ is the transport solution of the angular intensity based on the k -th LO estimate of q^k . The linear operator \mathbf{L}^k is the continuous streaming plus removal operator defined by the left hand side of Eq. (7.1). The m -th approximate LDFE solution to Eq. (7.2) (m is the index of inner HO batches) is represented as $\tilde{I}^{n+1,(m)}$.

The m -th residual is defined as $r^{(m)} = q - \mathbf{L}^k \tilde{I}^{n+1,(m)}$. For reference, the residual at iteration m in the HO solve is

$$r^{(m),k+1/2} = \frac{\sigma_s}{2} \phi^{n+1,k} + \frac{1}{2} (\sigma_a a c T^4)^{n+1,k} + \frac{\tilde{I}^n}{c \Delta t} - \left(\mu \frac{\partial \tilde{I}^{n+1,k+1/2}}{\partial x} + \left(\sigma_t + \frac{1}{c \Delta t} \right) \tilde{I}^{n+1,k+1/2} \right)^{(m)} \quad (7.3)$$

where the k terms are LD in space on the coarsest mesh and are not recalculated at any point during the HO solve. The functional form of \tilde{I}^n is defined from the final HO solution of the previous time step.

Addition of $\mathbf{L}I^{n+1} - q = 0$ to the residual equation and manipulation of the result yields the error equation

$$\mathbf{L}(I^{n+1} - \tilde{I}^{n+1,(m)}) = \mathbf{L}\epsilon^{(m)} = r^{(m)} \quad (7.4)$$

where I^{n+1} is the exact solution and $\epsilon^{(m)}$ is the true error in $\tilde{I}^{n+1,(m)}$. We have suppressed the HOLO iteration indices because the LO estimated q^k and \mathbf{L}^k remain constant over the entire HO solve. The \mathbf{L} operator in the above equation is inverted yielding the Monte Carlo LDFE projection of the error in $\tilde{I}^{n+1,(m)}$, i.e.,

$$\tilde{\epsilon}^{(m)} = \mathbf{L}^{-1} r^{(m)} \quad (7.5)$$

where \mathbf{L}^{-1} is the Monte Carlo inversion of the streaming and removal operator. This inversion is strictly a standard Monte Carlo simulation. It is noted that the exact error in $\tilde{I}^{n+1,(m)}$ (with respect to Eq. (7.1)) is being estimated with MC; tallies produce a projection of the error onto a LDFE space-angle trial space. The space-angle moments of the error computed as $\tilde{\epsilon}^{(m)}$ can be added to the moments of $\tilde{I}^{n+1,(m)}$ to produce a more accurate solution.

Here, we emphasize the solution $\tilde{I}^{n+1,(m)}$ represents the LD FE projection of the exact Monte Carlo solution to the transport problem defined by Eq. (7.1). The discretization error is in q , i.e., the LD spatial representation of the emission and scattering source and the LD FE space-angle projection $\tilde{I}^n(x, \mu)$. The projection of the intensity is in general far more accurate than a standard finite element solution, e.g., a S_N collocation method in angle. In typical IMC calculations, the average energy deposition within a cell is computed using a standard path-length volumetric flux tally; the zeroth moment of the LD FE projection of ϵ is computed using an equivalent tally, preserving the zeroth moment of the true error.

Volumetric flux tallies over each space-angle element are required to estimate $\tilde{\epsilon}^{(m)}$. The LD approximation in space is used to relate the outflow within a cell to the volumetric moments, eliminating the need for face-averaged tallies. The procedure for representing the solution, sampling with negative and positive weight particles, and tally definitions are given in Appendix 7.3.

The ECMC algorithm is

1. Initialize the guess for $\tilde{I}^{n+1,(0)}$ to \tilde{I}^n or the projection of \tilde{I}^{n+1} from the latest HO solve
2. Compute $r^{(m)}$.
3. Perform a MC simulation to obtain $\tilde{\epsilon}^{(m)} = \mathbf{L}^{-1}r^{(m)}$
4. Compute a new estimate of the intensity $\tilde{I}^{n+1,(m+1)} = \tilde{I}^{n+1,(m)} + \tilde{\epsilon}^{(m)}$
5. Repeat steps 2 – 4 until desired convergence criteria is achieved.

The initial guess for the angular intensity $I^{n+1,(0)}$ is computed based on the previous solution for \tilde{I}^n . This is a critical step in the algorithm; it significantly reduces the

required number of particles per time step because the intensity does not change drastically between time steps in optically-thick regions. It is noted that the ECMC batch (steps 1-4 of the algorithm) results in essentially the same estimate of the solution as the residual formulation used in [?]. The primary difference is that our method uses an LDFF trial space and iterates on the solution estimate by recomputing the residual.

Exponential convergence is obtained if the error ϵ is reduced each batch. With each batch, a better estimate of the solution is being used to compute the new residual, decreasing the magnitude of the MC residual source at each iteration m , relative to the solution I^{n+1} . Each MC estimate of the moments of ϵ still has a statistical uncertainty that is governed by the standard $1/\sqrt{N}$ convergence rate [4], for a particular source $r^{(m)}$, where N is the number of histories performed. If the statistical estimate of the projection $\tilde{\epsilon}$ is not sufficiently accurate, then the iterations would diverge. It is noted that there is statistical correlation across batches because $I^{n+1,(m+1)}$ and $\epsilon^{(m)}$ are correlated through $I^{n+1,(m)}$ and the MC source $r^{(m)}$.

Because the exact angular intensity does not in general lie within the LDFF trial space, the iterative estimate of the error will eventually stagnate once the error cannot be sufficiently represented by a given FE mesh. An adaptive h -refinement algorithm has been implemented that can be used to allow the system to continue converging towards the exact solution [3, ?]. For TRT problems where absorption-reemission physics dominate, the diffusive and slowly varying regions of the problem require a less refined angular mesh to capture the solution than typical neutronics problems. However, greater spatial resolution is needed due to steep spatial gradients. Once error stagnation has occurred (and mesh refinement has reached a maximum level), additional histories can be performed with a fixed residual source to estimate the remaining error in the current solution. Although the remaining error will converge

statistically at a standard $1/\sqrt{N}$ convergence rate, the remaining error will be much smaller than for a standard MC simulation, producing a much more efficient solution method overall.

For the HO solver, in cells near the radiation wavefront, the LDFE trial space results in negative values in $\tilde{I}^{n+1}(x, \mu)$, similar to the LO solver. Because the residual formulation in ECMC allows for negative weight particles to occur, currently we do not treat these cells specially. We detect if the consistency terms lie in the appropriate half space at the end of the HO solve, an indication that the intensity was negative within that cell. If the terms are non-physical, then they are replaced with the corresponding S_2 -equivalent value. In general, in such cells where the trial space cannot accurately represent the solution, error stagnation will rapidly occur.

7.2 MC solution with LDD trial space

The inclusion of the outflow discontinuity has a minimal effect on the treatment of the residual source. The residual source and process of estimating moments of the error on the interior of a space-angle cell is unchanged. The process of estimating the solution on the outgoing face requires tallying the solution when particles leave a cell. The tallying process is discussed later in Section 8.7.

Applying L to the LDD trial space, as shown in Fig. ??, results in two δ functions at each interior face. For positive flow, at a face $x_{i+1/2}$, the face portion of the residual is defined as

$$r_{\text{face}}(x_{i+1/2}) = -\mu \frac{\partial \tilde{I}^{(m)}}{\partial x} \Big|_{x_{i+1/2}} \quad (7.6)$$

$$= r_{\text{face}}(x_{i+1/2}^-) \delta^-(x - x_{i+1/2}) + r_{\text{face}}(x_{i+1/2}^+) \delta^+(x - x_{i+1/2}) \quad (7.7)$$

where

$$r_{\text{face}}(x_{i+1/2}^-) = -\mu \left(\tilde{I}^{(m)}(x_{i+1/2}, \mu) - \tilde{I}^{(m)}(x_{i+1/2}^-, \mu) \right) \quad (7.8)$$

$$r_{\text{face}}(x_{i+1/2}^+) = -\mu \left(\tilde{I}^{(m)}(x_{i+1/2}^+, \mu) - \tilde{I}^{(m)}(x_{i+1/2}, \mu) \right). \quad (7.9)$$

Here, $I^{(m)}(x_{i+1/2}^+)$ and $I^{(m)}(x_{i+1/2}^-)$ are the LD solution extrapolated to $x_{i+1/2}$ from the x cell i and cell $i + 1$, respectively. Particles sampled from the two δ -functions have the same starting location. The only difference is, for positive μ , particles sampled from $r_{\text{face}}(x_{i+1/2}^-)$ will contribute to the face tally at $x_{i+1/2}$; the opposite is true for negative μ .

To reduce variance, we do not sample the two δ functions independently. Instead, we combine the two δ -functions into a single face source, do not score particles at the face from which they are sampled. To account for the untallied error, we add the analytic contribution to the error from the face source to the corresponding face at the end of a batch. It is noted the combination of the two δ -functions produces the same residual source as the original LD residual.

Define the additional error contribution from the face sources at $x_{i+1/2}$ as $\delta\epsilon^{(m)}$. This additional error is tallied everywhere by MC, except for at $x_{i+1/2}$. The transport equation satisfied by $\delta\epsilon^{(m)}$, for positive μ , with effective total cross section $\hat{\sigma}_t$, is

$$\mu \frac{\partial \delta\epsilon^{(m)}}{\partial x} + \hat{\sigma}_t \delta\epsilon^{(m)} = r_{\text{face}}(x_{i+1/2}^-) \delta^-(x - x_{i+1/2}) + r_{\text{face}}(x_{i+1/2}^+) \delta^+(x - x_{i+1/2}) \quad (7.10)$$

This equation is integrated from $x_{i+1/2} - \alpha$ to $x_{i+1/2}$ to produce

$$\mu \delta\epsilon^{(m)}(x_{i+1/2}, \mu) - \mu \delta\epsilon^{(m)}(x_{i+1/2} - \alpha, \mu) + \int_{x_{i+1/2} - \alpha}^0 \hat{\sigma}_t \delta\epsilon^{(m)} dx$$

$$= r_{\text{face}}(x_{i+1/2}^-) + \int_{x_{i+1/2}-\alpha}^0 r_{\text{face}}(x_{i+1/2}^+) \delta^+(x - x_{i+1/2}) dx. \quad (7.11)$$

The integral on the right side of the equation is zero because $\delta^+(x - x_{i+1/2})$ is zero for $(-\infty, x_{i+1/2}]$. The limit of the above equation is taken as $\alpha \rightarrow 0$, i.e.,

$$\lim_{\alpha \rightarrow 0} \left(\mu \delta \epsilon^{(m)}(x_{i+1/2}, \mu) - \mu \delta \epsilon^{(m)}(x_{i+1/2} - \alpha, \mu) + \int_{x_{i+1/2}-\alpha}^0 \hat{\sigma}_t \delta \epsilon^{(m)} dx \right) = \lim_{\alpha \rightarrow 0} r_{\text{face}}(x_{i+1/2}^-) \quad (7.12)$$

The integral goes to zero because $\delta \epsilon^{(m)}$ is smooth on the interior of the cell, and $\mu \delta \epsilon^{(m)}(x_{i+1/2} - \alpha, \mu)$ goes to zero because there is no source upstream of $x_{i+1/2}^-$. Thus, the final solution is

$$\delta \epsilon^{(m)}(x_{i+1/2}, \mu) = \frac{r_{\text{face}}(x_{i+1/2}^-)}{\mu} = \tilde{I}^{(m)}(x_{i+1/2}^-, \mu) - \tilde{I}^{(m)}(x_{i+1/2}, \mu). \quad (7.13)$$

The update for $I(x_{i+1/2}, \mu)$ is

$$\tilde{I}^{(m+1)}(x_{i+1/2}, \mu) = \tilde{I}^{(m)}(x_{i+1/2}, \mu) + \epsilon^{(m)}(x_{i+1/2}, \mu) + \delta \epsilon^{(m)}(x_{i+1/2}, \mu) \quad (7.14)$$

$$= \tilde{I}^{(m)}(x_{i+1/2}^-, \mu) + \epsilon^{(m)}(x_{i+1/2}, \mu). \quad (7.15)$$

This result has the peculiar effect that the estimation of the solution on a face depends only on the interior solution $\tilde{I}^{(m)}(x_{i+1/2}^-, \mu)$ and not the previous face value $\tilde{I}^{(m)}(x_{i+1/2}, \mu)$. This could be used to only estimate face values in particular cells, at any chosen batch.

7.3 Implementation of ECMC finite-element space, tallies, and residual sampling

The ECMC solver uses a finite element representation in space and angle. On the interior of the cell with the i -th spatial index and j -th angular index, the linear representation is defined as

$$\tilde{I}(x, \mu) = I_{a,ij} + \frac{2}{h_x} I_{x,ij} (x - x_i) + \frac{2}{h_\mu} I_{\mu,ij} (\mu - \mu_j), \quad x_{i-1/2} < x < x_{i+1/2}, \quad \mu_{j-1/2} \leq \mu \leq \mu_{j+1/2}$$

The spatial cell width is h_x , the angular width is h_μ , the center of the cell is (x_i, μ_j) , and

$$I_{a,ij} = \frac{1}{h_x h_\mu} \iint_{\mathcal{D}} I(x, \mu) dx d\mu \quad (7.16)$$

$$I_{x,ij} = \frac{6}{h_x h_\mu} \iint_{\mathcal{D}} \left(\frac{x - x_i}{h_x} \right) I(x, \mu) dx d\mu \quad (7.17)$$

$$I_{\mu,ij} = \frac{6}{h_x h_\mu} \iint_{\mathcal{D}} \left(\frac{\mu - \mu_j}{h_\mu} \right) I(x, \mu) dx d\mu, \quad (7.18)$$

where $\mathcal{D} : x_{i-1/2} \leq x \leq x_{i+1/2} \times \mu_{j-1/2} \leq \mu \leq \mu_{j+1/2}$. Standard upwinding in space is used to define $I(\mu)$ on incoming faces.

This representation can directly be plugged into Eq. (7.3) and evaluated to produce the residual source in the ECMC HO transport problem. The MC source $r^{(m)}(x, \mu)$ in Eq. (7.5) consists of both face and volumetric sources and can produce positive and negative weight particles. The distribution for sampling particle coordinates, in space and angle, is based on the L_1 norm over space and angle of the residual [3]. A particular cell volume or face is sampled, and then rejection sampling [4] is used to sample from the appropriate distribution on the face or interior of the space-angle cell. If the residual is negative at the sampled coordinates, the

weight of the particle history is negative.

During a MC batch, moments of the error are tallied. The necessary moments of the error are defined analogously to Eq.'s (7.16)–(7.18). The tallies are evaluated by weighting the particle density with the appropriate basis function and integrating along the history path through the cell. For the cell average, the n -th particle makes the contribution

$$\epsilon_{a,ij}^n = \frac{1}{h_x h_\mu} \int_{s_o^n}^{s_f^n} w^n(x, \mu) ds, \quad (7.19)$$

where s_o^n and s_f^n are the beginning and end of the n -th particle track in the cell and $w(x, \mu)$ is the weight of the error particle in the MC simulation. Weight is attenuated exponentially, i.e., $w(x, \mu) \propto \exp(-\sigma_t |x/\mu|)$. Substitution of the exponential attenuation of the weight produces the result

$$\epsilon_{a,ij}^n = \frac{w(x_0, \mu)}{\sigma_t h_x h_\mu} (1 - e^{-\sigma_t s^n}). \quad (7.20)$$

Here, $w(x_0, \mu)$ is the particle weight at the start of the path and s^n is the length of the track. The contribution of a particle track to ϵ_x is given by

$$\epsilon_{x,ij}^n = \frac{w(x_0, \mu)}{h_x^2 h_\mu \sigma_t} \left[x_0 - x_f e^{-\sigma_t s^n} + \left(\frac{\mu}{\sigma_t} - x_i \right) (1 - e^{-\sigma_t s^n}) \right], \quad (7.21)$$

where x_0 and x_f are the beginning and ending x coordinates of the n -th path. The contribution to the first moment in μ is

$$\epsilon_{\mu,ij}^n = \frac{w(x_0, \mu)}{h_\mu^2 h_x \sigma_t} (\mu - \mu_j) (1 - e^{-\sigma_t s^n}), \quad (7.22)$$

where the particle x -direction cosine μ does not change because it is a pure-absorber simulation. Finally, the moments of the error are simply the average contribution of

all particles.

7.4 Adaptive Mesh Refinement

This section describes the adaptive refinement strategy for the ECMC algorithm. Detailed equations for performing projections between meshes and computing the residual source on the refined meshes can be found in [3]. At the end of the ECMC batch, refinement is performed in space-angle cells based on a jump indicator. The jump indicator is the magnitude of the different between $I(x, \mu)$ in adjacent cells, averaged over each edge. The value of the largest jump, out of the four edges within a cell, is used as the indicator for that cell. Based on this indicator, the 20% of cells with the largest jump are refined. Future work will explore simply using ϵ to indicate refinement, rather than the jump error. The refinement of a cell is chosen to be symmetric, with each space-angle cell divided into four equal-sized cells. The solution for $\tilde{I}^{n+1}(x, \mu)$ of the batch is projected onto the finer mesh for the next batch. Because the dimensionality of the sample space has increased, we increase the number of histories per batch s.t. the ratio of the number of histories to total cells is approximately constant for all meshes. At the end of the last HO solve in a time step, \tilde{I}^{n+1} is projected back onto the original, coarsest mesh and stored as \tilde{I}^n for the next time step.

7.4.1 Continuous Weight Deposition Tallies

As in [?], because we are solving a pure absorber problem with Monte Carlo, we will allow particles to stream without absorption to reduce statistical variance in the tallies. The weight of particles is reduced deterministically along the path as they stream, with no need to sample a path length. Because particles are exponentially attenuated, the normalized weight is adjusted as $w(x, \mu) = w(x_0, \mu) \exp(-\sigma_t |(x - x_0)/\mu|)$, where x_0 is the starting location of the path. The tallies account for the

continuously changing weight, as given in Appendix 7.3. Histories are allowed to stream in this manner for 6 mean free paths (mfp)) before switching to analog path length sampling; this limits the tracking of very small weight histories. The choice of 6 mfp allows particles to continuously deposit weight until they reach 0.25% of their original weight. Path lengths are tracked in terms of mfp, so there is no need to resample at material interfaces.

7.4.2 *Modified Systematic Sampling Algorithm*

As another way to improve efficiency, a modified systematic sampling method [4] was used for determining source particle locations. The goal is to effectively distribute particle histories to regions of importance, but to sample a sufficient number of histories in less probable regions to prevent large statistical noise. However, there is no need to sample histories in regions in thermal equilibrium. The residual gives a good indication of where histories are most likely to contribute to the error, particularly in optically thick cells where particles do not transport long distances. In the sampling algorithm the number of particle histories sampled in each space-angle cell is predetermined and proportional to the magnitude of the residual, including face and volumetric sources, within that cell. Then, for the predetermined number of histories within a cell, the source location is randomly sampled according to the residual source distribution of that cell. In cells where the relative magnitude of the residual is on the order of roundoff no particle histories are sampled. In these regions the problem is remaining in equilibrium and the solution is known exactly. For cells that are significant, but have a predetermined number of histories below some preset minimum N_{min} , the number of histories sampled in that cell is set to N_{min} . This is to limit bad statistics in low probability cells (this would be important for adaptively refined meshes). In the simulations performed for this work $N_{min} = 1$. This choice

was made to keep the total number of histories per time step constant throughout the simulation for comparison to IMC.

7.5 COMPUTATIONAL RESULTS

We will compare results of the HOLO method to IMC with a source tilting algorithm for two test problems [?]. Also, we briefly compare performance in Section 7.5.3. For all IMC results, no local, discrete diffusion acceleration methods for effective scattering (e.g., those in [?, ?]) are applied. Finally, we will demonstrate the efficiency advantage of ECMC in our HOLO algorithm by comparing the results to the same HOLO algorithm if the ECMC algorithm is replaced with a standard Monte Carlo (SMC) simulation. Results are also given for the case of a single ECMC batch, which is similar to a RMC method.

A measure of variance in cell-averaged scalar intensities was calculated to provide a quantitative measure of the statistical accuracy of different solution methods. To form sample standard deviations, twenty independent simulations for each particular result were performed using unique random number generator seeds. The variance of a particular cell-averaged $\phi(x)$ is

$$S_i^2 = \frac{20}{20-1} \sum_{l=1}^{20} (\overline{\phi}_i - \phi_i^l)^2, \quad (7.23)$$

where ϕ_i^l is the cell-averaged scalar intensity for cell i from the l -th of 20 independent simulations and $\overline{\phi}_i$ is the corresponding sample mean from the 20 simulations. To provide a normalized, spatially-integrated result, we form a norm over cells as

$$\|s\| = \left(\frac{\sum_{i=1}^{N_c} S_i^2}{\sum_{i=1}^{N_c} \overline{\phi}_i^2} \right)^{1/2}, \quad (7.24)$$

where N_c is the number of spatial cells.

We will also form a figure of merit (FOM) to demonstrate how statistical accuracy scales with the number of histories performed. Our FOM is defined as

$$\text{FOM} = \frac{1}{N_{\text{tot}} \|s\|^2} \quad (7.25)$$

where N_{tot} is the total number of histories performed over the simulation. A larger value of the FOM indicates that the method produced less variance in the solution per history performed, for a given problem. This form of the FOM is typically chosen because the variance is expected to reduce inversely proportional to N_{tot} , so for standard MC simulations the FOM becomes, on average, independent of N_{tot} [4]. The FOM is not necessarily expected to be independent of N_{tot} for IMC or our HOLO method due to correlation of the solution between time steps; additionally, ECMC has correlations between batches.

7.5.1 Marshak Wave

For the first problem, the radiation and material energies are initially in equilibrium at 2.5×10^{-5} keV. An isotropic incident intensity of 0.150 keV is applied at $x = 0$; the incident intensity on the right boundary is 2.5×10^{-5} keV. The material properties are $\rho = 1$ g cm $^{-3}$ and $c_v = 0.013784$ jks/keV-g. The absorption cross section varies as $\sigma(T) = 0.001 \rho T^{-3}$ (cm $^{-1}$). The simulation was advanced until $t = 5$ sh (1 sh $\equiv 10^{-8}$ s) with a fixed time step size of 0.001 sh. For comparison purposes, we have not used adaptive mesh refinement, only performed one HOLO iteration per time step, and use a fixed 3 HO batches with equal number of histories per batch. A relative tolerance of 10^{-6} for the change in $\phi(x)$ and $T(x)$ was used for the LO newton solver for all results. Radiation energy distributions are plotted as an equivalent temperature given by $T_r = (\phi/(ac))^{0.25}$. Cell-averaged quantities are

plotted. Although isotropic scattering is handled by the LO solver in the algorithm described above, we have only considered problems with $\sigma_s = 0$ here. Results for neutronics with isotropic scattering included are given in [?].

Fig. 7.1a compares the cell-averaged radiation temperatures for the IMC and HOLO method with ECMC, for various number of spatial mesh cells N_c ; we have used HOLO-ECMC to denote our algorithm because later results will use different HO solvers. For all IMC calculations, $n = 10^5$ histories per time step were used. For the HOLO method, we have used 4 equal-sized cells in μ for the finite-element angular mesh used by the ECMC solver. The spatial grid is the same for the HO and LO solvers. For the cases of $N_c = 25$ and $N_c = 200$, 4,000 histories per batch ($n = 12,000$ per time step) were used. For $N_c = 500$, 16,000 histories per time step were used due to increased number of space-angle cells that need to be sampled. The IMC and HOLO solutions agree as the mesh is converged. There is similar agreement in the location of the wavefront due to the linear shape of the emission source over a cell. The cells nearest the wavefront required use of the lumping-equivalent discretization and S_2 equivalent terms during the LO solve, resulting in strictly positive solutions.

Fig. 7.1b compares solutions for the case of 200 cells. For the IMC solution 10^5 histories per time step were simulated; for the HOLO method only 4,000 histories per batch (12,000 per time step) were simulated. There is significant statistical noise in the IMC solution compared to the HOLO solution. The HOLO solution visually demonstrates no statistical noise. Because the ECMC solve is only determining the change over the time step, the statistical noise in the result is small relative to the magnitude of I^{n+1} . Also, the source sampling only places particles in cells where the residual is large. No particles are sampled in the equilibrium region out front of the wave.

Table 7.1 compares $\|s\|$ and the FOM for IMC and the HOLO method, for different numbers of histories per time step. The FOM results are normalized to the value for IMC with $n = 12,000$. The HOLO method demonstrates less variance for the same numbers of histories, producing FOM values that are two orders of magnitude greater than for IMC. Where as the FOM remains relatively constant for IMC, as n is increased the FOM improves for the HOLO method. This is a result of each batch producing more statistically accurate estimates of the error ϵ , which results in an increased convergence rate of ϵ overall.

Table 7.1: **Comparison of sample statistics for the Marshak Wave problem. Simulation end time is $t = 5$ sh.**

hists./step	$\ s\ $		FOM	
	IMC	HOLO-ECMC	IMC	HOLO-ECMC
12,000	3.40%	0.28%	1	145
100,000	1.22%	0.057%	0.93	422

7.5.2 Two Material Problem

This problem consists of an optically thin (left) and an optically thick (right) material region, with temperature-independent cross sections. The material properties are given in Table 7.2. Initially the radiation and material energies are in equilibrium at a temperature of 0.05 keV. An isotropic incident intensity of 0.500 keV is applied at $x = 0$ at $t = 0$; the isotropic incident intensity on the right boundary is 0.05 keV. The simulation end time is 5 sh. For all HOLO simulations, we have used 8 equal-sized mesh cells in μ . As for the Marshak problem, the cells nearest the wavefront required use of the lumping-equivalent discretization and S_2 equivalent terms during

the LO solve.

Table 7.2: Material properties for two material problem

	$x \in [0, 0.5)$ cm	$x \in [0.5, 1.0]$ cm
σ_a (cm ⁻¹)	0.2	2000
ρ (g cm ⁻³)	0.01	10.0
c_v (jks/keV-g)	0.1	0.1

Fig. 7.2a compares the HOLO and IMC radiation temperatures at the end of the simulation. The IMC and HOLO results show good agreement over the finer mesh. On the coarse mesh ($N_c = 20$), the LDFE representation of T^4 in the HOLO method predicts the location of the wavefront more accurately than the IMC method with source tilting.

Fig. 7.2b demonstrates the benefit of ECMC as a HO solver compared to standard MC. The HOLO algorithm with the ECMC HO solver (HOLO-ECMC) results are for running 3 batches of 10,000 histories, per time step. The solution for the HOLO method with a standard MC solver as the HO solver (HOLO-SMC) with standard source sampling uses 10^5 histories per time step. The HOLO-SMC solution demonstrates significant statistical noise. This noise is introduced into the LO solver by bad statistics in computing the consistency terms. Also plotted is an S_2 solution obtained with consistency terms that are equivalent to S_2 and no HO correction. The S_2 solution results in an artificially fast wavefront, as expected, demonstrating the necessity of HO correction in this problem.

Table 7.3 compares the FOM and $\|s\|$ for IMC and the HOLO-ECMC method. The FOM values are normalized to the value for IMC with $n = 30,000$. The end time

was reduced to 2 sh for these results to reduce computational times. The reduction in variance by the HOLO method over IMC is substantial. The improvement of the FOM for the HOLO method compared to IMC is greater than for the Marshak wave problem. This improvement is because the wave moves much slower in right region of this problem, due to the large, constant cross section. Also, in the optically thin region of the problem the solution quickly comes to equilibrium. Thus, the ECMC algorithm has to estimate a very small change in the intensity over a time step. Additionally, difficulties in resolving the solution at the wavefront are not as severe compared to the Marshak wave problem, where the cold cells have a much larger cross section.

Table 7.3: **Comparison of sample statistics for the two material problem for 200 x cells. Simulation end time is $t = 2$ sh.**

hist./step	$\ s\ $		s_{\max}	
	IMC	HOLO-ECMC	IMC	HOLO-ECMC
30,000	3.63%	0.01%	1	104,000
100,000	1.96%	0.003%	1.03	360,000

7.5.3 Performance comparison of IMC and HOLO-ECMC

We have measured the total CPU time for simulations to provide a simplified measure of the computational cost. These results compare how computational times change the two different problems and how the methods scale with time step size and particle histories. Absolute comparisons in the computational cost of the two methods cannot be made because the methods are implemented in different code infrastructures. Additionally, the HOLO method fully resolves non-linearities at

each time step, whereas IMC is using a single linearized step with lagged cross sections. Simulations were performed on the same processor, using a single CPU core. Reported times are the average of 10 runs and all results used 200 x cells, $\Delta t = 0.001$ sh, and an end time of $t = 2$ sh.

Table 7.4 compares the average simulation time per history performed for the Marshak wave problem. The average time per history is computed by dividing the total simulation time by the total number of histories performed (e.g., the time of the LO solves is included for the HOLO method). Results are given for different numbers of histories per time step, as well as a case with an increased time step size. The table also includes the number of LO iterations performed per LO solve for the HOLO method, averaged over all time steps; there are two LO solves per time step. The same results are reported for the two material problem in Table 7.5.

The HOLO method does not scale with the number of histories due to the fixed cost of the LO solver. The cost of the LO solver is more significant at the lower history counts compared to the case of 10^5 histories, for both problems. There is a slight increase in the number of newton iterations as the time step is increased, but the average cost per history is not significantly increased. Similar to the results in [?], as the time step size is increased to 0.005 sh, the IMC method increases in cost per time step, due to an increase in effective scattering events, particularly for the two material problem. Because the cross sections in the two material problem do not have a T^{-3} behavior, the cost of the effective scattering cross section in IMC is more apparent, resulting in longer simulation times.

Table 7.4: **Comparison of average CPU times per history and LO iteration counts for the Marshak Wave problem.**

hists./step	$\Delta t(sh)$	IMC ($\mu s/hist.$)	HOLO-ECMC ($\mu s/hist$)	Newton iters./LO solve
100,000	0.001	10	5.3	3.8
12,000	0.001	9.7	8.1	4.1
12,000	0.005	19	9.4	6.2

Table 7.5: **Average CPU times per history and LO iteration counts required for the two material problem.**

hists./step	$\Delta t(sh)$	IMC ($\mu s/hist.$)	HOLO-ECMC ($\mu s/hist$)	Newton iters./LO Solve
100,000	0.001	17	3.5	4.9
30,000	0.001	18	6.9	5.0
30,000	0.005	59	7.4	7.6

7.5.4 Comparison of different HO Solvers

In this section we compare the results of our HOLO algorithm with different HO solvers for the test problems in Section 7.5.1 and 7.5.2. We compare standard MC (SMC) as a HO solver to the HOLO algorithm with ECMC using both three batches and a single batch, per time step. The use of a single batch is similar to the approach in [?]. Results are tabulated for 200 x cells, using the same total number of histories per time step, divided evenly among the batches.

Tables 7.6 and 7.7 compare the results for the Marshak wave and two material problems. The number of batches for each ECMC case is indicated in parenthesis. The FOM values are normalized to the reference IMC result for the corresponding problem. For HOLO-SMC there is minimal reduction in variance compared to IMC

in the Marshak wave problem, and the two material problem actually demonstrates worse variance. Sufficient histories are not performed to accurately estimate consistency terms throughout the problem. For ECMC, a single batch produces less variance than the case of three equal batches. This indicates that if the solution cannot be resolved with the trial space (i.e., the intensity is driven negative), a single large batch may be more accurate. It is noted that these results only account for statistical variance, and do not account for accuracy, which will depend on the estimates of ϵ computed each iteration.

Table 7.6: **Comparison of sample statistics for the Marshak Wave problem. Number of ECMC batches is indicated in parenthesis.**

	$\ s\ $			FOM		
hists./step	SMC	ECMC (1)	ECMC (3)	SMC	ECMC (1)	ECMC (3)
12,000	2.77%	0.10%	0.28%	1.50	1280	145
100,000	0.98%	0.03%	0.06%	1.43	1270	422

Table 7.7: **Comparison of sample standard deviations for the two material problem. Number of ECMC batches is indicated in parenthesis.**

	$\ s\ $			FOM		
hists./step	SMC	ECMC (1)	ECMC (3)	SMC	ECMC (1)	ECMC (3)
30,000	5.35%	0.002953%	0.011%	0.46	1.51×10^6	1.04×10^4
100,000	2.85%	0.001474%	0.0033%	0.49	1.80×10^6	3.59×10^4

7.5.5 *Pre-heated Marshak wave problem and adaptive mesh refinement*

Finally, to demonstrate the potential of ECMC with adaptive space-angle mesh refinement, we perform results for a modified Marshak wave problem. The problem is modified so that the LDFE trial space can accurately represent the solution (i.e., the intensity is strictly positive). Mesh refinement is of minimal use in the previous problems due to most of the error existing at the wavefronts, caused by the large cross sections. The modified problem has the same material properties and left boundary source as the Marshak wave problem in Section 7.5.1. However, the initial equilibrium temperature and right boundary condition are raised to 0.03 keV. The higher initial temperature reduces the initial cross section and increases the strength of the emission source within cells. The LDFE mesh can now sufficiently resolve the solution and lumping is not required by the LO solution. The simulation end time is 0.5 sh with a constant time step of $\Delta t = 0.001$ sh.

Fig. 7.3 compares the result from HOLO-ECMC with three batches and IMC. It was found that 100 x cells was sufficient to resolve the solution spatially. There is slightly more noise in IMC past the wavefront due to the increased emission source. Additionally, the opacity is thin enough that some photon energy is able to reach the right boundary, in front of the wavefront.

Table 7.8 compares the variances for this problem for the various HO solvers. The FOM values are normalized to the case of HOLO-SMC with 12,000 histories per time step. The final row of the table is for an ECMC simulation with adaptive mesh refinement (AMR). The strategy for refinement is described in Appendix 7.4. The adaptive mesh refinement case used a total of nine batches, with a refinement occurring at the end of the third and sixth batches, for every time step. The initial number of histories was adjusted so that the average number of histories per time

step is near 100,000; on average 99,881 histories per time step were used. All ECMC meshes used 4 equally-spaced μ cells initially. The improvement in variance by ECMC compared to SMC is not as significant as for the other problems. This is a result of the reduced opacity leading to intensity changing throughout the spatial and angular domains. The FOM is highest for the case of ECMC with adaptive refinement. When the solution can be resolved, the adaptive algorithm allows for a higher convergence rate of statistical variance. It is noted that the consistency terms and LO solution are still computed over the fixed, coarser mesh. However, in general, the refined mesh can produce higher accuracy in consistency terms that is not being measured by the FOM.

Table 7.8: Comparison of sample statistics for the pre-heated marshak wave problem for 100 x cells. Number of ECMC batches is indicated in parenthesis.

	$\ s\ $			FOM		
hists./step	SMC	ECMC (1)	ECMC (3)	SMC	ECMC (1)	ECMC (3)
12,000	0.86%	0.13%	0.24%	1	41	13
100,000	0.16%	0.042%	0.08%	3.32	52	15
99,881 (AMR, 9 batches)	—	0.038%		—	61	

7.6 Accuracy in the Equilibrium Diffusion Limit

A critical aspect for any numerical solution to the thermal radiative transfer equations is preservation of the equilibrium diffusion limit (EDL). We expect the LD representation in the LO equations to preserve the equilibrium diffusion limit. In this limit, the MC HO solution will estimate angular consistency terms associated with an isotropic intensity, based on a spatially LD emission source. Because the

spatial closure produces equations that are equivalent to an LDFE solution to the S_2 equations, we expect the equations to preserve the equilibrium diffusion limit [?, ?].

We test a problem in the EDL by adjusting material properties to produce a strongly diffusive region. The EDL problem has constant cross sections with $\sigma_a = 1000 \text{ cm}^{-1}$, $\sigma_s = 10 \text{ cm}^{-1}$, $\rho c_v = 6.8784 \times 10^{-3} \text{ Jk keV}^{-1} \text{ cm}^{-3}$. The domain width is 0.1 cm and 4 μ cells and 3 batches of 4,000 histories are used for the single HO solve in all calculations. The simulation end time is 5 sh and a linear increase of 15% from $\Delta t = 0.001 \text{ sh}$ to a maximum $\Delta t = 0.01 \text{ sh}$ is used. We compare the LDFE LO solution to a LO solution using a step discretization, which is known to not preserve the EDL for S_N equations. The step discretization is implemented by using the scaled slope spatial closure in Sec. 8.6.2 with closure parameters $\gamma_i^\pm = 0$ for all cells.

The accuracy in the equilibrium diffusion limit is compared for the two spatial discretizations, for different mesh sizes, in Fig. 7.4. As demonstrated, the LDFE spatial discretization has converged spatially, where both 20 and 200 cells produce the same location of the wave front. However, the step discretization artificially propagates the energy forward; the inaccuracy is greater than what would be expected from simply truncation error. The step discretization will only be accurate if the mesh cells are on the order of a mean free path, which is very large for this problem. Although not plotted, the material temperature overlays the radiation temperature for the LDFE solution, in equilibrium with the radiation.

7.7 CONCLUSIONS

We have been able to produce solutions for Marshak wave test problems using a new HOLO method that are in agreement with IMC. Unlike IMC, our method requires no effective scattering events to be included in the MC simulation, which

limits the run time of particle tracking, while adding the cost of a LO newton solver. Average LO iteration counts did not significantly increase as the time step size was increased. The LDFF spatial representation mitigates issues with teleportation error, producing results with spatial accuracy comparable to IMC with source tilting. The ECMC approach, with initial guesses based on the previous radiation intensity, results in efficient reduction of statistical error and allows for particles to be distributed to largely varying regions of the problem. The LO solver resolves the non-linearities in the equations resulting in a fully implicit time discretization. The LO solver can accurately and efficiently resolve the solution in diffusive regions, while the HO transport solver provides the accuracy of a full transport treatment where necessary.

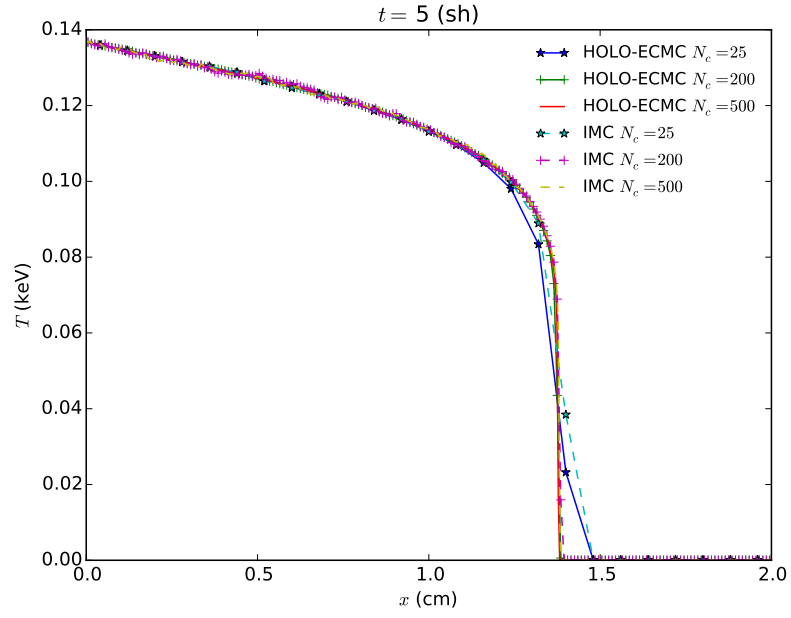
The primary difficulty to overcome in the ECMC algorithm is when the solution cannot be accurately represented by the trial space, e.g., in optically thick cells where the solution is driven negative. We are currently developing an approach to allow the ECMC iterations to continue converging globally when there are such regions present. It is necessary to ensure the closure in the LO system is consistent with the HO representation for the solution in such regions. The ability to represent the solution accurately in rapidly varying regions of the problem will be key for generalization of this method to higher dimensions. A formulation of the ECMC method that allows for time-continuous MC transport (similar to IMC) is also currently being investigated. This may reduce some of the loss of accuracy in optically thin regions due to the time discretization of the transport equation in the HO solver. However, greater time accuracy is not of primary concern as this method is intended for use in problems dominated by large absorption opacities, where the LO acceleration is critical. Inclusion of Compton scattering in this algorithm, which would introduce additional non-linear dependence through energy exchange with the material, is a

topic for future research.

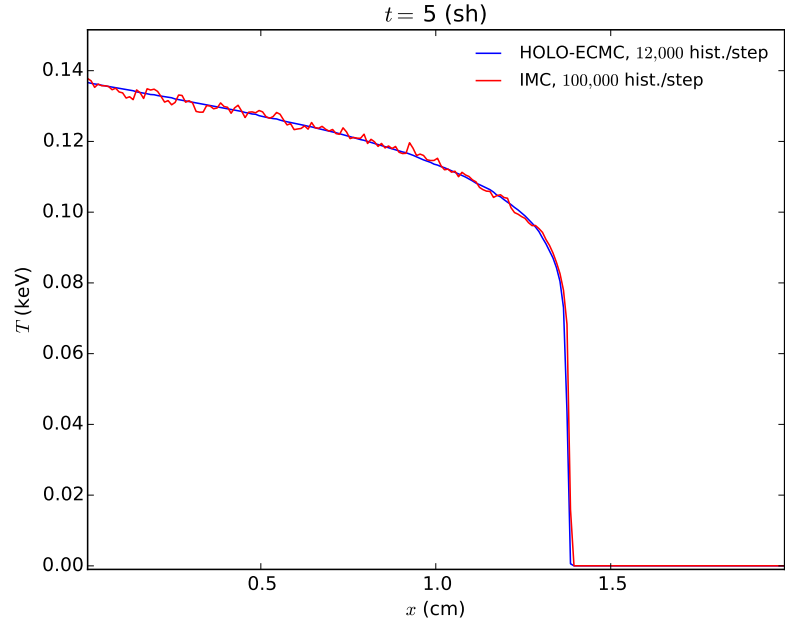
Future work will also explore the accuracy of the HOLO method, in particular, analyzing the optimal number of batches and the benefit of adaptive refinement. This will likely require the use of manufactured solutions. The sensitivity of the method to mesh sizes and time step sizes will be investigated more thoroughly. Ultimately, we plan to extend this method to multiple spatial dimensions for the case of multigroup TRT equations. For TRT problems, it is important that the LO spatial discretization satisfies the equilibrium diffusion limit. To extend to higher dimensions, our LDFE representation may require the use of a higher-degree spatial representation for the LO system to achieve the diffusion limit. Further asymptotic analysis on the method will be applied before implementation. It may be necessary to use a different LO system (e.g., the non-linear diffusion acceleration approach in [?]), if the S_2 -like equations become too inefficient or difficult to implement in higher dimensions. Alternatively, a variable Eddington Tensor approach may provide more stability in rapidly variable regions of the problem while still allowing for a consistent, LDFE solution that is efficiently solvable.

ACKNOWLEDGEMENTS

This research was supported with funding received from the DOE Office of Nuclear Energy’s Nuclear Energy University Programs, the DOE National Nuclear Security Administration, under Award Number(s) DE-NA0002376, and under Los Alamos National Security, LLC, for the National Nuclear Security Administration of the U.S. Department of Energy under contract DE-AC52-06NA25396.

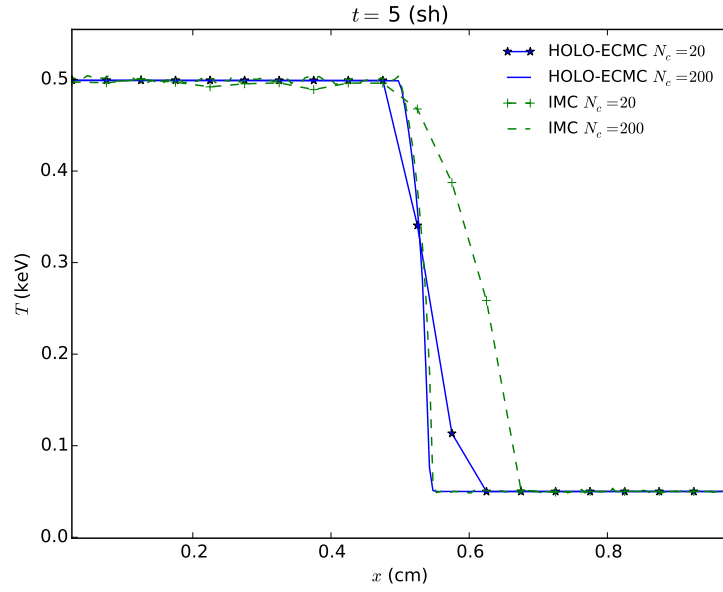


(a) Convergence of IMC and HOLO-ECMC solutions.

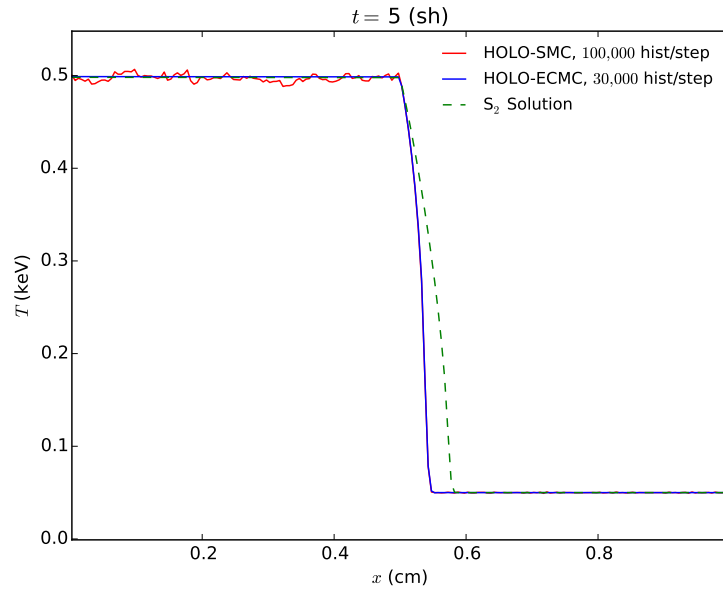


(b) Comparison of solutions for 200 spatial cells.

Figure 7.1: Comparison of radiation temperatures for Marshak wave problem at $t = 5$ sh.



(a) Comparison of IMC and HOLO-ECMC.



(b) Comparison of SMC and ECMC HO solvers.

Figure 7.2: Comparison of radiation temperatures for two material problems.

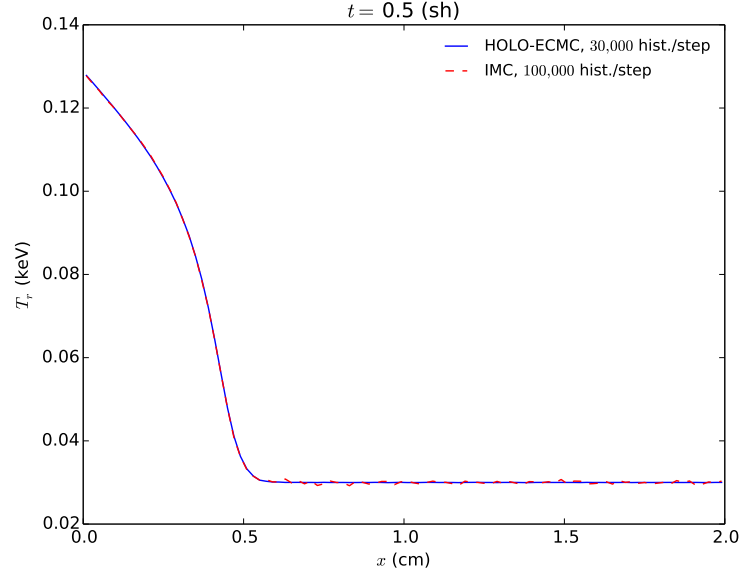


Figure 7.3: Comparison of radiation temperatures for the pre-heated Marshak wave problem for 100 x cells at $t = 0.5$ sh.

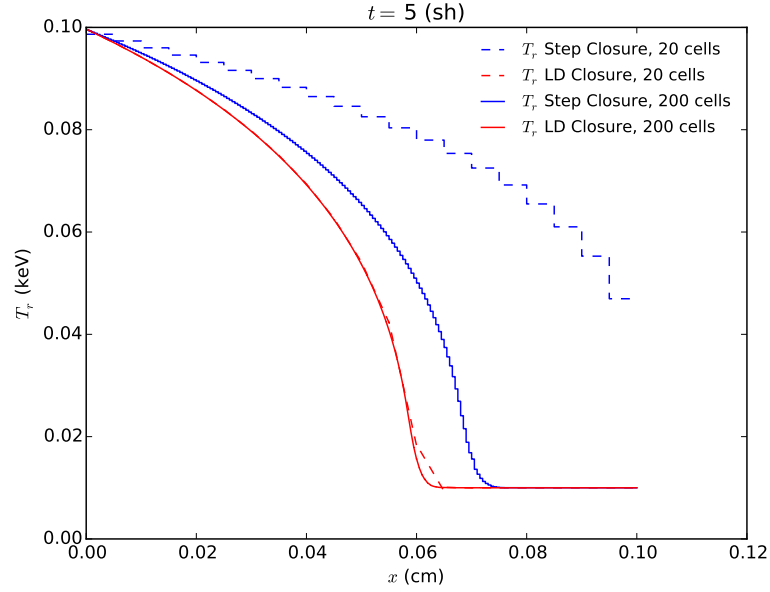


Figure 7.4: Comparison of T_r for step and LD FE discretizations of the LO equations in the equilibrium diffusion limit.

8. ACCELERATED ITERATIVE SOLUTION TO THE LO EQUATIONS

As described in Sec. ??, the fully-discrete, S_2 -like LO equations are not easy to directly inverted efficiently in higher spatial dimensions. To demonstrate a possible path forward in higher dimensions, we have investigated the use of a standard source iteration scheme to invert the scattering terms in the LO equations. As material properties become more diffusive (e.g., c_v is small and σ_a is large), the effective scattering cross sections becomes large. This results in a spectral radius of the source iterations that approaches unity [?]. These regimes are typical in TRT simulations, so an acceleration method for an iterative solution is critical. We have accelerated the source iterations with a nearly-consistent diffusion synthetic acceleration (DSA) method known as WLA [?, 6].

REWRITE: STUFF ABOUT LUMPING ETC. We have also recast the DSA method as a preconditioner to an iterative Krylov solution [?] of the LO equations. Generally, Krylov methods mitigate acceleration losses due to inconsistencies in the acceleration method. In higher dimensions, the use of a Krylov method is necessary for effective acceleration for nearly-consistent acceleration methods in problems with mixed optical thicknesses [?], e.g., typical radiative transfer problems. Also, applying the preconditioned-Krylov approach allows for the use of spatially lumped DSA equations as a preconditioner, with the LO equations using alternative fix-up methods. We expect better acceleration performance (DID WE GET IT?) when the LDD discretization is introduced into the LO equations.

In the remainder of this chapter is structured as follows: The source iteration solution to the LO equations is detailed. Then, the equations for the WLA DSA method are derived and the acceleration algorithm is given. The DSA method is

then recast as a preconditioner to a GMRES solution to the scattering iteration equations. Finally, results are given for a modified test problem which requires the use of acceleration.

8.1 Source Iteration Solution to the Linearized LO Equations

The linearized LO equations can be solved with a source iteration method [2, ?, ?]. In the source iteration process the scattering source is lagged, which uncouples unknowns between the two half-ranges. This produces a lower-triangular system where the spatial unknowns can be solved for sequentially along the two directions of flow via a standard sweeping procedure [2, ?]. Beginning at the left boundary, the positive unknowns can be determined for each cell from $i = 1, \dots, N_c$; because the inflow to the i -th cell is defined from the previous cell or boundary condition, a local system of equations can be solved for the $\langle \phi \rangle_{L,i}^+$ and $\langle \phi \rangle_{R,i}^+$ unknowns. The negative direction unknowns are determined similarly, starting from the right boundary towards the left. The newly computed half-range intensities can then be used to estimate the scattering source for the next iteration. This process is repeated until convergence.

The source iteration process can be written in operator notation as

$$\mathbf{M}\underline{\psi}^{l+1} = \frac{1}{2}\mathbf{S}\underline{\psi}^l + \underline{Q}, \quad (8.1)$$

where \mathbf{M} is the LO streaming and removal operator (i.e., the left-hand side of Eqs. (5.17)–(5.20) without the scattering terms included), $\underline{\psi}$ is a vector of the half-range FE moment unknowns, and the vector \underline{Q} contains the fixed source terms resulting from the linearized emission source and previous time step moments, for each equation. The source terms for the i -th element and the L equation, for both

half-ranges, are

$$(\underline{Q})_{i,L}^{\pm} = \frac{\langle \phi \rangle_L^{\pm}}{c\Delta t} + \frac{1}{2}f_i\sigma_{a,i}ac\langle (T^n)^4 \rangle_{L,i} \quad (8.2)$$

The scattering operator terms for the i -th element and the L equations are

$$(\underline{S}\psi^l)_{i,L}^{\pm} = (\sigma_{a,i}(1 - f_i) + \sigma_{s,i}) (\langle \phi^l \rangle_{i,L}^+ + \langle \phi^l \rangle_{i,L}^-). \quad (8.3)$$

Equivalent expressions are defined for the R moment equations and boundary conditions, forming a fully defined set of equations. The process of sweeping is denoted as \mathbf{M}^{-1} .

The scattering inversion must be performed within each Newton iteration. Thus, for the m -th Newton step, the source iteration process is defined as

1. Evaluate effective scattering and absorption cross sections with $\{T_i^m : i = 1, 2, \dots, N_c\}$.
2. Compute new scattering source $\frac{1}{2}\underline{S}\psi^l$.
3. Perform sweeps to calculate $\underline{\psi}^{l+1} = \mathbf{M}^{-1}\underline{S}\psi^l + \mathbf{M}^{-1}\underline{Q}$
4. If $\|\underline{\psi}^{l+1} - \underline{\psi}^l\|_2 < \text{tolerance } \|\underline{\psi}^{l+1}\|$, move to next Newton step.
5. Else: repeat steps 2–4.

8.2 Linear Diffusion Synthetic Acceleration

A form of DSA referred to as the WLA method is used to accelerate the source iterations [?, 6]. Between each sweep, an error equation for the scattering iterations is solved with an approximate angular discretization of the transport equation. The estimated error is used to correct the zeroth moment of the intensity unknowns. In operator notation, the DSA equations for a single iteration are

$$\mathbf{L}\psi^{l+1/2} = \frac{1}{2}\mathbf{S}\psi^l + \underline{Q} \quad (8.4)$$

$$\mathbf{D}\delta\phi^{l+1/2} = \mathbf{S}(\psi^{l+1/2} - \psi^l) \quad (8.5)$$

$$\psi^{l+1} = \psi^{l+1/2} + \delta\phi^{l+1/2}, \quad (8.6)$$

where $\delta\phi$ represents the error in the mean intensity unknowns. The operator \mathbf{D} represents a diffusion-like approximation to the transport equation. The DSA equations contain a standard finite-difference diffusion discretization that can be more efficiently inverted than the S_2 -like equations that are being accelerated (particularly in higher spatial dimensions), but will accurately resolve the slowly-converging, diffusive error modes.

It is important for the spatial discretization of Eq. (8.5) to be closely related to the discretization of the LO equations for the acceleration to be effective and stable [?]. The WLA method first solves a spatially-continuous discretization of the diffusion equation for the error at faces $\{x_{i+1/2}\}$. The error on the faces is then mapped onto the volumetric moment unknowns via a LD discretization of the P_1 equations [?]. The LD mapping resolves issues that would occur in optically-thick cells, while the continuous diffusion equation is accurate in the EDL where acceleration is important [?].

The continuous diffusion equation and mapping equations for the WLA method are derived in Appendix ???. To allow for the use of lumped or standard LD in the DSA equations, we introduce the factor θ , with $\theta = 1/3$ for standard LD, and $\theta = 1$ for lumped LD. The diffusion equation for the face at $x_{i+1/2}$ is

$$\begin{aligned} & \left(\frac{\sigma_{a,i+1}h_{i+1}}{4} (1 - \theta) - \frac{D_{i+1}}{h_{i+1}} \right) \delta\phi_{i+3/2} + \left(\frac{D_{i+1}}{h_{i+1}} + \frac{D_i}{h_i} + \left(\frac{1 + \theta}{2} \right) \left[\frac{\sigma_{a,i+1}h_{i+1}}{2} + \frac{\sigma_{a,i}h_i}{2} \right] \right) \delta\phi_{i+1/2} \\ & + \left(\frac{\sigma_{a,i}h_i}{4} (1 - \theta) - \frac{D_i}{h_i} \right) \delta\phi_{i-1/2} = \frac{h_{i+1}}{2} \langle q \rangle_{L,i+1} + \frac{h_i}{2} \langle q \rangle_{R,i} . \quad (8.7) \end{aligned}$$

The source in Eq. (8.7) is the residual for a given scattering iteration [?, 2]

$$\langle q \rangle_{L/R,i} = \sigma_{s,i} (\langle \phi^{l+1/2} \rangle_{L/R,i} - \langle \phi^l \rangle_{L/R,i}). \quad (8.8)$$

It is noted that there is no need to define the source differently for the lumped or standard LD DSA equations because it is in terms of moments.

The upwinding in the LO system exactly satisfies the inflow boundary conditions, therefore a vacuum boundary condition is applied to the diffusion error equations. Application of Eq. (??) gives the left boundary condition:

$$\left(\frac{1}{2} + \sigma_{a,1} h_1 \frac{1+\theta}{4} - \frac{D_1}{h_1} \right) \delta \phi_{1/2} + \left(\sigma_{a,1} h_1 \frac{1-\theta}{4} - \frac{D_1}{h_1} \right) \delta \phi_{3/2} = \frac{h_1}{2} \langle q \rangle_{L,1} \quad (8.9)$$

The boundary condition for the right-most face is

$$\left(\frac{1}{2} + \sigma_{a,I} h_I \frac{1+\theta}{4} - \frac{D_I}{h_I} \right) \delta \phi_{I+1/2} + \left(\sigma_{a,I} h_I \frac{1-\theta}{4} - \frac{D_I}{h_I} \right) \delta \phi_{I-1/2} = \frac{h_I}{2} \langle q \rangle_{R,I} \quad (8.10)$$

where I is the index of the last cell.

The system of equations formed from Eqs. (8.9), (8.10), and (8.7) can be solved directly with a banded matrix solver. Then, Eq. (??)–(??) are solved in each cell to map the face errors onto an LD representation over the interior. It is noted that unlike fully consistent DSA equations, the WLA-DSA algorithm does not preserve particle balance to round off. This is because the mapping procedure uses an approximate inflow to each cell, which is inconsistent with the partial outflows from adjacent cells.

Because we are interested in the time-dependent solution, we need to accelerate the solution for the half-range intensities, rather than just the zeroth moment. We do not accelerate the first moment of the angular intensity, as the solution for ΔJ is inaccurate due to the approximations introduced. The error in the half-range

moments, using the lumping notation, are

$$\langle \delta\phi \rangle_L^\pm = \frac{1+\theta}{4} \delta\phi_L^\pm + \frac{1-\theta}{4} \delta\phi_R^\pm \quad (8.11)$$

$$\langle \delta\phi \rangle_R^\pm = \frac{1-\theta}{4} \delta\phi_L^\pm + \frac{1+\theta}{4} \delta\phi_R^\pm, \quad (8.12)$$

8.2.1 The WLA-DSA Accelerated Source Iteration Algorithm

We define the process of solving the diffusion like equations and mapping the error unknowns back onto the moment equations as the operator \mathbf{D}^{-1} . The source iteration with linear DSA procedure, for the m -th Newton iteration, is then defined as

1. Evaluate effective scattering and absorption cross sections with $\{T_i^m : i = 1, 2, \dots, N_c\}$.
2. Compute new scattering source $\mathbf{S}\psi^l$.
3. Perform sweeps to calculate $\psi^{l+1/2} = \mathbf{M}^{-1}\mathbf{S}\psi^l + \mathbf{M}^{-1}Q$
4. Perform DSA iteration to solve $\phi^{l+1} = \mathbf{D}^{-1}\sigma_s(\phi^{l+1/2} - \phi^l)$
 - Solve continuous DSA equations, i.e., Eq. (8.7) and Eq. (??), for $\{\delta\phi_{i+1/2}^{l+1/2} : i = 0, 1, \dots, N_c\}$.
 - Map the continuous error onto the moment unknowns, via Eq. (??)–(??).
5. Add correction to the moment unknowns, e.g., $\phi_L^{\pm, l+1} = \phi_L^{\pm, l+1/2} + \delta\phi^{l+1/2}/2$.
6. If $\|\psi^{l+1} - \psi^l\| < \text{tolerance}$, exit
7. Else: repeat steps 4–9.

8.3 GMRES Solution to the LO Equations

The source iteration procedure can be recast as an iterative solution to a matrix equation. Using operator notation, we manipulate the moment equations to form a matrix equation:

$$(\mathbf{I} - \mathbf{M}^{-1}\mathbf{S}) \psi = \mathbf{M}^{-1}Q, \quad (8.13)$$

where I is an identity matrix. The GMRES method is used to iteratively solve the above linear system. The GMRES is an iterative Krylov solution method for asymmetric, sparse matrix equations [?]. Krylov solutions to a linear system repeatedly apply the matrix operator to vectors, projecting the system onto a Krylov subspace [?]. Rather than forming the full matrix system, we apply the operation of \mathbf{S} and \mathbf{M}^{-1} as detailed in Sec. (8.1) to apply $(\mathbf{I} - \mathbf{M}^{-1}\mathbf{S})$ to the Krylov vectors.

The GMRES method will generally converge faster than the source iteration procedure [?]. However, as the system becomes scattering dominated, convergence will degrade. To improve the convergence rate, we precondition the GMRES system with the WLA-DSA method. The goal of preconditioning is to efficiently apply an operator to the equation that will approximate the inverse of the matrix operator. Left preconditioning [?] was applied to the above system. In matrix form, we write the preconditioned GMRES equations as

$$(\mathbf{I} + \mathbf{D}^{-1}\mathbf{S}) (\mathbf{I} - \mathbf{L}^{-1}\mathbf{S}) \psi = (\mathbf{I} + \mathbf{D}^{-1}\mathbf{S}) \mathbf{L}^{-1}Q. \quad (8.14)$$

The operation of $(\mathbf{I} + \mathbf{D}^{-1}\mathbf{S})^{-1}$ is equivalent to the DSA procedure, adding the correction to a Krylov vector.

The opensource library `mgmres` was modified to implement the matrix-free version of the GMRES procedure. The infrastructure from the source iteration with DSA

procedure is reused to provide the operation of $(\mathbf{I} + \mathbf{D}^{-1}\mathbf{S})(\mathbf{I} - \mathbf{M}^{-1}\mathbf{S})$ applied to the Krylov vectors returned from the GMRES solver. The preconditioned-GMRES algorithm is

1. Evaluate effective scattering and absorption cross sections with $\{T_i^m : i = 1, 2, \dots, N_c\}$.
2. Form initial source vector b by solving $b = \mathbf{M}^{-1}Q$
3. Apply left-preconditioner operator to b , so $b \leftarrow (\mathbf{I} + \mathbf{D}^{-1}\mathbf{S})\mathbf{M}^{-1}Q$
4. Compute new scattering source $\mathbf{S}\psi^l$.
5. Perform sweeps to calculate $\psi^{l+1/2} = \mathbf{M}^{-1}\mathbf{S}\psi^l + \mathbf{M}^{-1}Q$
6. Compute DSA residual source $\sigma_s(\phi^{l+1/2} - \phi^l)$
7. Solve continuous DSA equations (i.e., Eq. (8.7)) for $\{\delta\phi_{i+1/2}^{l+1/2} : i = 0, 1, \dots, N_c\}$
8. Map the continuous error onto the moment unknowns.
9. If $\|\psi^{l+1} - \psi^l\| < \text{tolerance}$, exit
10. Else: repeat steps 4-9.

The convergence tolerance is based on the residual. Without preconditioning, the diffusion solve is simply removed.

8.4 Computational Results

It is noted we are not interested in measuring the reduction of computational time in this section because in 1D the LO equations can be directly solved efficiently. We are just interested in ensuring that the acceleration methods can reduce the number of scattering iterations sufficiently, including cases where inconsistencies in the LO equations are present.

We test our acceleration methods with three test problems. The first is the two material problem in Sec ???. The second problem is a modification of the two material problem described in Sec. ???. The problem specifications are the same as before, except for modifications to the material properties for $x > 0.5$ cm. In the right region, the parameters are $\sigma_a = 20,000 \text{ cm}^{-1}$, $\sigma_s = 500 \text{ cm}^{-1}$, $c_v = ??? \text{ Jk g}^{-1} \text{ keV}^{-1}$. The third test problem is the diffusion limit problem described in Sec. ???.

8.4.1 Results for LD Spatial Discretization

We first test this problem with the source iteration using DSA to accelerate and compare to an unaccelerated SI solution. 3 batches of 10,000 particles are ran for each HO solve, one HO solver per time step. We tally the total number of source iterations per time step, over the two solves. We initialize the solution for the scattering iterations to zero at the beginning of each LO solve. We reduce the solve time for each to 1.0 sh. The time step begins at 0.001 sh and linearly increases by 15 % each time step to a maximum time step size of 0.01 sh. The larger time step size increases the amount of diffusive behavior. The scattering iterations have a relative convergence between scattering iterations of 1.E-10.

For the DSA we have used a lumped spatial representation in all cases. This should cause some inconsistency issues, slightly degrading the acceleration. There is a slight degradation in the performance, but the GMRES does not work significantly better.

8.5 Analytic Neutronics answer for Source fixup

In this section we model a fixed-source, pure-absorber neutronics calculation where we know the analytic answer to test our fixup. If we make the mesh thick enough, we can set the solution to be the equilibrium answer $\psi(x) = \frac{q(x)}{2\sigma_a}$. For a

Table 8.1: Scattering source iterations for the two material problem. Simulation end time is 1 sh.

Method	Sweeps/Newton Step	Newton Steps/LO Solve
SI	247.0	19.4
SI-DSA	10.1	19.3
GMRES	13.1	19.4
GMRES-DSA	7.7	19.3

Table 8.2: Scattering source iterations for the equilibrium diffusion limit problem. Simulation end time is 3 sh.

LD LO Equations		
Method	Sweeps/Newton Step	Newton Steps/LO Solve
SI	357.4	4.2
SI-DSA	21.9	4.2
GMRES	36.5	4.2
GMRES-DSA	13.3	4.2
Lumped LO Equations		
SI	359.8	4.1
SI-DSA	14.6	4.1
GMRES	37.3	4.1
GMRES-DSA	9.8	4.1

general isotropic source $Q(x)$, the 1D transport equation to be solved is

$$\mu \frac{\partial \psi}{\partial x} + \sigma_a \psi(x, \mu) = \frac{q(x)}{2} \quad (8.15)$$

with boundary condition $\psi(0, \mu) = \psi_{inc}$, $\mu > 0$ and $\psi(x_R, \mu) = \frac{q(x_R)}{2\sigma_a}$ for $\mu < 0$, where x_R is the right boundary. This first order differential equation is solved using an integration factor. The solution to this equation for $\mu > 0$ is given by

$$\psi(x, \mu) = \psi_{inc} e^{-\frac{\sigma_a x}{\mu}} + \int_0^x \frac{q(x')}{2\mu} e^{-\frac{\sigma_a x'}{\mu}} dx', \quad \mu > 0 \quad (8.16)$$

Integration of this result over the positive half range of μ gives

$$\phi^+(x) = \psi_{inc} E_2(\sigma_a x) + \frac{1}{2} \int_0^x q(x') E_1(\sigma_a x') dx'. \quad (8.17)$$

In the simplification of a constant source, the integral reduces to

$$\phi^+(x) = \psi_{inc} E_2(\sigma_a x) + \frac{q}{2\sigma_a} (1 - E_2(\sigma_a x)). \quad (8.18)$$

Also, for a constant source the solution for the negative half range becomes a constant, i.e.,

$$\phi^-(x) = \frac{q}{\sigma_a} \quad (8.19)$$

Combination of the above two equations gives the solution for the scalar flux:

$$\phi(x) = \psi_{inc} E_2(\sigma_a x) + \frac{q}{2\sigma_a} (1 - E_2(\sigma_a x)) + \frac{q}{\sigma_a}. \quad (8.20)$$

8.6 Estimating the Spatial Closure from the HO Solution

This section describes an alternative spatial closure to the LO equations based on a parametric relation from the HO solution. After approximating the angular consistency terms in the time-discretized moment equations, there is still more unknowns than equations, for each spatial cell and half range; an extra equation relating the spatial moments and face values is needed. The HO solution can be used to estimate the relation so that, upon nonlinear convergence, the LO moments will exactly preserve the HO moments. The only discretization error is then what errors were introduced into the HO equations and temperature representation. In the remainder of this section, we will motivate the HO spatial closure by forming half range balance equations to form a single unknown for each cell. We will then discuss possible closure relations, based on modifications to standard spatial closures.

8.6.1 Motivation

A half-range balance equation for $\mu > 0$ is formed by adding the exact L and R moment equations given by Eq. (??) and (??), i.e.,

$$\bar{\mu}_{i+1/2}^+ \phi_{i+1/2}^+ - \bar{\mu}_{i-1/2}^+ \phi_{i-1/2}^+ + \sigma_{a,i} h_i \phi_i^+ = \frac{h_i}{2} q_i, \quad (8.21)$$

where q is a general, isotropic source. To reduce the number of unknowns, the angular consistency terms can be estimated with the HO solution and the inflow term $\phi_{i-1/2}^+$ is known via upwinding from the previous cell or a boundary condition. An additional equation is needed to eliminate the outflow $\phi_{i+1/2}^+$ to produce an equation for a single unknown ϕ_i^+ . Standard spatial discretizations techniques use a uniform approximation to eliminate the outflow in terms of other quantities. Alternatively, the outflow can be eliminated as a parametric combination of other variables based

on the previous HO solution, i.e.,

$$\phi_{i+1/2}^+ = f(\gamma_i^{HO}, \phi_i^+, \phi_x^+, \phi_{i-1/2}^+), \quad (8.22)$$

where γ_i^{HO} is some constant estimated with the HO solution and f is some function of some number of the input variables. If the problem is linear, i.e., q is not a function of ϕ , then application of this closure can ensure that the HO and LO equations produce the same moments. To produce the same moments, the HO solution must also satisfy the local balance equation, e.g., Eq. (8.21), and any other moment equations that are introduced indirectly through the spatial closure. For example, both the LO and HO equation must satisfy the first moment equation in space.

As TRT problems are non-linear (i.e., scattering or thermal emission are included in q), the moments will only be preserved upon non-linear convergence of the source. The nonlinearity introduces the possibility for stability issues. However, we have already consistently formed angular consistency terms, so the the spatial closure should be more stable than introducing other terms, such as in NDA methods. Additionally, because these closure parameters are modifications to standard spatial closures, it should be possible to filter bad values of γ_i^{HO} . Future studies will investigate the stability of this method more rigorously.

8.6.2 Choice of Spatial Closure

We will explore two different closure relations: a scaled slope, i.e.,

$$\phi_{i\pm 1/2}^\pm = \phi_i^\pm \pm \gamma_i \phi_x^\pm \quad (8.23)$$

and a scaled average

$$\phi_{i\pm 1/2}^\pm = \gamma_i \phi_i^\pm \pm \phi_x^\pm, \quad (8.24)$$

where a value of $\gamma_i = 1$ produces the standard linear discontinuous expressions for the extrapolated outflows. The closures are only needed to eliminate the extrapolated face values, not the inflow values for the particular direction equation.

We now use the HO solution to estimate γ_i . For example,

$$\gamma_i^{+,HO} = \frac{\phi_{i+1/2}^+ - \phi_x^+}{\phi_i^+} \quad (8.25)$$

in the scaled slope case. For this closure, as the slope goes to zero this expression becomes undefined. In cells where the slope is $O(10^{-13}\psi_i)$, we use $\gamma_i = 1$. No problems have been observed with the fact that at relatively modest slopes γ becomes very large because the solution is changing minimally in such sections. The main reason for using this closure is it allows for values of γ that are equivalent to step and lumped expressions.

To solve the equations, the expression for the outflow face term is substituted in each equation, using the γ estimated from a HO solution. For instance, the positive balance equation becomes

$$\bar{\mu}_{i+1/2}^+ \left(\gamma_i^{+,HO} \phi_i^+ + \phi_x^+ \right) - \bar{\mu}_{i-1/2}^+ \phi_{i+1/2}^+ + \frac{\sigma_{a,i} h_i}{2} \phi_i^+ = \frac{h_i}{2} q_i, \quad (8.26)$$

noting that ϕ_i^+ and ϕ_x^+ remain as unknowns. The MC solution can provides the face values.

Our LO system is formulated in terms of L and R moments, rather than the average and slope. Thus, the parameteric functions are expressed in terms of the L and R unknowns. There is a spatial closure parameter for each half-range, for each cell.

REWRITE: NOT SURE WHAT TO DO WITH THE NEXT STUFF, IT TALKS

ABOUT HOW LDFE MC DOESNT ACTUALLY CONSISTENTLY MATCH LDFE LO EQUATIONS It is noted that the LD projection of the HO solution produces the same moments, because MC was used to obtain this projection, the outflow will not agree with the LO equations. For example, the upwinding inflow from a previous cell does not match the actual energy that flowed through that surface due to MC noise.

8.6.3 *The Doubly-Discontinuous Trial Space*

Because of the temperature unknowns and the HO scattering source representation, it is necessary to define a representation for the intensity and temperature over the interior of the cell. Thus, we introduce a linear doubly discontinuous (LDD) trial space for the half-range intensities, which is depicted in Fig. 8.1. The linear relation on the interior of the cell preserves the L and R moments of the solution. The temperature is still represented with a linear interpolant of T^4 and T . In the case of strong gradients, it is necessary to modify the interior representation. In this case, we use the standard lumped expression where the moments take on the edge values.

This trial space has an extra unknown outflow, which is eliminated using the HO spatial closure. For the initial LO solve, the outflow is assumed continuous, using the standard upwinding and LD representation. With the outflow term eliminated, the equations have the same numerical complexity as the LD equations. Also, the equations can be closed exactly in terms of moments, if an assumption is made about the relation between spatial moments of T^4 and T . Ultimately, we have to reconstruct the temperature anyways, so we use the LDFE representation for T and T^4 . As long as the outflows that are produced are positive, then the interior moments will be positive. Thus, the lumping representation should ensure a positive

representatin for the temperature.

During the Newton solve, once new half-range intensities are determined, the temperatures are updated using the moment same moment equations given by Eq. (??). This can be confusing because the slope moment, e.g., ψ_x^\pm , does not stricly correspond to the slope in the typical since. We have modified it. This is the same as the lumped closure relation in the previous section, where we are preserving the average and modifying the outflow, then the slope must be modified.e

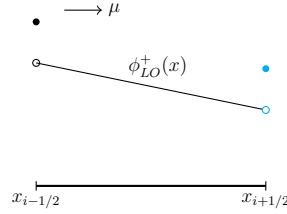


Figure 8.1: Linear doubly-discontinuous representation for mean intensity in LO equations

Poor statistics for the face tallies may result in this trial space producing less accurate results compared to the standard LDFE solution, at least for sufficiently fine meshes where LD can accurately represent the solution. Although the closure will be applied everywhere, we expect the greatest improvement in accuracy for cells where the LDFE trial space produces a negative solution.

In theory, if the problem were linear, or the nonlinear problem was fully converged, then the HO and LO solutions would produce exactly the same moments. There are several issues with ECMC that cause this to not be true, even for a linear problem. With ECMC, global and, particularly, local energy balance are not preserved. There are source biasing techniques for standard MC (e.g., systematic

sampling) that exactly preserve the zeroth moment of the source [4]). It is a requirement that the HO solution satisfies the zeroth moment equation. If the closure relation also uses the first moment, then it must also satisfy the first spatial moment equation. However, because we have to reconstruct the bilinear moment of x and μ , the consistency terms do not exactly preserve the first moment equation. One final reason is that the analog treatment of absorption (at low weights as discussed in Sec. ??) results in $\sigma_a \phi_i^{HO}$ and the amount of energy removed from a cell not being equal, due to statistical noise in the path-length estimators used to estimate ϕ_i^{HO} . However, ECMC will preserve balance to the order of the magnitude of the error, so the closure parameters will reproduce the HO moments to the accuracy of the LO solution.

8.7 Face Tallies and correction near $\mu = 0$

Face-averaged estimators of the angular error are required to compute the outflow for estimating the spatial closure. The standard face-based tallies [4, ?] are used. Tallies are weighted by the appropriate basis functions to compute a linear FE projection in μ at each face. The tally score, for the angular-averaged error $\epsilon_{a,i}$ is defined as

$$\hat{\epsilon}_{a,i\pm 1/2,j} = \frac{1}{N} \sum_{m=1}^{N_{i\pm 1/2,j}} \frac{w_m(x_{i\pm 1/2}, \mu)}{h_\mu |\mu|}, \quad (8.27)$$

where N is the number of histories performed and $N_{i\pm 1/2,j}$ is the number of histories that crossed the surface $i \pm 1/2$, in the j angular element. For the first moment, the tally is

$$\hat{\epsilon}_{\mu,i\pm 1/2,j} = \frac{1}{N} \sum_{m=1}^{N_{i\pm 1/2,j}} 6 \left(\frac{\mu - \mu_j}{h_\mu} \right) \frac{w_m(x_{i\pm 1/2}, \mu)}{|\mu| h_\mu}. \quad (8.28)$$

For positive and negative direction outflows are tallied on the $x_{i+1/2}$ and $x_{i-1/2}$ faces, respectively. Particles are only tallied after leaving a cell, and, as discussed in

Section 7.2, particles born on a surface do not contribute to the tally of that surface.

Near $\mu = 0$, particles can contribute large scores to the zeroth angular moment that lead to large and unbounded variances [?]. To avoid large variances, we have applied the standard fixup [?, ?]. For $|\mu|$ below some small value μ_{cut} , particles contribute the expected score over the range $(0, |\mu_{cut}|)$, based on an approximate, isotropic particle density. Thus, scores in this range have no variance. Assuming an isotropic particle density I_0 , the average of $1/\mu$, for positive μ , is

$$\overline{1/\mu} = \frac{\int_0^{\mu_{cut}} \frac{1}{\mu} I_0 d\mu}{\int_0^{\mu_{cut}} I_0 d\mu} = \frac{2}{\mu_{cut}}. \quad (8.29)$$

For negative μ , $\overline{1/\mu} = -2/\mu_{cut}$. All particles in the range $(0, |\mu_{cut}|)$ contribute the expected score by evaluating the tallies at $\pm\mu = \pm\mu_{cut}$. It is noted that the first angular moment tallies are well defined because there is no μ term in the tally. THIS ISNT REALLY TRUE NOW BECAUSE THE FINITE ELEMENT FIRST MOMENT IS FINE. Additionally, assuming an isotropic intensity over the range helps to limit the first moment near $\mu = 0$, which the LD trial space generally cannot resolve anyways, as discussed in ???.

8.8 Preservation of the Discrete Maximum Principle

An important property for a discretization of the TRT equations is preservation of the discrete maximum principle (MP). The maximum principle states that the material temperature and mean intensity in the interior of the domain should be bounded by the solution at the boundaries of the domain, in the absence of interior energy sources [?, ?]. The analytic solution to the TRT equations satisfies a maximum principle [?], so we desire numerical approximations that preserve the MP in

a discrete sense, for each time step. For IMC simulations, violation of the maximum principle results in the material temperature being artificially higher than the radiation temperature. As discussed in Sec. ??, IMC can violate the MP due to the approximate linearization of the emission source in the time discretization; it is not truly implicit in time. We expect our method, with a fully implicit time discretization, to preserve the MP with sufficient convergence of the nonlinear emission source [?].

To numerically demonstrate that our method preserves the MP, we have simulated problems similar to those in [?]. We modify the Marshak wave problem in Sec. ??, by decreasing c_v and increasing σ_a , to produce a problem which results in MP violations for IMC at various fixed time step sizes. The spatial and temporal discretization determine the occurrence of MP violations for IMC. In particular, if time steps are too large or spatial mesh cells are too small, IMC will demonstrate MP violations [?]. Here, we have kept the spatial mesh size fixed and increased the time step size to produce MP violations. The material specifications for the problem are given in Table 8.3. The domain width is 2.0 cm with $N_c = 150$ uniform spatial mesh cells. The radiation and material energies are initially in equilibrium at 0.01 keV, before an isotropic boundary source of 1 keV is applied at the left boundary at $t = 0$. The simulation end time is $t = 0.1$ sh.

The material and radiation temperature are plotted for an IMC simulation with $\Delta t = 0.025$ sh in Figure 8.2. Figure 8.3 depicts the material temperature for various time step sizes and the fixed mesh size of 150 cells. All IMC simulations used 100,000 histories per time step. As demonstrated in Fig. 8.2, the material temperature exceeds the specified boundary temperature and is artificially hotter than the radiation temperature. This artificial “temperature spike” also leads to a slower propagation of the wave [?]. As shown in Fig. 8.3, as larger time-step sizes are taken the non-

physical results worsen. It is noted that although the final solution for $\Delta t = 0.0001$ sh obeys the MP, during the first few time steps the temperature spikes are present.

The simulations are repeated with the same specifications for the HOLO method. All HOLO simulations used a fixed mesh of 8μ cells by $150 x$ cells, 3 batches per time step, and 6,000 histories per batch. A single HO solve is performed per time step, and the LO relative convergence tolerance is 10^{-6} . The lumping closure is used in all spatial cells and any negativities in the HO solution are rotated to the floor value.

As seen in Fig. 8.4, the HOLO solution does not violate the maximum principle; the temperature is bounded from above by the radiation boundary condition. For these simulations, it was necessary to use the damped Newton's method discussed in Sec. ?? to converge the solutions [?]. A fixed damping parameter with a factor of 0.5 was found to stably converge for all time-step sizes that were simulated. Table 8.4 demonstrates the LO Newton iteration counts for the HOLO method. For reference, a solution with $\Delta t = 10^{-4}$ sh is given, which required no damping to converge. The damped iterations require more iterations to converge. However, it is necessary to converge the nonlinear iterations to produce physically meaningful solutions to this problem. The advantage of the LO solution is that there is no additional cost for the HO solution when the damped method is used.

Table 8.3: Problem specifications for maximum principle violation. Absorption cross section has form $\sigma_a = \sigma_{a,0}/T^3$.

$\sigma_{a,0}$ ($\text{cm}^{-1} \text{ keV}^3$)	4.0
σ_s (cm^{-1})	0.0
ρ (g cm^{-3})	1.0
c_v (jks/keV-g)	0.0081181

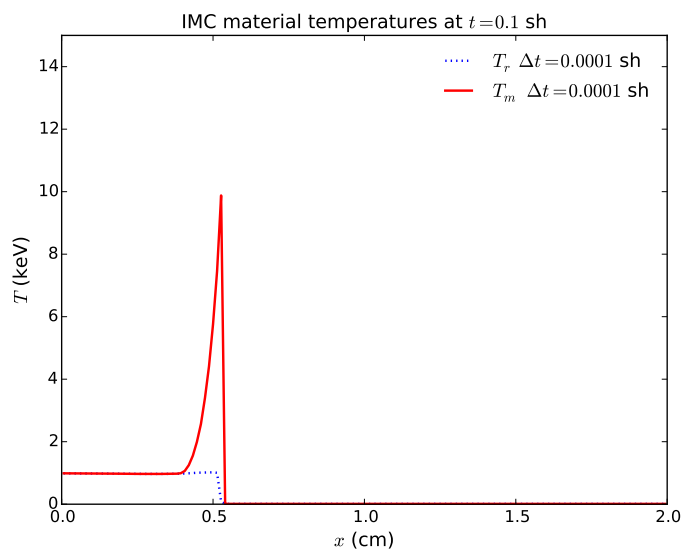


Figure 8.2: T_r and T for MP violation problem with IMC and $\Delta t = 0.001$ sh.

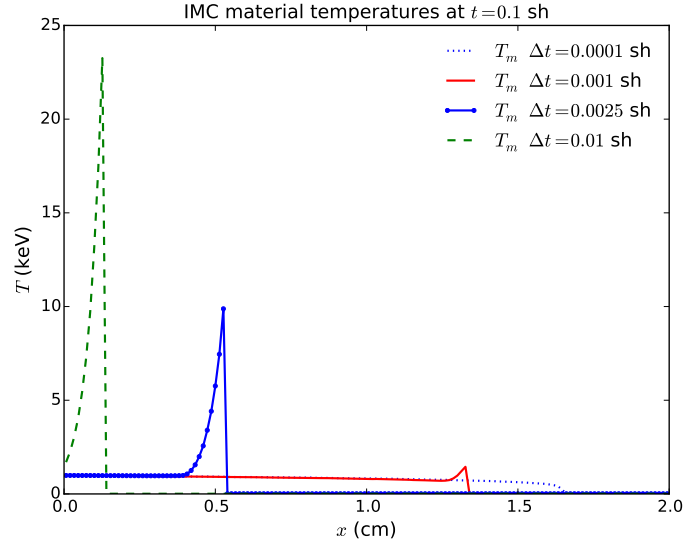


Figure 8.3: T_m for MP violation problem with IMC for various time step sizes.

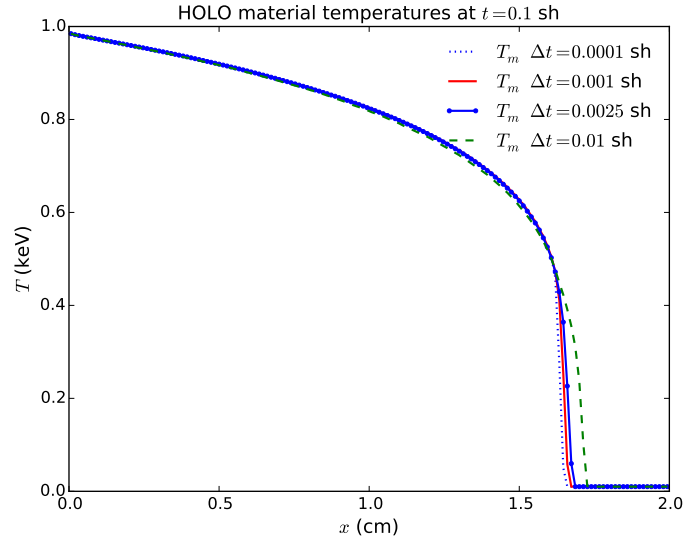


Figure 8.4: T_m for MP violation problem with HOLO method for various time step sizes.

Table 8.4: Comparison of LO Newton iterations for HOLO solution to MP problem and different time step sizes. For $\Delta t = 0.1$ sh, no damping was used; for all other cases a damping factor of 0.5 was used.

Δt (sh)	Newton Iters. / LO Solve
10^{-5}	3.5
10^{-4}	21.0
10^{-3}	28.5
2.5×10^{-3}	29.7
10^{-2}	46.3

REFERENCES

- [1] J. A. Fleck, Jr. and J. D. Cummings, Jr. An implicit monte carlo scheme for calculating time and frequency dependent nonlinear radiation transport. *J. Comput. Phys.*, 8(3):313–342, December 1971.
- [2] Elmer Eugene Lewis and Warren F Miller. *Computational methods of neutron transport*. John Wiley and Sons, Inc., New York, NY, 1984.
- [3] J.R. Peterson. Exponentially Convergent Monte Carlo for the 1-d Transport Equation. Master’s thesis, Texas A&M, 2014.
- [4] J.K. Shultis and W.L. Dunn. *Exploring Monte Carlo Methods*. Academic Press, Burlington, MA 01803, 2012.
- [5] ”Weston M. Stacey”. *”Nuclear Reactor Physics”*. Wiley, 2007.
- [6] T.A. Wareing. *Asymptotic diffusion accelerated discontinuous finite element methods for transport problems*. PhD thesis, Michigan, 1991.
- [7] Allan B. Wollaber, H. Park, R.B. Lowrie, R.M. Rauenzahn, and M.E. Cleveland. Radiation hydrodynamics with a high-order, low-order method. In *ANS Topical Meeting, International Topical Meeting on Mathematics and Computation*, Nashville Tennessee, 2015.